Doctoral Dissertation

Supramolecular Assemblies of a Hexameric Hemoprotein Engineered by Chemical Modifications

January 2020

Shota Hirayama

Graduate School of Engineering,
Osaka University

Contents

General introduction

Natural protein assemblies

In nature, self-assembling systems composed of biomolecules such as DNA, sugars and proteins play crucial roles in biological events. The study of protein assemblies is one of the main subjects because their fascinating structures and functions are remarkably diverse (Figure 1). For example, actin forms filamentous assembly as a rigid cytoskeleton in eukaryotes (Figure 1a).[1] Actin filaments maintain shapes of cells and have polarity on its growth. The direction of the extension is always same and its asymmetric growth serves as the driving forces for the cell movement. Surface layer (S-layer) covers many prokaryotic cells for various roles (Figure 1b).[2] This assembly protects prokaryotic cells from various damages such as environmental changes and supports the cell shapes as a cell wall. Light-harvesting system is large protein assembly composed of a lot of ring-type proteins (LH1 and LH2) containing photosensitizers (Figure 1c).[3] Intra- and interprotein energy migration is necessary to collect energy of sunlight to reaction center for achieving effective photosynthesis. Hemoglobin has a tetrameric structure composed of two different subunits (Figure 1d).[4] These subunits are interacting each other and controlling the affinity of dioxygen for the cofactor, heme, to make it possible to transport oxygen from lung to other tissues effectively. Ferritin is 24-mer protein assembly

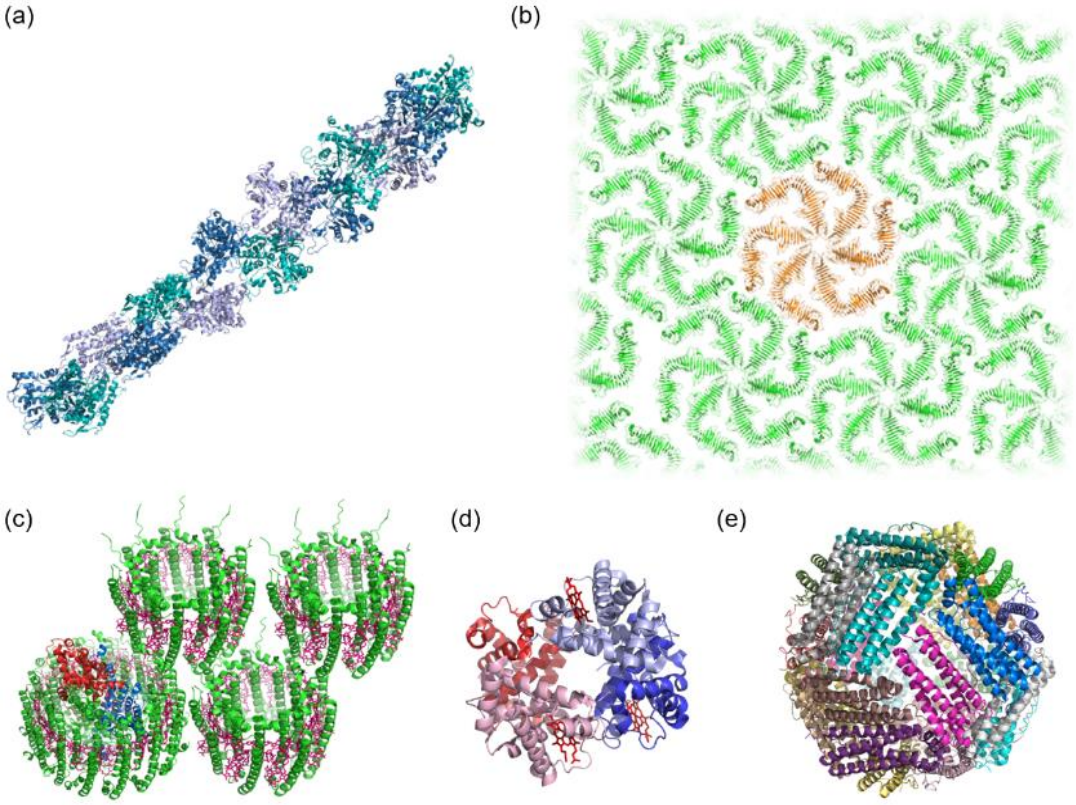

Figure 1. Representative natural protein assemblies. (a) actin filament (PDB ID: 3B63), (b) S-layer (PDB ID: 5N97), (c) light-harvesting system composed of LH1 (PDB ID: 3WMM) and LH2 (PDB ID: 2FKW), (d) hemoglobin (PDB ID: 2HHB) and (e) ferritin (PDB ID: 3E6R).

with hollow spherical shape broadly existing in plants, animals and microorganisms (Figure 1e).[5] Ferritin stores iron ions by the mineralization at the inside hollow sphere to control the amount of iron ions in living organisms. Taken together, there are various types of protein assemblies in nature and have various functions derived from the sophisticated assembling structures.

Artificial protein assemblies

Artificial protein assemblies inspired by nature have been enthusiastically studied as novel bionanomaterials in these two decades.[6] Artificial protein assemblies are expected to be applied to various fields such as drug delivery systems, biomolecular machines, artificial light-harvesting systems and so on. Toward these applications, various types of approaches are utilized and combined for the construction of artificial protein assemblies as stated below.

Genetic engineering method including mutagenesis is one of the most usual approaches to utilize the natural protein–protein interactions.[7] Yeates and coworkers designed and prepared a fusion protein composed of two different monomer units of trimeric protein (bromoperoxidase) and dimeric protein (M1 virus matrix protein) connected by a short α-helix linker. This designed fusion protein spontaneously forms protein cage (Figure 2).[7a] Genetic engineering is also utilized for introduction of the interaction units and/or selective chemical modification sites to generate protein assemblies.

The modification of protein with self-assembling molecules such as DNA,[8] peptides [9] or synthetic polymers[10] is also frequently utilized method. Aida and coworkers modified large tetradecameric protein, GroEL, with two types of DNA complementary to one another. Mixing these modified GroEL resulted in the formation of GroEL tube (Figure 3a). [8a]

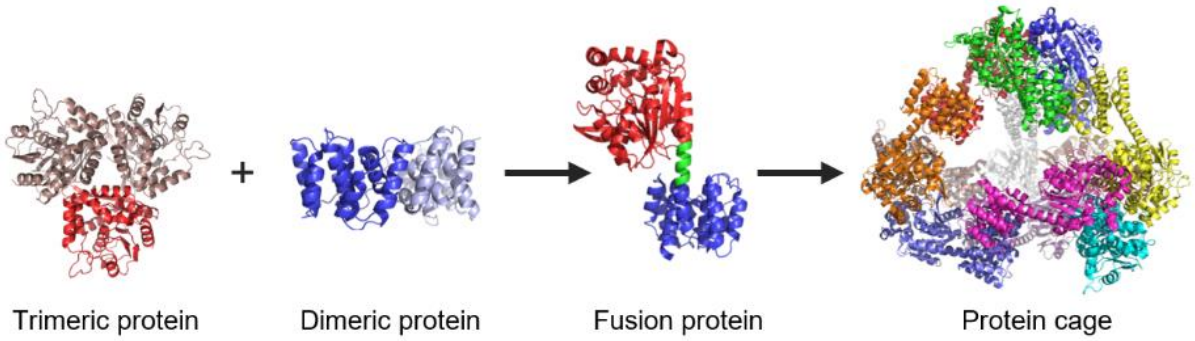

Figure 2. Construction of cage-shaped artificial protein assembly by genetic engineering.

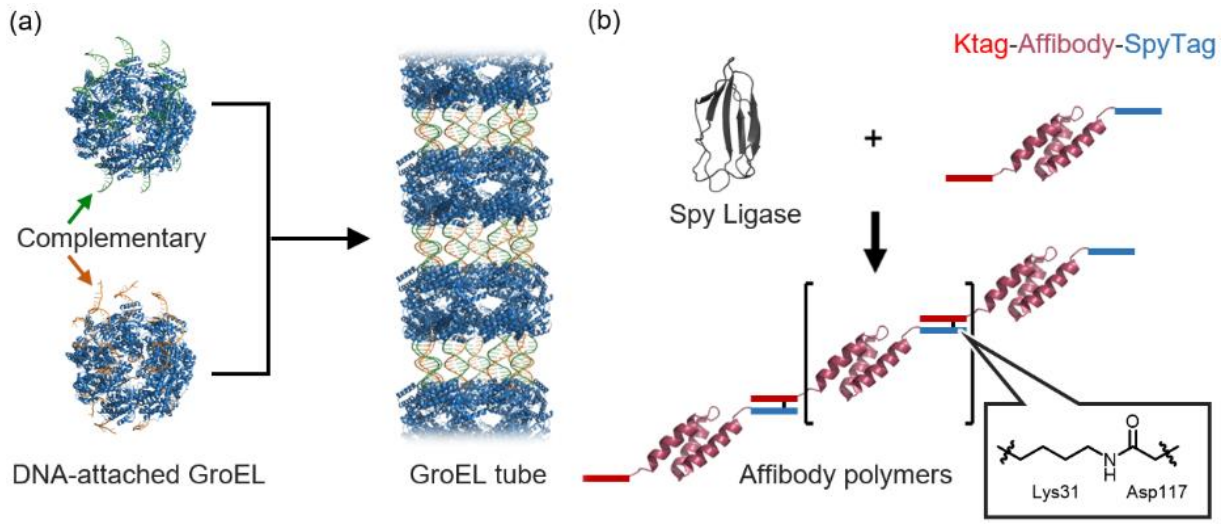

Figure 3. Construction of artificial protein assemblies by (a) hybridization of complementary DNA strands attached onto GroEL units and (b) covalent linkage of KTag and SpyTag attached on protein units by SpyLigase.

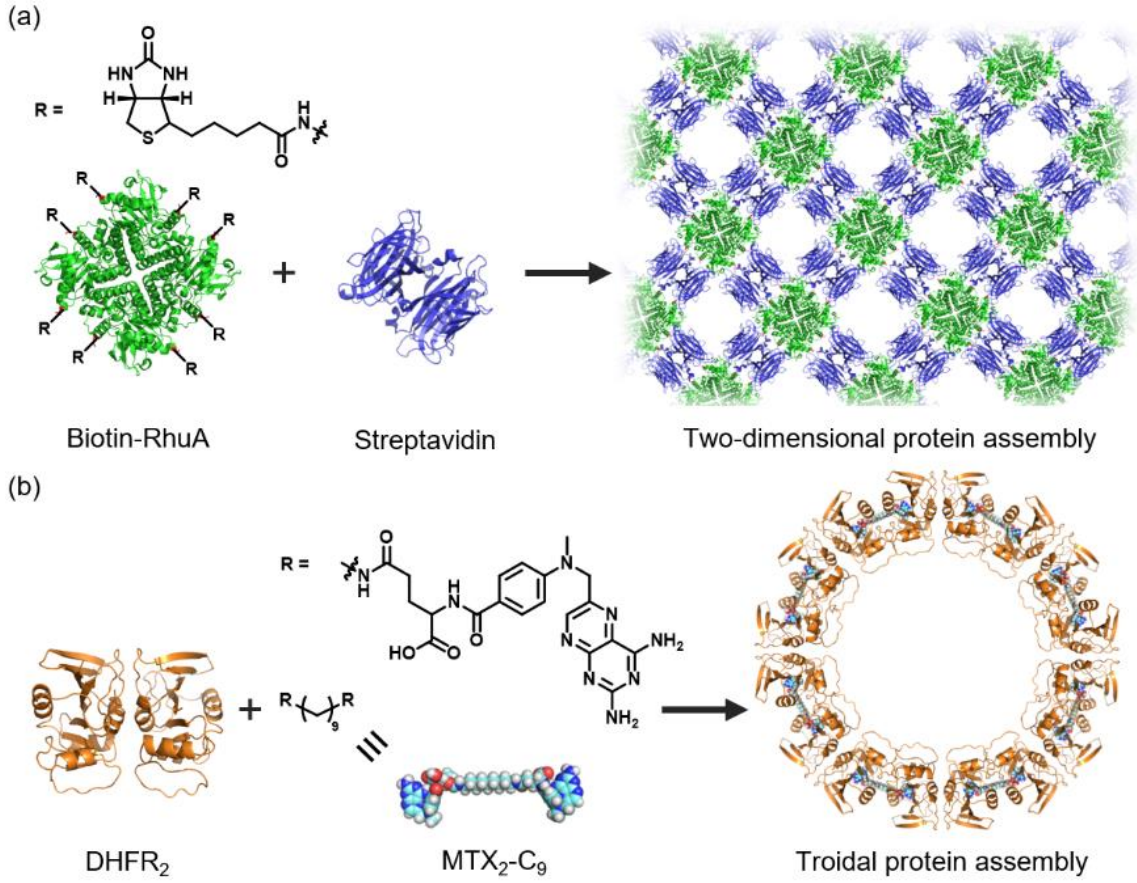

Figure 4. Construction of artificial protein assemblies via (a) the ligand–protein interaction and (b) inhibitor–protein interaction.

Covalent connection is also utilized as a powerful approach extended beyond supramolecular approaches.[11] Howarth and coworkers made use of peptide–peptide ligation to obtain the protein assembly of affibody, which is antibody-like small protein. The affibody containing KTag and SpyTag was covalently linked each other upon the addition of SpyLigase via the isopeptide bond formed between KTag and SpyTag (Figure 3b).[11a]

Connection of proteins by small molecule which has strong affinity against proteins such as ligands and cofactors is also often employed (Figure 4).[12] Schultz and Ringler genetically introduced eight cysteine residues into C_4 symmetric homotetrameric protein RhuA. The introduced cysteine residues were modified with biotin derivative which has remarkably strong affinity against streptavidin, that is also homotetrameric protein. The strong affinity between modified biotin and streptavidin resulted in the formation of the supramolecular protein network of RhuA and streptavidin (Figure 4a). Wagner and his coworkers demonstrated the combination of genetic engineering and protein–ligand interaction. The synthesized dimer of ligand (bis-MTX) bound to dihydrofolate reductase (DHFR) and genetically fused homodimer of DHFR were prepared. Mixing these building blocks resulted in the formation of the toroidal protein assembly (Figure 4b). Additionally, unnatural host–guest interactions are also used.

As described above, there are a lot of reports to demonstrate the formation of artificial protein assemblies by utilizing various techniques in a couple of decades. The research topic has been rapidly developed because of technical advances in the area of protein engineering. However, most reports are limited to the construction of assemblies because of the difficulty to maintain or express functions.

Hemoprotein as a building block of artificial protein assemblies

Hemoprotein is one of the well-known protein families. It contains Fe porphyrin complex (heme) bound into its protein matrix as a cofactor (Figure 5). Hemoprotein expresses various functions such as electron transfer, oxidation reaction, gas storage/carrier and so on. The heme bound to hemoprotein can be reversibly removed because it is incorporated by supramolecular interactions into most of hemoproteins. After the removal of heme, other metal-porphyrinoid complexes can be inserted into the vacant heme pocket.[13] This substitution of heme with other metal porphyrinoid complex

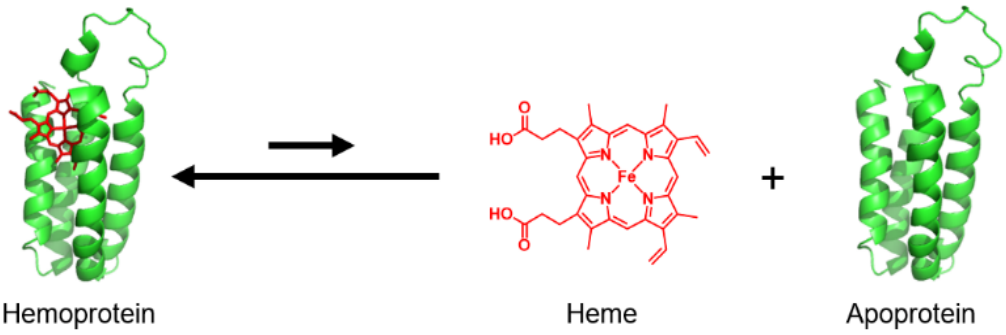

Figure 5. Representative structure of hemoprotein and its reversible binding behavior of heme.

enables to improve the intrinsic function of hemoproteins and to convert into the artificial protein with other function (Figure 6). For example, Hayashi, Hisaeda and coworkers demonstrated that the replacement of heme with Fe porphycene, a structural isomer of heme, in myoglobin dramatically enhances the oxygen binding affinity.[14] Hamachi and coworkers reported the insertion of artificial heme with covalently attached $Ru(bpy)_3$ into apomyoglobin and the photoinduced electron transfer.[15] Niemeyer and coworkers demonstrated that the insertion of artificial heme modified with DNA into hemoprotein achieves the immobilization of protein onto materials covered by complementary DNA.[16] The insertion of metal-substituted heme to change function is also reported. Gray and coworker demonstrated that the insertion of Pd-mesoporphyrin or Pt-mesoporphyrin-inserted myoglobin shows electron transfer from the metalloporphyrin to Ruthenium complex.[17] Ir or Ru-mesoporphyrin-inserted myoglobin is also studied toward the construction of artificial metalloenzyme catalyzing carbene insertion reaction.[18] Thus, the substitution of heme in hemoproteins with other metal-porphyrinoid

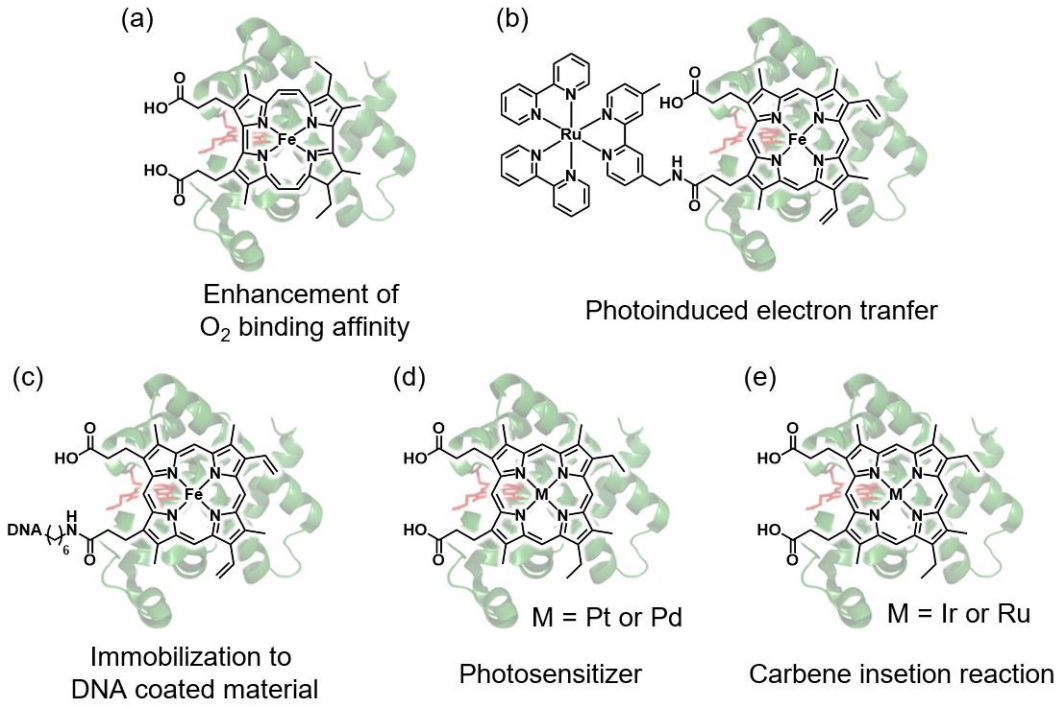

Figure 6. Structures of metal porphyrinoid complexes to generate the reconstituted hemoproteins.

complex dramatically changes the property and function of hemoproteins.

On the other hands, hemoproteins are also used as building blocks of artificial protein assemblies (Figure 7) because hemoprotein assemblies can be a platform of well-ordered metalloporphyrins.[19] Tezcan and coworkers genetically introduced ligating amino acid onto the surface of the monomeric hemoprotein, cytochrome cb_{562} (Cyt cb_{562}), that is a variant of cytochrome b_{562} (Cyt b_{562}), a simple electron transfer hemoprotein, with covalently linked heme molecule in the heme pocket.[20] The tetramer of Cyt cb_{562} was constructed by the coordination of mutated amino acid residues to zinc ions (Figure 7a). Moreover, the additional mutations provided the β-lactamase activity.[21] Hirota and coworkers investigated the domain-swapped hemoprotein assemblies of cytochrome *c (*Cyt *c)*, a

simple electron transfer hemoprotein. The ethanol treatment of aqueous solution of Cyt *c* resulted in the formation of stable oligomer of Cyt *c* such as dimer and trimer (Figure 7b).[22] Barker and his coworkers designed fusion protein of Cyt b_{562} and repeated self-assembling motif, SH3. The SH3 dimer, $(SH3)_2$, is tandem repeat of 86 amino acid residues which is known to form fibrils under appropriate conditions. This designed fusion protein was found to form fibril displaying Cyt b_{562} (Figure 7c).[23] Additionally, Hayashi and his coworkers also demonstrated a series of hemoprotein assemblies, in which the synthetic heme was modified onto the surface of myoglobin[24] or Cyt b_{562}[25] mutant and the following removal of native heme resulted in the formation of supramolecular polymer of hemoproteins (Figure 7d). This hemoprotein polymer was applied to photochemical studies.[26] Thus, several reports describing the construction of artificial hemoprotein assemblies are available and these systems employ small monomeric hemoproteins as building blocks because they are easy to handle.

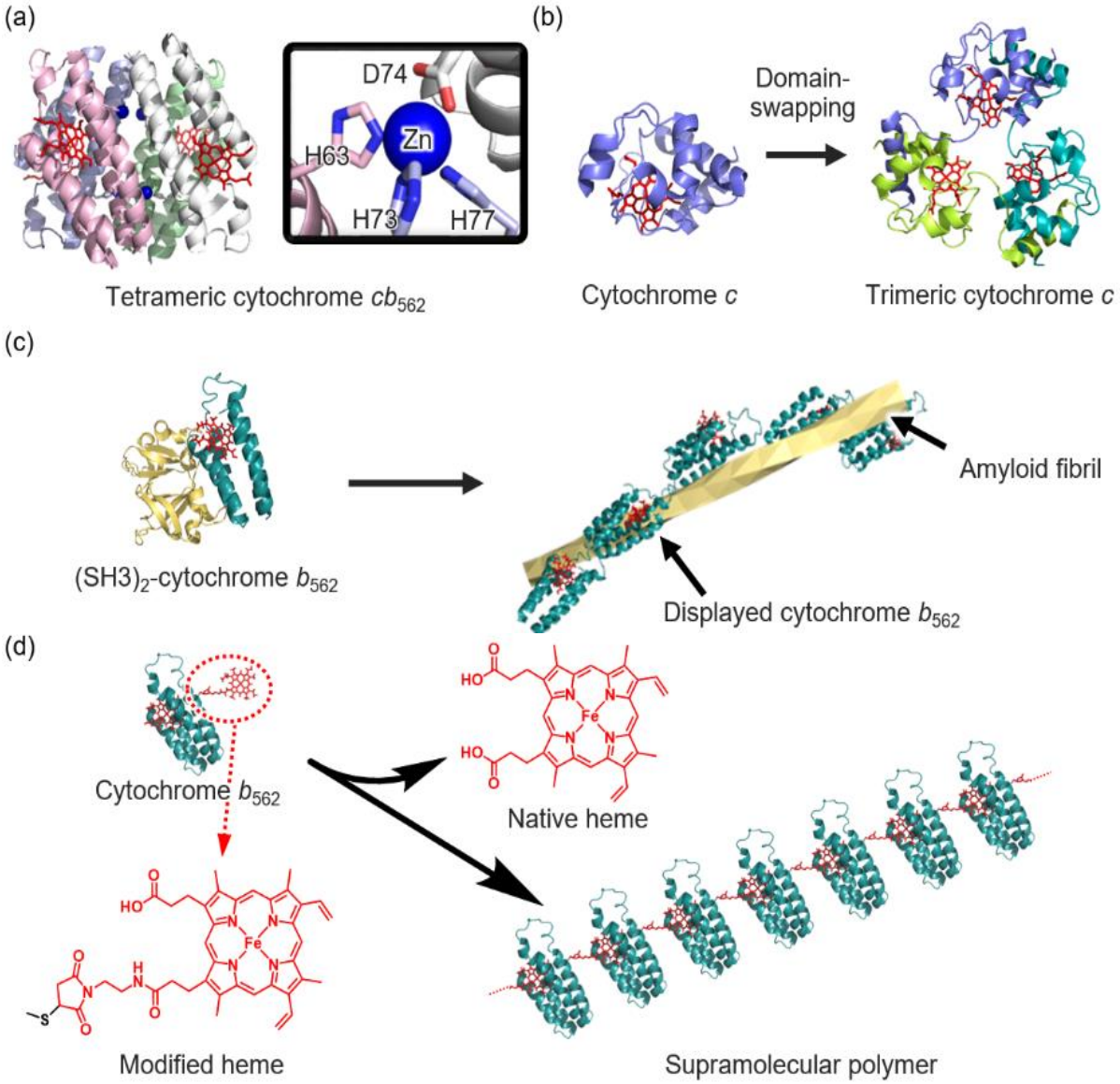

Figure 7. Representative artificial hemoprotein assemblies by (a) Zn coordination, (b) domain-swapping, (c) fibril formation of fused protein and (d) heme–heme pocket interaction.

However, these proteins have low symmetry and difficult to be applied to high-ordered structure.

Hexameric tyrosine-coordinated heme protein (HTHP)

Hexameric tyrosine-coordinated heme protein (HTHP) is a homohexameric hemoprotein with one heme molecule bound into each monomer unit (Figure 8).[27] HTHP is found in marine bacterium *Silicibacter pomeroyi* and has a relatively low molecular weight about ca. 9 kD as a monomer composed of three α-helix domains. HTHP with ring-like arrangement has highly symmetric structure (C_6). The remarkable character of HTHP is its high thermostability. The denaturation midpoint is estimated to be around 130 ºC. The UV–Vis spectra indicate that heme in HTHP has the high-spin ferric form. This ferric form of the heme molecule in HTHP is axially ligated by tyrosine residue (Y45) and there is no ligand at another side. The oxygen atom of the coordinating tyrosine interacted with the nitrogen atom of the arginine residue (Arg42) via hydrogen-bonding network. The distal side in the heme pocket has positive charge because of three arginine residues. Although HTHP shows catalase and peroxidase activity, both of their activities are quite low relative to other native hemoenzymes.

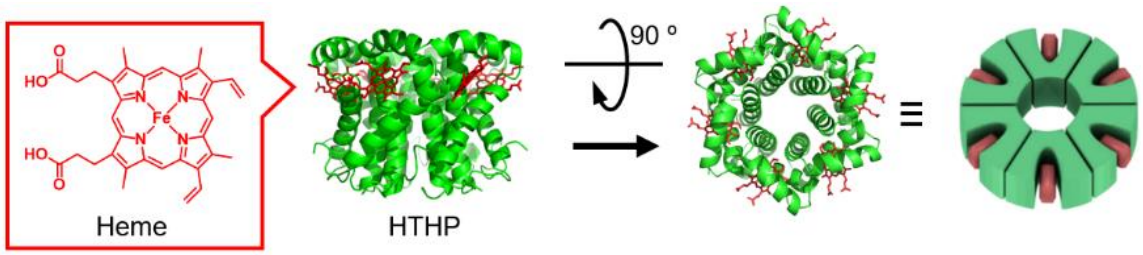

Figure 8. Crystal structure of HTHP (PDB ID: 2OYY) and its schematic representation.

The function of HTHP in nature is still unknown.

Previously, the author's group demonstrated functionalization of HTHP by reconstitution, mutagenesis and chemical modifications. The substitution of axial ligand from tyrosine to histidine provided high peroxidase activity (Figure 9a).[28] The introduction of photosensitizer into the protein matrix[29] and modification by fluorescent dye[30] constructed the model system of light-harvesting system utilizing unique structure of HTHP (Figure 9b). Thus, HTHP is a useful candidate for a building block of artificial protein assemblies since HTHP has remarkably stable and highly symmetric structure and potentials for application studies, unlike the other hemoproteins used as building blocks for artificial protein assemblies demonstrated in previous reports. The presentation of the method for the construction of protein assemblies by using HTHP as a highly symmetric building block could be the landmark for the study of artificial protein assemblies.

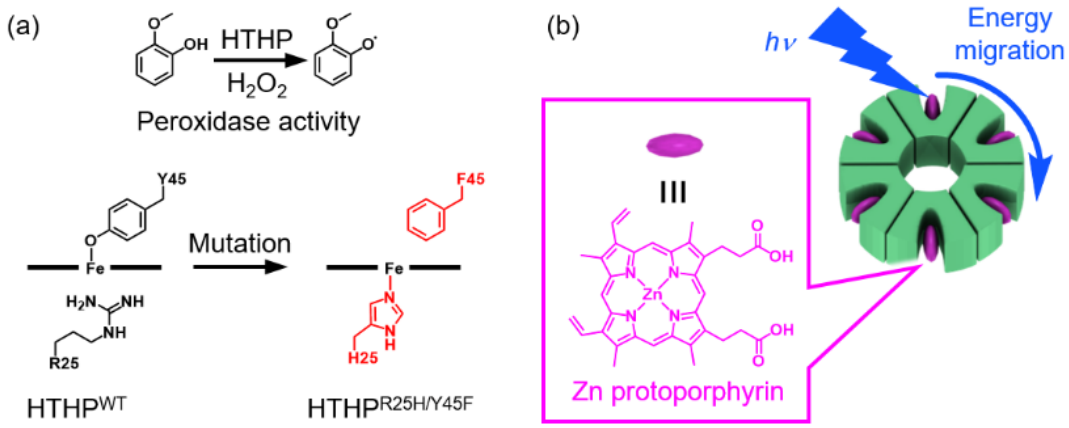

Figure 9. Modification of HTHP by (a) changing axial ligand and (b) insertion of photosensitizer.

Outline of this thesis

In contrast to the previous reports describing artificial assemblies of monomeric hemoproteins, the author focused on HTHP as a building block for the assembly because of its symmetrical structure, thermal stability and potential for functionalization. This thesis describes the formation of artificial assemblies of HTHP by the chemical modification with various molecules. Depending on the molecules modified onto the surface of HTHP, different protein assemblies were constructed.

Chapter 1: Supramolecular Dimerization of HTHP via Multiple Pyrene–pyrene Interactions

Pyrene modification onto the surface of HTHP induced the multiple pyrene–pyrene interaction between two HTHP hexamers. Size exclusion chromatography (SEC) revealed that this pyrene-linked HTHP forms stable supramolecular dimer of HTHP. It was also revealed that the obtained supramolecular dimer of HTHP reversibly dissociates upon removal of the heme cofactor.

Chapter 2: Construction of HTHP Sheet and Direct Observation of Dynamic Process of Its Formation

Two-dimensional HTHP assembly was constructed via host–guest interactions between modified peptide which has phenylalanine-glycine-glycine (FGG) sequence as a guest and host molecule, cucurbit[8]uril (CB8). Additionally, the dynamic formation process of two-dimensional HTHP assembly was observed by high-speed atomic force microscopy. The assembly forms and grows larger than hundreds of nanometers square within a few minutes after the addition of CB8.

Chapter 3: Thermoresponsive Micelle Construction of HTHP Modified with Poly(*N*-isopropylacrylamide) Designing toward an Artificial Light-harvesting System

Thermoresponsive construction of micellar assembly of HTHP was demonstrated by the modification with thermoresponsive polymer, Poly(*N*-isopropylacrylamide). The formation of this micellar assembly is repeatable and the structure of HTHP is stable during the assembling procedure. Additionally, the heme in the assembly was substituted with Zn protoporphyrin IX to apply this assembly as an artificial light-harvesting system. The energy migration at the surface of the obtained micellar assembly was evaluated by fluorescence measurements.

References

1. Pollard, T. D.; Cooper, J. A. *Science* **2009**, *326*, 1208-1212.
2. Tanmay, A. M. B.; Danguole, K.-C.; Gail, G. H.; Ellen, W. Y.; Jessica, M. D.; Wim, J. H. H.; Yves, V. B.; John, A. G. B.; Jan, L. *Nat. Microbiol.* **2017**, *2*, 17059.
3. Scholes, G. D.; Fleming, G. R.; Olaya-Castro, O.; van Grondelle, R. *Nat. Chem.* **2011**, *3*, 763-774.
4. Shaanan, B. *J. Mol. Biol.* **1983**, *171*, 31-59.
5. Liu, X.; Theil, E. C. *Acc. Chem. Res.* **2005**, *38*, 167-175.
6. (a) Fegan, A.; White, B.; Carlson, J. C. T.; Wagner, C. R. *Chem. Rev.* **2010**, *110*, 3315-3336. (b) Bai, Y.; Luo, Q.; Liu, J. *Chem. Soc. Rev.* **2016**, *45*, 2756-2767. (c) van Dun, S. Ottmann, C.; Milroy, L.-G.; Brunsveld, L., *J. Am. Chem. Soc.* **2017**, *139*, 13960-13968.
7. (a) Lai, Y.-T.; Cascio, D.; Yeates, T. O. *Science* **2012**, 336, 1129. (b) Kobayashi, N.; Yanase, K.; Sato, T.; Unzai, S.; Hecht, M. H.; Arai, R. *J. Am. Chem. Soc.* **2015**, *137*, 11285-11293. (c) Kawakami, N.; Kondo, H.; Matsuzawa, Y.; Hayasaka, K.; Nasu, E.; Sasahara, K.; Arai, R.; Miyamoto, K. *Angew. Chem. Int. Ed.* **2018**, *57*, 12400-12404.
8. (a) Kashiwagi,D.; Sim, S.; Niwa, T.; Taguchi, H.; Aida, T. *J. Am. Chem. Soc.* **2018**, *140*, 26-29. (b) Subramanian, R. H.; Smith, S. J.; Alberstein, R. G.; Bailey, J. B.; Zhang, L.; Cardone, G.; Suominen, L.; Chami, M.; Stahlberg, H.; Baker, T. S.; Tezcan, F. A. *ACS Cent. Sci.* **2018**, *4*, 11, 1578-1586. (c) McMillan, J. R.; Hayes, O. G.; Remis, J. P.; Mirkin, C. A. *J. Am. Chem. Soc.* **2018**, *140*, 46, 15950-15956.
9. Matsuura, K.; Honjo, T. *Bioconjugate Chem.* **2019**, *30*, 1636-1641.
10. (a) Reynhout, I. C.; Cornelissen, J. J. L. M.; Nolte, R. J. M. *J. Am. Chem. Soc.* **2007**, *129*, 2327-2332. (b) Wan, X.; Liu, S. *Macromol. Rapid Commun.* **2010**, *31*, 2070-2076.
11. (a) Fierer, J. O.; Veggiani, G.; Howarth, M. *Proc. Natl. Acad. Sci. U. S. A.* **2014**, *111*, E1176-E1181. (b) Ballister, E. R.; Lai, A. H.; Zuckermann, R. N.; Cheng, Y.; Mougous, J. D. *Proc. Natl. Acad. Sci. U. S. A.* **2008**, *105*, 3733-3738.
12. (a) Ringler, P.; Schultz, G. E. *Science* **2003**, *302*, 106-109. (b) Carlson, J. C. T.; Jena, S. S.; Flenniken, M.; Chou, T.-F.; Siegel, R. A.; Wagner, C. R. *J. Am. Chem. Soc.* **2006**, *128*, 7630-7638.
13. Hayashi, T.; Hisaeda, Y. *Acc. Chem. Res.* **2002**, *35*, 35-43
14. Hayashi, T.; Dejima, H.; Matsuo, T.; Sato, H.; Murata, D.; Hisaeda, Y. *J. Am. Chem. Soc.* **2002**, *124*, 11226-11227.
15. Hamachi, I.; Tsukiji, S.; Shinkai, S.; Oishi, S. *J. Am. Chem. Soc.* **1999**, *121*, 23, 5500-5506.
16. Fruk, L.; Niemeyer, C. M.; *Angew. Chem. Int. Ed.* **2005**, *44*, 2603-2606.
17. Cowan, J. A.; Gray, H. B.; *Inorg. Chem.* **1989**, *28*, 11, 2074-2078.
18. (a) Key, H. M.; Dydio, P.; Clark D.S.; Hartwig, J. F. *Nature* **2016**, *534*, 534-537. (b) Wolf, M. W.; Vargas, D. A. Lehnert, N. *Inorg. Chem.* **2017**, *56*, 5623-5635.
19. Oohora, K.; Hayashi, T. *Curr. Opin. Chem. Biol.* **2014**, *19*, 154-161.

20. (a) Salgado, E. N.; Ambroggio, X. I.; Brodin, J. D.; Lewis, R. A.; Kuhlman, B.; Tezcan, F. A. *Proc. Natl. Acad. Sci.* **2010**, *107*, 1827-1832. (b) Salgado, E. N.; Faraone-Mennella, J.; Tezcan, F. A. *J. Am. Chem. Soc.* **2007**, *129*, 13374-13375.
21. Song, W. J.; Tezcan, F. A. *Science* **2014,** *346*, 1525-1528.
22. Hirota, S.; Hattori, Y.; Nagao, S.; Taketa, M.; Komori, H.; Kamikubo, H.; Wang, Z.; Takahashi, I.; Negi, S.; Sugiura, Y.; Kataoka, M.; Higuchi, Y. *Proc. Natl. Acad. Sci.* **2010**, *107*, 12854-12859.
23. Baldwin, A. J.; Bader, R.; Christodoulou, J.; MacPhee, C. E.; Dobson, C. M.; Barker, P. D. *J. Am. Chem. Soc.* **2006**, *128*, 2162-2163.
24. Kitagishi, H.; Oohora, K.; Yamaguchi, H.; Sato, H.; Matsuo, T.; Harada, A.; Hayashi, T. *J. Am. Chem. Soc.* **2007**, *129*, 10326-10327.
25. Kitagishi, H.; Kakikura, Y.; Yamaguchi, H.; Oohora, K.; Harada, A.; Hayashi, T. *Angew. Chem. Int. Ed.,* **2009**, *48*, 1271-1274.
26. (a) Onoda, A.; Kakikura, Y.; Uematsu, T.; Kuwabata, S.; Hayashi, T. *Angew. Chem. Int. Ed.* **2012** *51*, 2628-2631. (b) Kajihara, R.; Oohora, K.; Hayashi, T. *J. Inorg. Biochem.* **2019**, *193*, 42-51.
27. Jeoung, J.-H.; Pippig, D. A.; Martins, B. M.; Wagener, N.; Dobbek, H. *J. Mol. Biol.* **2007**, *368*, 1122-1131.
28. Mashima, T.; Oohora, K.; Hayashi, T. *J. Porphyrins Phthalocyanines* **2017**, *21*, 825-831.
29. Oohora, K.; Mashima, T.; Ohkubo, K.; Fukuzumi, S.; Hayashi, T. *Chem. Commun.* **2015**, *51*, 11138-11140.
30. Mashima, T.; Oohora, K.; Hayashi, T. *Phys. Chem. Chem. Phys.* **2018**, *20*, 3200-3209.

Chapter 1
Supramolecular Dimerization of HTHP via Multiple Pyrene–pyrene Interactions

1-1. Introduction

Artificially-constructed supramolecular protein assemblies have been rapidly investigated in these two decades due to advances in techniques for genetic and/or chemical modification of proteins.[1-8] There are four main strategies for forming supramolecular protein-protein interactions to induce formation of artificial protein assemblies: (i) modifications to induce the hydrogen-bonding, hydrophobic and electrostatic interactions between amino acid residues on the protein surface as seen in natural systems, supported by protein-fusion and/or computational design;[5,8-11] (ii) provision of coordination bonding between metal ions and amino acids or unnatural moieties such as phenanthroline attached to proteins;[4,12-15] (iii) modifications to induce the interactions between proteins and specifically bound small molecules such as substrates, cofactors and protein ligands;[6,7, 16-20] and (iv) provision of non-natural host-guest systems such as the FGG tag and cucurbituril.[2,3,21-24] Advances in analytical techniques for generating protein assemblies have contributed significantly to this research area and precise structures of protein assemblies have been characterized by X-ray crystallography as well as atomic force microscopy and electron microscopy. Various structures of artificial protein assemblies such as rings,[25-27] two-dimensional sheets,[28-30] tubes[31-33] and cages[34-37] have been reported by several research groups by using these strategies. Moreover, some of the protein assembling systems are candidates for development as artificial enzymes,[4,38] light-harvesting antennas[39-41] and drug delivery systems.[42-44] However, artificial protein assemblies formed by the multivalent effect consisting of only weak interactions have been limited[2,11,45,46] although this effect is well known to induce formation of native protein assemblies. In this context, the author has focused on the generation of protein assemblies formed by multiple pyrene–pyrene interactions.

In protein science, pyrene derivatives have been mainly employed as an interface for constructing carbon materials and a prove to indicate protein structural changes. In the former case, the large hydrophobic and π system of pyrene enables immobilization of pyrene-attached proteins onto other π system such as carbon nanotubes or graphene.[47-49] In the latter case, the excimer emission of pyrene molecules interacted with each other via the proximity effect has been utilized.[50-52] In most cases, pyrene molecules are attached onto cysteine residues in a reaction with iodoacetamide or maleimide groups to evaluate the structural changes. Matsuo and his coworkers introduced pyrene moieties at two cysteine residues on adenylate kinase and detected excimer emission only in the closed protein structure induced by substrate binding.[51] Engineered ferritin, which is assembled to a spherical 24-mer and disassembled to dimer under high and low-salt concentrations, respectively, was modified with pyrene at the dimer interface by Baiocco and coworkers.[52] In this system, the intensity of excimer emission works as a sensitive sensor of the assembly event: the dimer has the strong excimer emission, whereas the 24-mer has weak fluorescence due to structural changes occurring during assembly. Thus,

the pyrene molecules are strongly interacted with each other in the dimer state, while the single pyrene–pyrene interaction is too weak to generate the protein dimer or larger assembly. Here, multivalent pyrene–pyrene interactions are expected to serve as a driving force for formation of the protein assembly. In this context, the author employed hexameric tyrosine coordinated hemoprotein (HTHP)[53] as a protein assembly building block because this protein is a homohexamer with a C_6-symetric cylindrical shape (Figure 1-1), and demonstrated multiple pyrene–pyrene interactions by introduction of a pyrene moiety onto each protein monomer subunit. The present study describes the supramolecular assembling behavior of pyrene-attached HTHP.

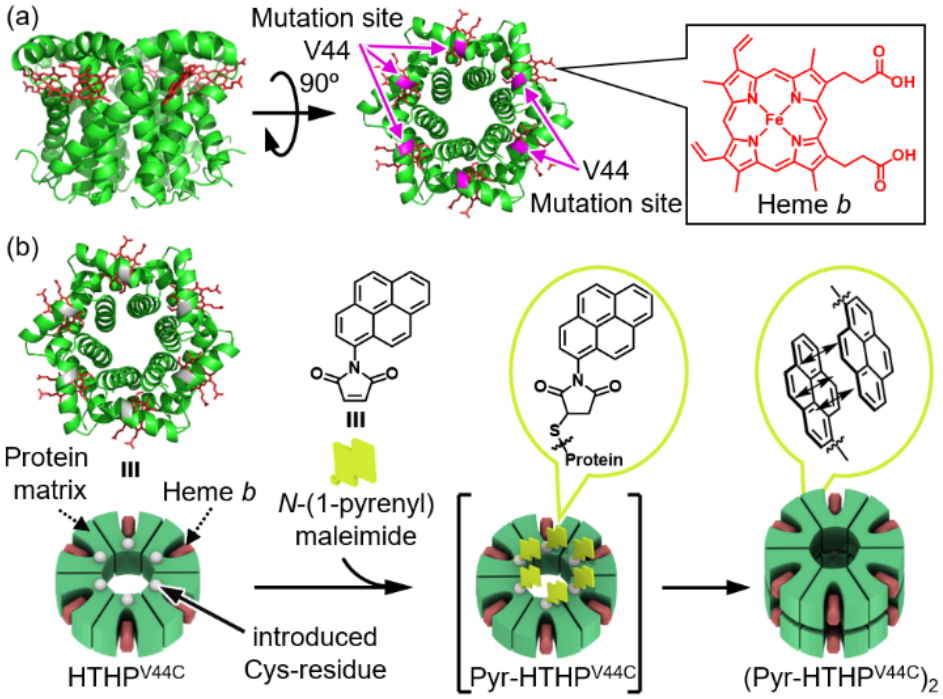

Figure 1-1. (a) Crystal structure of HTHP (PDB ID: 2OYY) with the mutation site in this work. (b) Schematic representation of the surface modification of HTHP^{V44C} with *N*-(1-pyrenyl)maleimide and formation of the supramolecular dimer of the hexamers.

1-2. Results and discussion

Modification of HTHP with *N*-(1-pyrenyl)maleimide

The author chose the V44 residue of HTHP for attachment of pyrene because this residue is exposed on the outer surface and placed at the bottom of the cylindrical structure of HTHP. Since wild type HTHP (HTHP^{WT}) have no cysteine residues, V44 was replaced with cysteine as a unique reaction point in each monomer unit to introduce a total of six cysteine residues into the hexamer. The V44C mutant (HTHP^{V44C}) was successfully prepared by site direct mutagenesis and expression/purification protocols for HTHP. The shape of UV–vis spectrum of HTHP^{V44C} is almost same to that of HTHP^{WT} and the expected mass-number was observed in MALDI-TOF mass spectra of HTHP^{V44C}. The SDS-

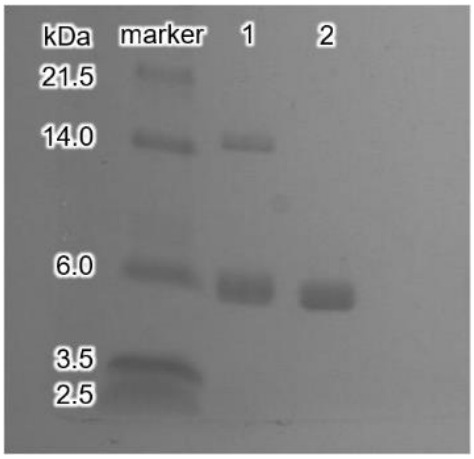

Figure 1-2. SDS-PAGE of as-prepared HTHP^{V44C} (lane 1) and DTT-treated HTHP^{V44C} (lane 2).

PAGE result of HTHP^{V44C} indicates a single band in the 6-7 kDa region (Figure 1-2), which corresponds to monomer unit of HTHP^{V44C} as expected because HTHP dissociates to its monomer under the denaturing conditions of SDS-PAGE. Additionally, another band is found in the 14-15 kDa region in SDS-PAGE without mercaptoethanol reductant which cleaves disulfide bonds. In the size exclusion chromatography (SEC) measurements, two peaks are observed at 13.2 and 14.8 mL of elution volume (Figure 1-3). These peaks correspond to a dimer of the hexamers and the hexamer itself, respectively, according to the SEC traces of authentic samples. These findings indicates that the prepared HTHP^{V44C} is a mixture of the hexamer and the dimer of the hexamers linked by an interhexamer disulfide bond. Therefore, reductive cleavage of the disulfide bond was carried out using dithiothreitol (DTT) before the modification reaction of HTHP^{V44C}. After confirmation of the dissociation into the hexamer detected by SEC, HTHP^{V44C} was modified with *N*-(1-pyrenyl)maleimide. The characterization of the modified protein by MALDI-TOF mass spectrometry (Figure 1-4) reveals that the modification yield is ca. 92% based on the monomer after optimization (to be discussed in more detail below). The UV–vis spectrum of the modified HTHP^{V44C} includes characteristic absorption peaks at 278, 346, 403, 499 and 616 nm derived from the pyrene moiety and heme bound into HTHP (Figure 1-5). Thus, the author confirmed the modification of HTHP^{V44C} by *N*-(1-pyrenyl)maleimide. The pyrene-attached protein is given the designation pyr-HTHP^{V44C}.

Supramolecular dimerization of pyrene-attached HTHP

The size of pyr-HTHP^{V44C} was evaluated. The SEC trace of pyr-HTHP^{V44C} shows only a single peak eluting at 13.2 mL (Figure 1-3c), which is the same elution volume of the disulfide dimer of HTHP^{V44C}. Here, two possibilities were considered: (i) regeneration of the disulfide dimer of the hexamers in the course of the modification reaction; and (ii) supramolecular dimerization via the pyrene molecules attached onto the protein. The former possibility was ruled out according to the observation that the SEC profile does not shift after the DTT treatment (Figure 1-6). Thus, it appears

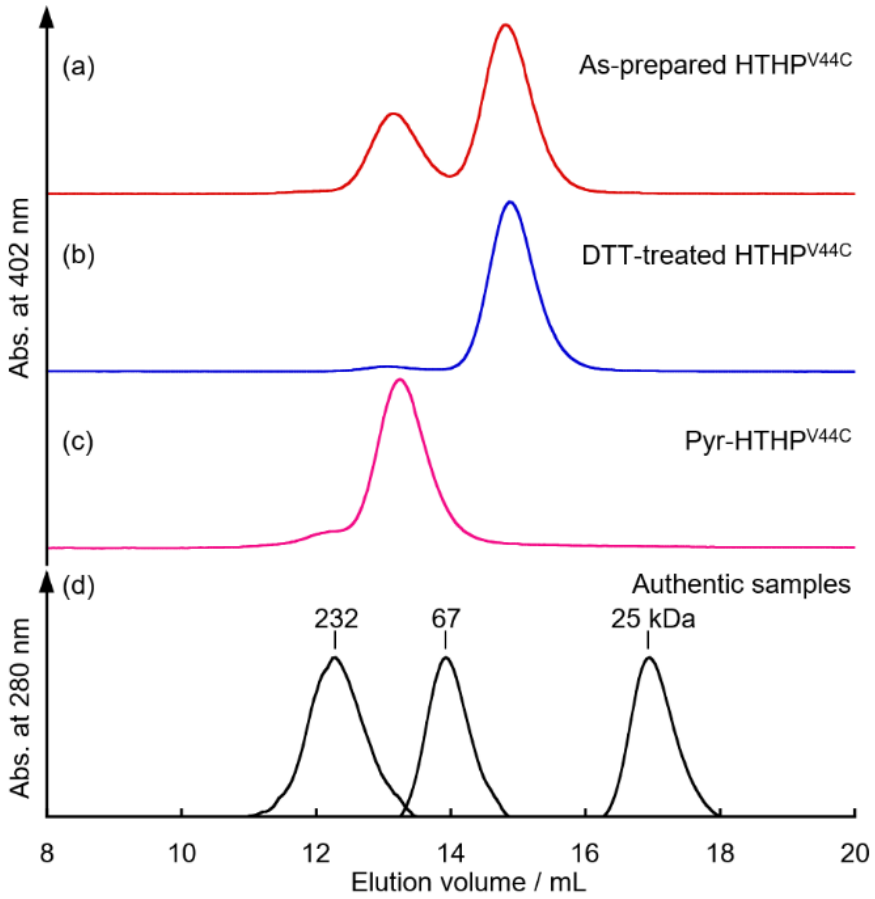

Figure 1-3. SEC traces of (a) as-prepared HTHP^{V44C}, (b) DTT-treated HTHP^{V44C}, (c) pyr-HTHP^{V44C} and (d) authentic samples.

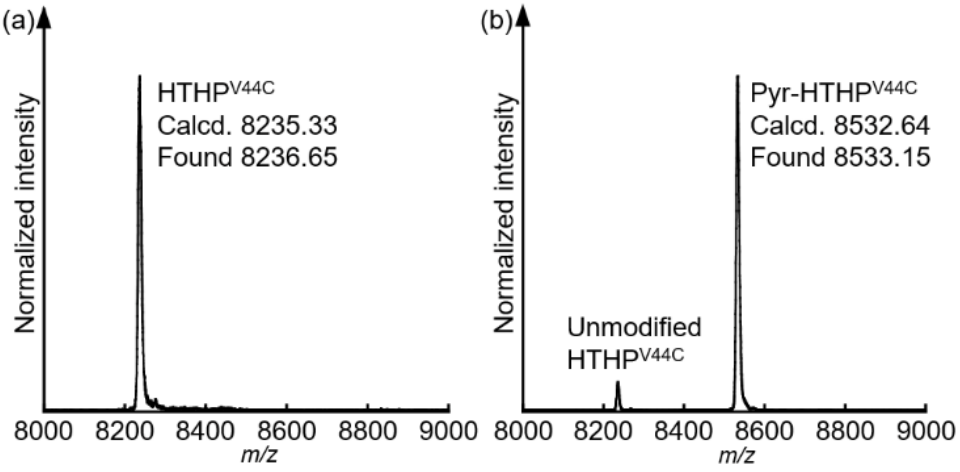

Figure 1-4. MALDI-TOF mass spectra of (a) HTHP^{V44C} and (b) pyr-HTHP^{V44C}.

that supramolecular dimerization of the pyr-HTHP^{V44C} via pyrene–pyrene interactions is responsible for construction of the dimer. Moreover, the hydrodynamic diameter of the pyr-HTHP^{V44C} was determined to be 9.0 nm by dynamic light scattering (DLS) measurements (Figure 1-7). The diameter of HTHP^{WT} is 6.3 nm and the diameter of pyr-HTHP^{V44C} is estimated to be that of the dimer of the

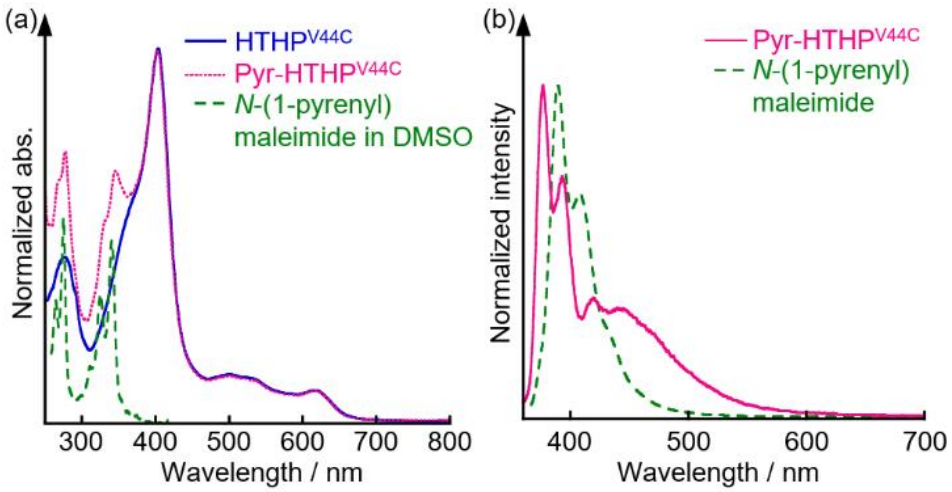

Figure 1-5. (a) UV–vis spectra of HTHP^{V44C}, pyrene and pyr-HTHP^{V44C}. (b) Fluorescence spectra of pyrene and pyr-HTHP^{V44C}: λ_{ex} = 346 nm. Conditions: solvent 100 mM potassium phosphate buffer, pH 7.0 for protein and DMSO for *N*-(1-pyrenyl)maleimide, temperature = 25 ºC.

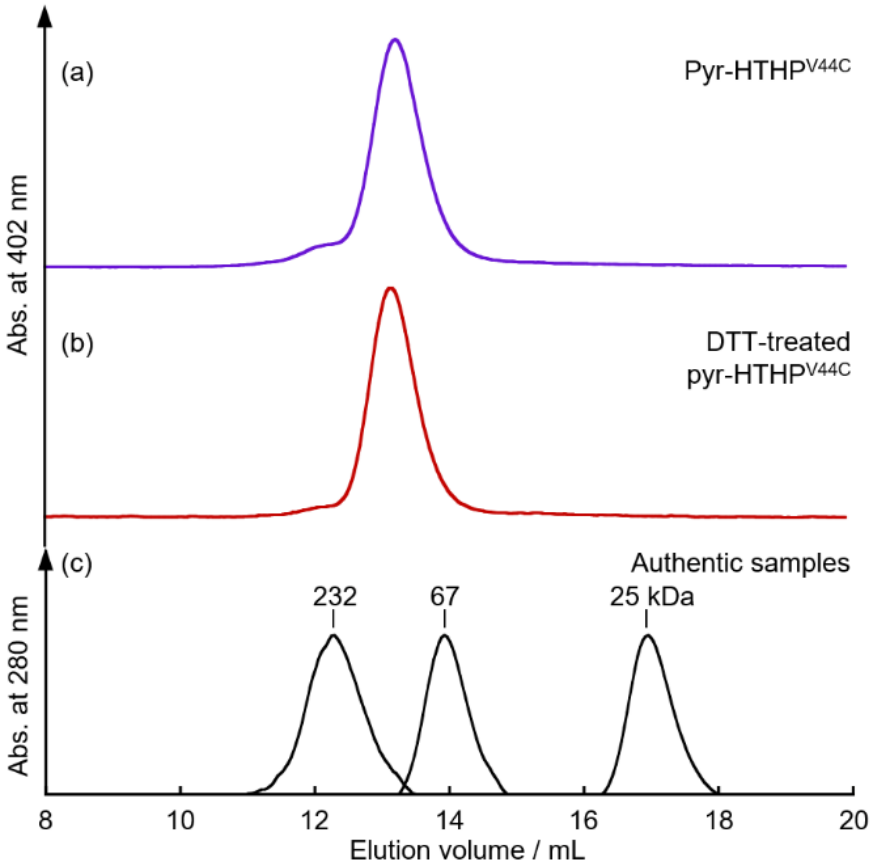

Figure 1-6. SEC traces of (a) pyr-HTHP^{V44C}, (b) DTT-treated pyr-HTHP^{V44C} and (c) authentic samples.

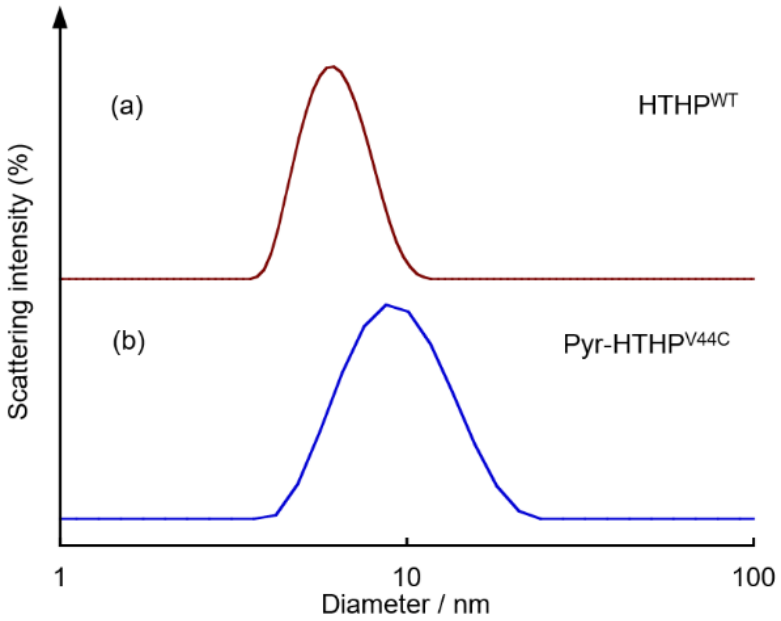

Figure 1-7. Hydrodynamic radius distributions as determined by DLS traces for (a) $HTHP^{WT}$ and (b) pyr-$HTHP^{V44C}$.

hexamers, which is consistent with the results of SEC described above. This supramolecular dimerization is supported also by fluorescence spectroscopy measurements. While the fluorescence peaks derived from pyrene are observed at 389 nm and 408 nm, a 442 nm emission peak is observed for pyr-$HTHP^{V44C}$ (Figure1-5b). This is similar to the typical excimer emission of pyrene molecules, supporting the estimation that pyrene–pyrene interactions are responsible for formation of the dimer of the hexamers, (pyr-$HTHP^{V44C}$)$_2$. The intensity of the excimer emission is, however, weaker than that of the intrinsic pyrene fluorescence in pyr-$HTHP^{V44C}$, whereas the usual excimer emission from a stable dimer of pyrene is stronger than that of the intrinsic pyrene fluorescence. This could be caused by two following possibilities: i) The excimer emission is quenched by heme, which is located within 1 nm of the pyrene molecule. ii) Not all pyrene molecules contribute to the supramolecular dimerization of the hexamer. The author attempted the inhibition of the pyrene–pyrene interactions upon addition of a water-soluble pyrene derivative, 1-pyrene sulfonic acid potassium salt (pyr-SO_3K). Figure 1-8 shows the DLS results upon addition of the presence of pyr-SO_3K. Contrary to the expectation, no disassembly of the dimer was observed, suggesting that the multiple pyrene–pyrene interactions are so strong relative to simple interaction between the attached pyrene moiety on the protein surface and pyr-SO_3K. As a control experiment, a smaller aromatic molecule, naphthalene, was attached instead of pyrene. *N*-(1-naphthyl)maleimide was reacted with $HTHP^{V44C}$ in a similar manner as the modification reaction with *N*-(1-pyrenyl)maleimide. In this case, quantitative modification was confirmed by MALDI-TOF mass spectroscopy (Figure 1-9a) and the naphthalene-attached protein is given the designation nap-$HTHP^{V44C}$. UV–vis and CD spectra indicate that the structure of HTHP is maintained after the modification. Contrary to pyr-$HTHP^{V44C}$, the SEC trace of nap-$HTHP^{V44C}$ has a single peak eluting at 16.2 mL (Figure 1-9b). This is a slightly late elution volume compared with

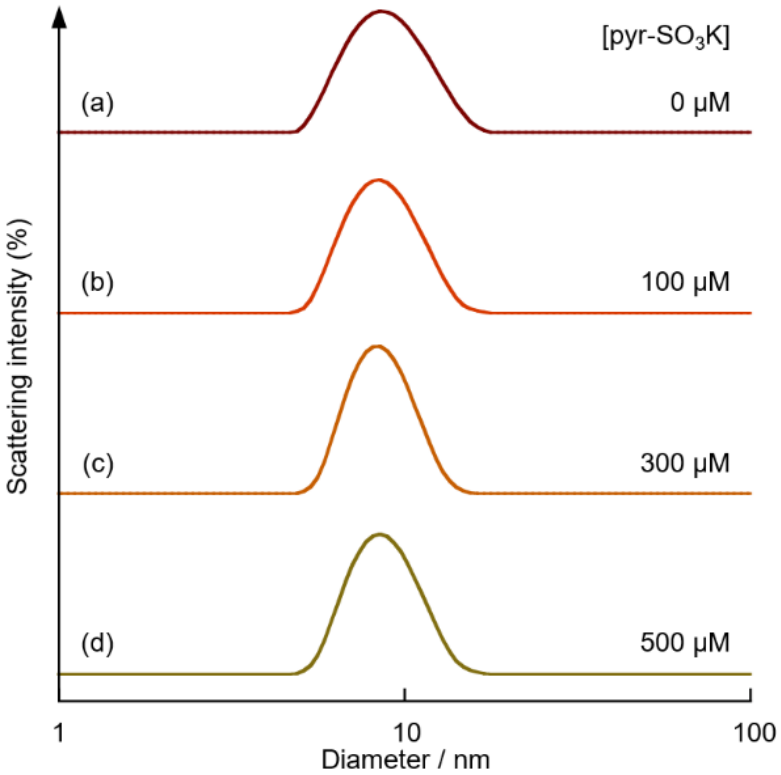

Figure 1-8. Hydrodynamic radius distributions as determined by DLS traces for 50 μM of pyr-HTHP^{V44C} with (a) 0 μM, (b) 100 μM, (c) 300 μM and (d) 500 μM of pyr-SO_3K.

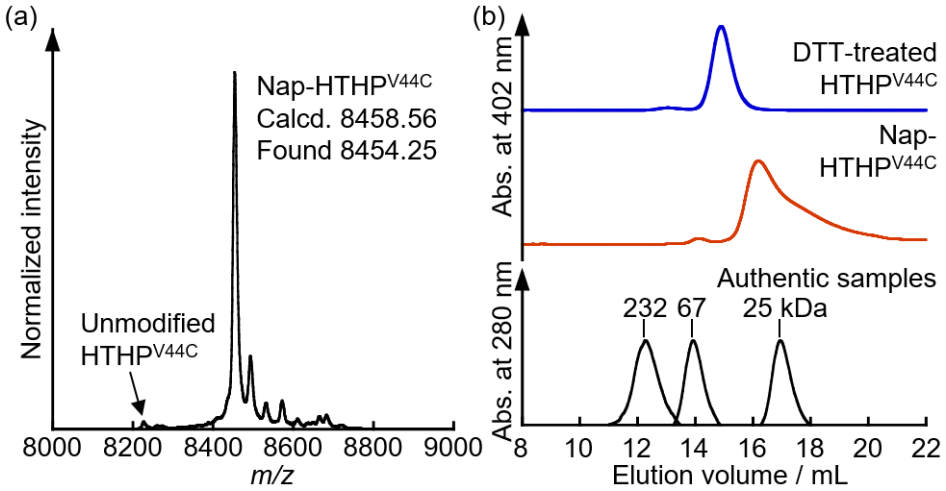

Figure 1-9. (a) MALDI-TOF mass spectrum of nap-HTHP^{V44C}. (b) SEC traces of DTT-treated HTHP^{V44C} (upper) and nap-HTHP^{V44C} (lower) with authentic samples.

HTHP^{WT}, suggesting that there may be a hydrophobic interaction between the attached naphthalene moieties and column beads. Thus, it was found that the six naphthalene moieties on the HTHP hexamer do not provide a sufficient driving force to construct the dimer of the hexamers. The difference in assembly behaviors for the naphthalene and pyrene modifications suggests that significant steric hindrance by supramolecular dimerization in the course of the modification of pyrene to HTHP^{V44C}

inhibits quantitative modification of the cysteine residue.

Surprisingly, pyr-HTHP^{V44C} forms only (pyr-HTHP^{V44C})$_2$ without any smaller components and larger aggregates, indicating that the present multivalent effect provided by the pyrene–pyrene interaction is suitably balanced. If a single pyrene–pyrene interaction was significantly stronger, larger aggregates might be formed. If multiple pyrene–pyrene interactions are too weak, dimers or other aggregates would likely not be formed and the hexamer would remain in solution.

Removal of heme and the subsequent insertion of heme in the pyrene-attached HTHP

Removal of heme from (pyr-HTHP^{V44C})$_2$ provided unique structural changes: (pyr-HTHP^{V44C})$_2$ dissociates into the hexamers. The conventional procedure to extract heme from (pyr-HTHP^{V44C})$_2$ under acidic conditions successfully provides the apoprotein as evidenced by UV–vis spectra lacking heme absorbance (Figure 1-10). In this UV–vis spectrum, the bands at 278 nm, 328 nm and 343 nm are derived from the pyrene molecule, indicating that apo-form of pyr-HTHP^{V44C}, pyr-apo-HTHP^{V44C}, was obtained and the pyrene moieties attached via covalent linkage onto the protein surface are stable against acidification. As shown in Figure 1-11, the SEC profile of the apo-form of pyr-HTHP^{V44C} has a single peak eluting at 15.1 mL, which is similar to the elution volume of the HTHP hexamer. This obviously indicates the dissociation of (pyr-HTHP^{V44C})$_2$ into the hexamers. Furthermore, the addition of heme into pyr-apo-HTHP^{V44C} is found to regenerate the (pyr-HTHP^{V44C})$_2$ which is characterized by the elution at 13.2 mL in SEC. However, other components elute earlier than the dimer of the hexamers after the reinsertion of heme into pyr-apo-HTHP^{V44C}. This result suggests formation of larger assemblies which could be driven by interprotein interactions of pyrene with the vacant heme pocket and/or misfolding. Plausible mechanisms of assembly and disassembly are

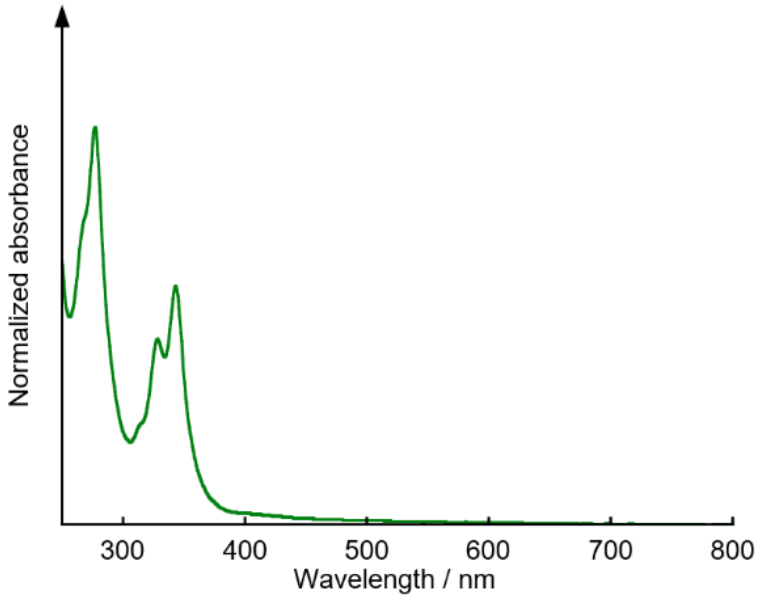

Figure 1-10. UV–vis spectrum of pyr-apo-HTHP^{V44C}.

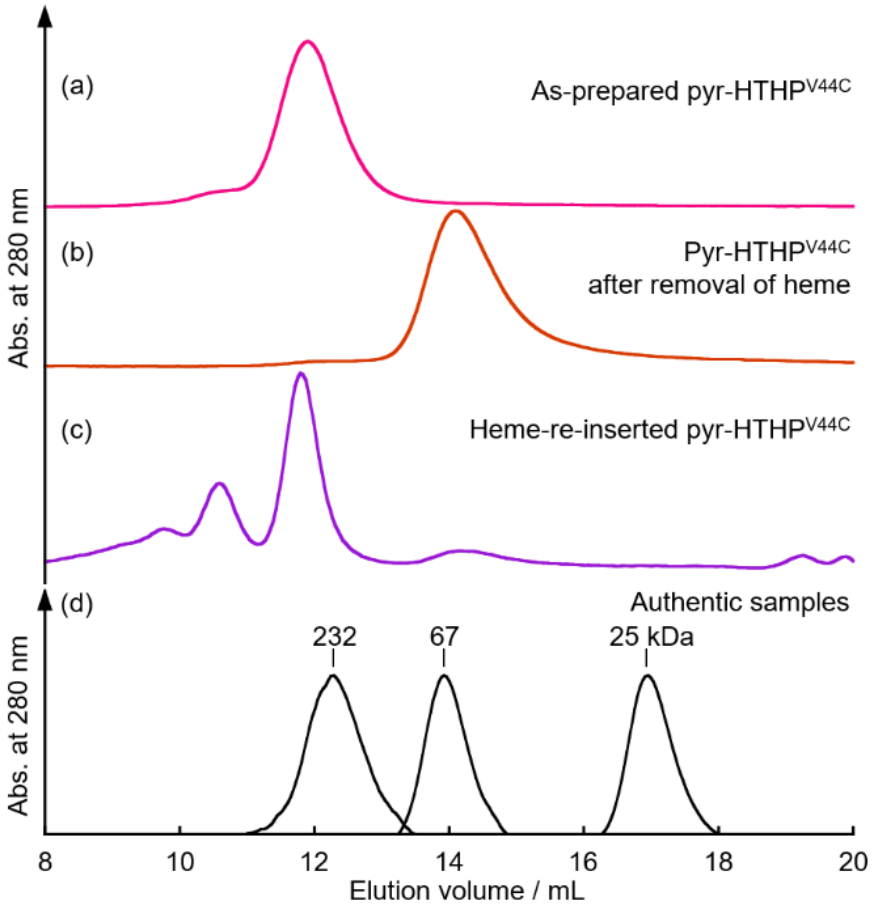

Figure 1-11. SEC traces of (a) as-prepared pyr-HTHP^{V44C}, (b) pyr-HTHP^{V44C} after removal of heme, (c) heme-re-inserted pyr-HTHP^{V44C} and (d) authentic samples.

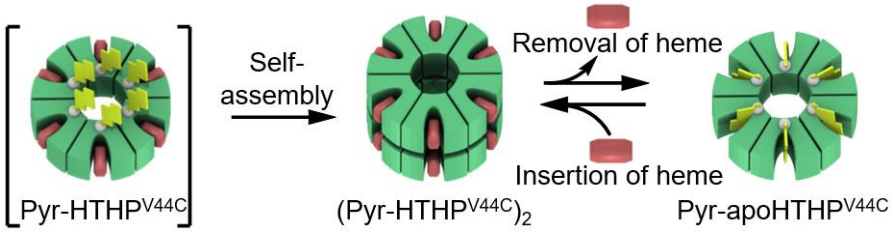

Figure 1-12. Plausible scheme for assembly and disassembly of pyr-HTHP^{V44C}.

summarized in Figure 1-12. The author suggests that insertion of the pyrene moiety into the vacant heme pocket of the apo-form provides the driving force for disassembly of (pyr-HTHP^{V44C})$_2$ into the hexamers due to the proximity effects where the pyrene molecule is attached onto Cys44 which is adjacent to Tyr45 the axial ligand for heme. Thus, the supramolecular dimerization of pyr-HTHP^{V44C} requires the presence of heme in its heme pocket. This behavior is regarded as complementary to the functionality of another assembly system where an externally heme-attached hemoprotein promotes assembly via successive heme–heme pocket interactions. In the present case, formation of the hemoprotein assembly is promoted in the absence of native heme and addition of heme induces the dissociation of the assembly.[16-19] Thus, the present study demonstrates a unique heme-dependent assembling system.

1-3. Summary

Modifications of a hexameric hemoprotein mutant with pyrene derivative, *N*-(1-pyrenyl)maleimide, at genetically introduced cysteine residues generates a stable dimer of the hexamers via a driving force provided by multiple pyrene–pyrene interactions without formation of larger aggregates and smaller components. In contrast, naphthalene-attached HTHP is found not to form the dimer of the hexamers, supporting the author's proposal that aromatic and/or hydrophobic properties of pyrene are required for formation of the stable dimer of the hexamers. In the dimer of the hexamers, the closest distance between heme molecules within the two hexamers is estimated to be ca. 3 nm, which possibly affects some physicochemical properties of heme such as magnetism. The removal of heme from the dimer of hexamers appears to trigger incorporation of pyrene into the vacant heme pocket to drive dissociation of the dimer. This is the first demonstration of an artificial protein assembly system with an assembling mechanism driven by of heme binding. The present system is expected to contribute to development of functional biomaterials which respond to the presence or absence of heme.

1-4. Experimental section

Material and methods

UV–vis absorption spectra were obtained on a Shimadzu UV-2550 or UV-3150 double-beam spectrophotometer, a JASCO V-670 UV–vis–NIR spectrophotometer (JASCO), or a Shimadzu BioSpec-nano spectrophotometer. Circular dichroism (CD) spectra were recorded on a JASCO spectropolarimeter (Model J-820). The pH values were monitored with a Horiba F-52 pH meter. Fluorescence spectra were recorded with a JASCO FP-8600 fluorescence spectrophotometer. MALDI-TOF MS analyses were performed with a Bruker autoflex III mass spectrometer and sinapic acid was used as a matrix reagent. Size exclusion chromatographic (SEC) analyses were performed using a Superdex 200 Increase 10/300 GL (GE Healthcare) column with an ÄKTApurifier system (GE Healthcare) at 4 ºC. Dynamic light scattering (DLS) measurements were performed using a Zetasizer μV (Malvern Instruments) with an 830 nm laser at 25 ºC. Ultrapure water (Milli-Q) was demineralized using a Merk Millipore Integral 3 apparatus. *N*-(1-pyrenyl)maleimide was purchased from TCI. Other all reagents were of the highest guaranteed grade commercially available and were used as received unless otherwise indicated.

Protein sequence of HTHP and its mutant

Wild type HTHP:
SETWLPTLVTATPQEGFDLAVKLSRIAVKKTQPDAQVRDTLRAVYEKDANALIAVSAVVATHF
QTIAAANDYWKD.
HTHP V44C mutant ($HTHP^{V44C}$):

SETWLPTLVTATPQEGFDLAVKLSRIAVKKTQPDAQVRDTLRACYEKDANALIAVSAVVATHF QTIAAANDYWKD.

Expression and purification of HTHP^{V44C}

The gene expression system for wild type HTHP was reported in the previous paper.[40] The single-point mutation was performed by the polymerase chain reaction (PCR) using LA PCR in vitro Mutagenesis Kit (Takara) according to the protocol of the manufacture. The HTHP gene cloned into pDEST14 was used as a template to introduce V44C single-point mutation into the HTHP matrix. The primer sequence used to generate the mutant was (5'-GTTCGCGATACTCTCCGTGCTTGCTATGAGAAAGATGCGAATGCG-3') and the complementary primer.

After PCR, the template plasmids were digested with DpnI (Thermo Fisher Scientific). *E. Coli*. DH5α competent cells were transformed with PCR products. After the cultivation, the plasmids were purified with PureLink^{TM} Quick Plasmid Miniprep Kit (Thermo Fisher Scientific). DNA sequencing was performed to verify the correct mutation in the gene sequence. The resulting expression plasmid was used to transform *E. Coli*. BL21(DE3). LB medium (3 L) containing ampicillin (300 mg) was inoculated with 50 mL of a culture (OD600 = 0.7) of the transformed cells. After the cells were grown aerobically with vigorous shaking at 37 ºC until OD600 reached 0.7, isopropyl-β-D-1-thiogalactopyranoside (IPTG, 1 mM as a final concentration) was added to the culture for induction of protein expression. The culture was continued at 37 ºC overnight. The cells were harvested by centrifugation at 3200 x g for 10 min. The harvested cells from 3 L of culture were re-suspended in ca. 50 mL of a 10 mM Tris-HCl buffer, pH 8.0, and lysed by freeze–thaw cycles with subsequent sonication for 30 sec x 10 times at 4 ºC. The lysate was then centrifuged and the supernatant was collected. The excess amount of hemin chloride (800 μM in 100 mM $NaOH_{aq}$) was added to the solution and stirred for 10 min at 4 ºC. The solution was then incubated at 80 ºC for 10 min and the precipitate was removed by centrifugation at 8000 rpm for 10 min. The solution was loaded onto a DEAE Fast Flow (GE Healthcare) anion-exchange column pre-equilibrated with 10 mM potassium phosphate buffer at pH 6.0. The fraction of the target protein was collected in 10 mM potassium phosphate buffer at pH 6.0 containing 0.3 M NaCl. The obtained solution was concentrated using an Amicon stirred ultrafiltration cell with a 10 kDa molecular weight cut-off membrane (Millipore). The concentrated solution was passed through a Sephacryl S-200 column equilibrated with 100 mM potassium phosphate buffer at pH 7.0. The fractions with $R_z > 2.5$ (R_z is a ratio of absorbance values at 402 nm and 280 nm) were collected and concentrated. The obtained Cys-introduced HTHP mutants was characterized by SDS-PAGE and MALDI-TOF MS, and stored at –80 ºC.

Preparation of pyrene-attached HTHP^{V44C}

An aqueous solution of 1 M DTT_{aq} (100 μL) was added to HTHP^{V44C} (500 μM, 900 μL) and incubated for 1 h at 50 ºC. DTT was removed using a HiTrap Desalting column (eluent: 100 mM

potassium phosphate buffer at pH 7.0) and the obtained protein solution was diluted to 20 μM (22.5 mL). A dimethylsulfoxide (DMSO) solution of *N*-(1-pyrenyl)maleimide (5 mM, 450 μL) was added into a protein solution and incubated for 1 h at 25 ºC. The excess *N*-(1-pyrenyl)maleimide was removed using a HiTrap Desalting column and purified using a Superdex 200 Increase 10/300 GL column (eluent: 100 mM potassium phosphate buffer at pH 7.0 and 4 ºC). The obtained protein was characterized by MALDI-TOF MS, analytical SEC measurements and UV–vis spectroscopy.

Removal of heme from pyrene-attached HTHP^{V44C}

Removal of heme was performed using Teale's method[54] as follows: a solution of pyrene-attached HTHP^{V44C} (50 μM as a monomer) in 150 mM of L-histidine solution at 4 ºC was acidified to pH 1.7 upon addition of 1 M HCl_{aq}. Unbound heme was extracted with 2-butanone (5 times) and the solution was neutralized by dialysis with 100 mM potassium phosphate buffer at pH 7.0 and 4 ºC (4 times). The obtained apo-form of pyrene-attached HTHP^{V44C} was characterized by analytical SEC measurements and UV–vis spectroscopy.

Reconstitution of pyrene-attached HTHP^{V44C}

One equivalent of hemin (0.81 mM, 48 μL) in 100 mM $NaOH_{aq}$ was added to a solution of the apo-form of pyrene-attached HTHP^{V44C} (1.0 μM, 30 mL) in 100 mM potassium phosphate buffer at pH 7.0 and incubated for 1 h at 4 ˚C. The solution was loaded onto a DEAE Fast Flow (GE Healthcare) anion-exchange column pre-equilibrated with 100 mM potassium phosphate buffer at pH 7.0. The fraction of the target protein was collected in 100 mM potassium phosphate buffer at pH 7.0 containing 0.5 M NaCl. NaCl was removed by an HiTrap Desalting column. Completion of reconstitution was confirmed by UV–vis spectroscopy.

Preparation of naphthalene-attached HTHP^{V44C}

The 1 M DTT_{aq} (20 μL) was added to a HTHP^{V44C} solution (500 μM, 180 μL) and incubated for 1 h at 50 ºC. DTT was removed using a HiTrap Desalting column (eluent: 100 mM potassium phosphate buffer at pH 7.0) and the obtained protein solution was diluted to 20 μM (4.5 mL). A dimethylsulfoxide (DMSO) solution of *N*-(1-naphthyl)maleimide (5 mM, 90 μL) was added into the protein solution and incubated for 1 h at 25 ºC. The excess *N*-(1-naphthyl)maleimide was removed using a HiTrap Desalting column. The obtained protein was characterized by MALDI-TOF MS, and analytical SEC measurements.

Analytical SEC measurements

For SEC analysis, 100 mM potassium phosphate buffer at pH 7.0 was used as an eluent. The analysis performed at 4 ºC at a flow rate of 0.5 mL/min with monitoring of the absorbance at 280 or 402 nm for detection. The Superdex 200 Increase 10/300 GL column (GE Healthcare) was calibrated using the following reagents: catalase (232 kDa), albumin (67 kDa) and chymotripsinogen (25 kDa).

DLS measurements

For DLS measurements, 100 mM potassium phosphate buffer at pH 7.0 was used as a solvent. To analyze the protein solution, a 12 μL quartz cuvette was utilized. Prior to placement of the solution into the cuvette, the sample was filtered using a 0.22-μm filter. The cuvette was inserted into the apparatus for 5 min to obtain equilibration at the desired temperature before the measurement was performed. The signals were processed in protein analysis mode. The data were obtained by the number-based particle size distribution mode.

References

1. van Dun, S.; Ottmann C.; Milroy, L. G.; Brunsveld, L. *J. Am. Chem. Soc.* **2017**, *139*, 13960-13968.
2. Luo, Q.; Hou, C.; Bai, Y.; Wang, R.; Liu, J. *Chem. Rev.* **2016**, *116*, 13571-13632.
3. Sun, H.; Luo, Q.; Hou, C.; Liu, J. *Nano Today* **2017**, *14*, 16-41.
4. Churchfield, L. A.; Tezcan, F. A. *Acc. Chem. Res.* **2019**, *52*, 345-355.
5. Kobayashi, N.; Arai, R. *Curr. Opin. Biotech.* **2017**, *46*, 57-65.
6. Fegan, A.; White, B.; Carlson, J. C. T.; Wagner, C. R. *Chem. Rev.* **2010**, *110*, 3315-3336.
7. Oohora, K.; Hayashi, T. *Curr. Opin. Chem. Biol.* **2014**, ***19***, 154-161.
8. Hirota, S. *J. Inorg. Biochem.* **2019**, *194*, 170-179.
9. Lai, Y. T.; Cascio, D.; Yeates, T. O. *Science* **2012**, *336*, 1129.
10. Hsia, Y.; Bale, J. B.; Gonen, S.; Shi, D.; Sheffler, W.; Fong, K. K.; Nattermann, U.; Xu, C.; Huang, P.; Ravichandran, R.; Yi, S.; Davis, T. N.; Gonen, T.; King, N. P.; Baker, D. *Nature* **2016**, *535*, 136-139.
11. Simon, A. J.; Zhou, Y.; Ramasubramani, V.; Glaser, J.; Pothukuchy, A.; Gollihar, J.; Gerberich, J. C.; Leggere, J. C.; Morrow, B. R.; Jung, C.; Glotzer, S. C.; Taylor, D. W.; Ellington, A. D. *Nat. Chem.* **2019**, *11*, 204-212.
12. Burazerovic, S.; Gradinaru, J.; Pierron, J.; Ward, T. R. *Angew. Chem. Int. Ed.* **2007**, *46*, 5510-5514.
13. Pires, M. M.; Chmielewski, J. *J. Am. Chem. Soc.* **2009**, *131*, 2706-2712.
14. Munch, H. K.; Heide, S. T.; Christensen, N. J.; Hoeg-Jensen, T.; Thulstrup, P. W.; Jensen, K. J. *Chem. Eur. J.* **2011**, *17*, 7198-7204.
15. Bai, Y.; Luo, Q.; Zhang, W.; Miao, L.; Xu, J.; Li, H.; Liu, J. *J. Am. Chem. Soc.* **2013**, *135*, 10966-10969.
16. Oohora, K.; Onoda, A.; Hayashi, T. *Chem. Commun.* **2012**, *48*, 11714-11726.
17. Oohora, K.; Burazerovic, S.; Onoda, A.; Wilson, Y. M.; Ward, T. R.; Hayashi, T. *Angew. Chem. Int. Ed.* **2012**, *51*, 3818-3821.
18. Oohora, K.; Fujimaki, N.; Kajihara, R.; Watanabe, H.; Uchihashi, T.; Hayashi, T. *J. Am. Chem. Soc.* **2018**, *140*, 10145-10148.

19. Oohora, K.; Kajihara, R.; Fujimaki, N.; Uchihashi, T.; Hayashi, T. *Chem. Commun.* **2019**, *55*, 1544-1547.
20. Carlson, J. C. T.; Jena, S. S.; Flenniken, M.; Chou, T.; Siegel, R. A.; Wagner, C. R. *J. Am. Chem. Soc.* **2006**, *128*, 7630-7638.
21. Nguyen, H. D.; Dang, D. T.; van Dongen, J. L. J.; Brunsveld, L. *Angew. Chem. Int. Ed.* **2010**, *49*, 895-898.
22. Hou, C.; Li, J.; Zhao, L.; Zhang, W.; Luo, Q.; Dong, Z.; Xu, J.; Liu, J. *Angew. Chem. Int. Ed.* **2013**, *52*, 5590-5593.
23. Hou, C.; Huang, Z.; Fang, Y.; Liu, J. *Org. Biomol. Chem.* **2017**, *15*, 4272-4281.
24. Dang, D. T.; Schill, J.; Brunsveld, L. *Chem. Sci.* **2012**, *3*, 2679-2684.
25. Bastings, M. M. C.; de Greef, T. F. A.; van Dongen, J. L. J.; Merkx, M.; Meijer, E. W. *Chem. Sci.* **2010**, *1*, 79-88.
26. Radford, R. J.; Tezcan, F. A. *J. Am. Chem. Soc.* **2009**, *131*, 9136-9137.
27. Hirota, S.; Hattori, Y.; Nagao, S.; Taketa, M.; Komori, H.; Kamikubo, H.; Wang, Z.; Takahashi, I.; Negi, S.; Sugiura, Y.; Kataoka, M.; Higuchi, Y. *Proc. Natl. Acad. Sci. USA* **2010**, *107*, 12854-12859.
28. Suzuki, Y.; Cardone, G.; Restrepo, D.; Zavattieri, P. D.; Baker, T. S.; Tezcan, F. A. *Nature* **2016**, *533*, 369-373.
29. Gonen, S.; DiMaio, F.; Gonen, T.; Baker, D. *Science* **2015**, *348*, 1365-1368.
30. Sinclair, J. C.; Davies, K. M.; Venien-Bryan, C.; Noble, M. E. M. *Nat. Nanotechnol.* **2011**, *6*, 558-562.
31. Brodin, J. D.; Smith, S. J.; Carr, J. R.; Tezcan, F. A. *J. Am. Chem. Soc.* **2015**, *137*, 10468-10471.
32. Komatsu, T.; Qu, X.; Ihara, H.; Fujihara, M.; Azuma, H.; Ikeda, H. *J. Am. Chem. Soc.* **2011**, *133*, 3246-3248.
33. Sendai, T.; Biswas, S.; Aida, T. *J. Am. Chem. Soc.* **2013**, *135*, 11509-11512.
34. Miyamoto, T.; Kuribayashi, M.; Nagao, S.; Shomura, Y.; Higuchi, Y.; Hirota, S. *Chem. Sci.* **2015,** *6*, 7336-7342.
35. Ni, T. W.; Tezcan, F. A. *Angew. Chem. Int. Ed.* **2010**, *49*, 7014-7018.
36. Bale, J. B.; Gonen, S.; Liu, Y.; Sheffler, W.; Ellis, D.; Thomas, C.; Cascio, D.; Yeates, T. O.; Gonen, T.; King, N. P.; Baker, D. *Science* **2016**, *353*, 389-394.
37. Kawakami, N.; Kondo, H.; Matsuzawa, Y.; Hayasaka, K.; Nasu, E.; Sasahara, K.; Arai, R.; Miyamoto, K. *Angew. Chem., Int. Ed.* **2018**, *57*, 12400-12404.
38. Song, W. J.; Tezcan, F. A. *Science* **2014**, *346*, 1525-1528.
39. Miao, L.; Han, J.; Zhang, H.; Zhao, L.; Si, C.; Zhang, X.; Hou, C.; Luo, Q.; Xu, J.; Liu, J. *ACS Nano* **2014**, *8*, 3743-3751.
40. Oohora, K.; Mashima, T.; Ohkubo, K.; Fukuzumi, S.; Hayashi, T. *Chem. Commun.* **2015**, *51*, 11138-11140.
41. Mashima, T.; Oohora, K.; Hayashi, T. *Phys. Chem. Chem. Phys.* **2018**, *20*, 3200-3209.

42. Biswas, S.; Kinbara, K.; Niwa, T.; Taguchi, H.; Ishii, N.; Watanabe, S.; Miyata, K.; Kataoka, K.; Aida, T. *Nat. Chem.* **2013**, *5*, 613-620.
43. Li, Q.; So, C. R.; Fegan, A.; Cody, V.; Sarikaya, M.; Vallera, D. A.; Wagner, C. R. *J. Am. Chem. Soc.* **2010**, *132*, 17247-17257.
44. Oohora, K.; Kajihara, R.; Jiromaru, M.; Kitagishi, H.; Hayashi, T. *Chem. Lett.* **2019**, *48*, 295-298.
45. Yang, G.; Zhang, X.; Kochovski, Z.; Zhang, Y.; Dai, B.; Sakai, F.; Jiang, L.; Lu, Y.; Ballauff, M.; Li, X.; Liu, C.; Chen, G.; Jiang, M. *J. Am. Chem. Soc.* **2016**, *138*, 1932-1937.
46. Sakai, F.; Yang, G.; Weiss, M. S.; Liu, Y.; Chen, G.; Jiang, M. *Nat. Commun.* **2014**, *5*, 4634.
47. Milton, R. D.; Wang, T.; Knoche, K. L.; Minteer, S. D. *Langmuir* **2016**, *32*, 2291-2301.
48. Lalaoui, N.; Rousselot-Pailley, P.; Robert, V.; Mekmouche, Y.; Villalonga, R.; Holzinger, M.; Cosnier, S.; Tron, T.; Goff, A. L. *ACS Catal.* **2016**, *6*, 1894-1900.
49. Holder, P. G.; Francis, M. B. *Angew. Chem. Int. Ed.* **2007**, *46*, 4370-4373.
50. Bains, G.; Patel, A. B.; Narayanaswami, V. *Molecules* **2011**, *16*, 7909-7935.
51. Fujii, A.; Sekiguchi, Y.; Matsumura, H.; Inoue, T.; Chung, W. S.; Hirota, S.; Matsuo, T. *Bioconjugate Chem.* **2015**, *26*, 537-548.
52. Benni, I.; Trabuco, M. C.; Stasio, E. D.; Arcovito, A.; Boffi, A.; Malatesta, F.; Bonamore, A.; Panfilis, S. D.; de Turris, V.; Baiocco, P. *RSC Adv.* **2018**, *8*, 12815-12822.
53. Jeoung, J. H.; Pippig, D. A.; Martins, B. M.; Wagener, N.; Dobbek, H. *J. Mol. Biol.* **2007**, *368*, 1122-1131.
54. Teale, F. W. J. *Biochem. Biophys. Acta* **1959**, *35*, 543.

Chapter 2
Construction of HTHP Sheet and Direct Observation of Dynamic Process of Its Formation

2-1. Introduction

Artificial protein assemblies have recently emerged as an important research area[1-2] and various artificially one-, two-, and three-dimensional protein assemblies have been reported.[3-16] Artificial two-dimensional protein assemblies have recently been found to generate protein sheets with nanometer-scale thickness while demonstrating attractive functions required for development of auxetic materials[7] and light-harvesting systems.[8] The most common strategy used in construction of the artificial protein sheets requires connection of C_3-, C_4- or C_6-symmetric protein oligomers through C_2-symmetric linkages.[8,10] Such symmetric protein oligomers are easily found in protein databases containing protein crystal structures. Thus, it is necessary to utilize suitable linkages connecting the protein units to obtain the protein sheets. According to previous reports, several types of linkage have been used in constructing the artificial protein sheets: (i) native-like protein–protein interactions,[10,11] (ii) dative bonding,[7,12] (iii) covalent bonding,[7-9] and (iv) specific hydrophobic interactions.[13] However, to the best of the author's knowledge, protein sheets assembled using a chemically-controlled host–guest interaction has not been previously reported although this interaction is useful for creating protein assemblies.[3,5,17-20] A reversible and moderate interprotein interaction is appropriate to generate protein sheets because significantly strong and/or irreversible interactions could result in the formation of dendritic assemblies unless the structures are accurately designed. The author focused on a C_2-symmetrical host–guest complex constructed by one cucurbit[8]uril (CB8) molecule and two FGG tripeptide tags,[21] which were previously used by Liu's group and Brunsveld's group individually to provide a driving force for construction of the artificial protein assemblies.[17-19] As a building block, we employed hexameric tyrosine coordinated heme protein (HTHP) because of its robustness (T_m > 130 ºC), C_6-symmetric cylindrical shape and visibly confirmable color derived from the heme chromophore.[22,23] The present study demonstrates construction of HTHP sheets via multiple interactions between CB8 and FGG tags without any support provided by a flat substrate and also demonstrates direct observation of the dynamic process of formation of the sheets on a substrate (Figure 2-1).

2-2. Results and discussion

Modification of HTHP with maleimide-linked FGG tripeptide

For preparation of FGG-attached HTHP (FGG-HTHP) the author employed the chemical modification method reported by Liu.[17] The FGG tripeptide with a maleimide group linked via an ethylene diamine linker (mFGG) was synthesized as Liu previously reported and introduced onto the

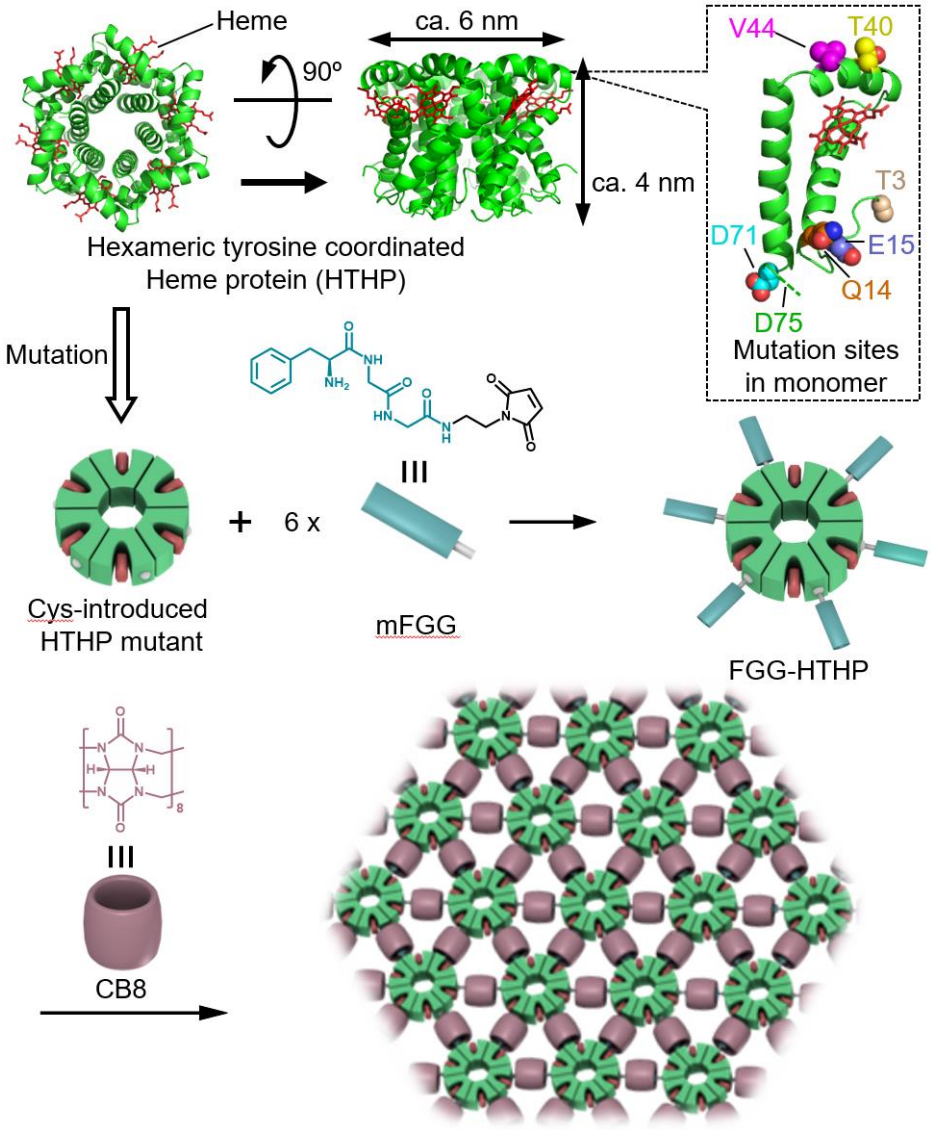

Figure 2-1. Crystal structure of HTHP (PDB ID: 2OYY) and schematic representation of the assembling system of FGG-HTHP induced by CB8. The mutation sites of each monomer unit are shown in the upper right corner. The disordered C-terminal residues are indicated by the green broken line.

surface of target protein by the specific reaction of the maleimide moiety with a cysteine residue. For this reaction, seven cysteine-introduced single mutants, HTHP^{T3C}, HTHP^{Q14C}, HTHP^{E15C}, HTHP^{T40C}, HTHP^{V44C}, HTHP^{D71C}, and HTHP^{D75C}, were prepared. The cysteine-introduced position of each mutant is displayed in Figure 2-1. Each mutant has a single cysteine residue per each monomer unit because wild type HTHP lacks cysteine residues. Thus, a total of six cysteine residues were introduced into each of the hexamers. Each of mutants was successfully modified with mFGG to obtain modified proteins. The modified proteins were characterized by MALDI-TOF mass spectroscopy (Figure 2-2).

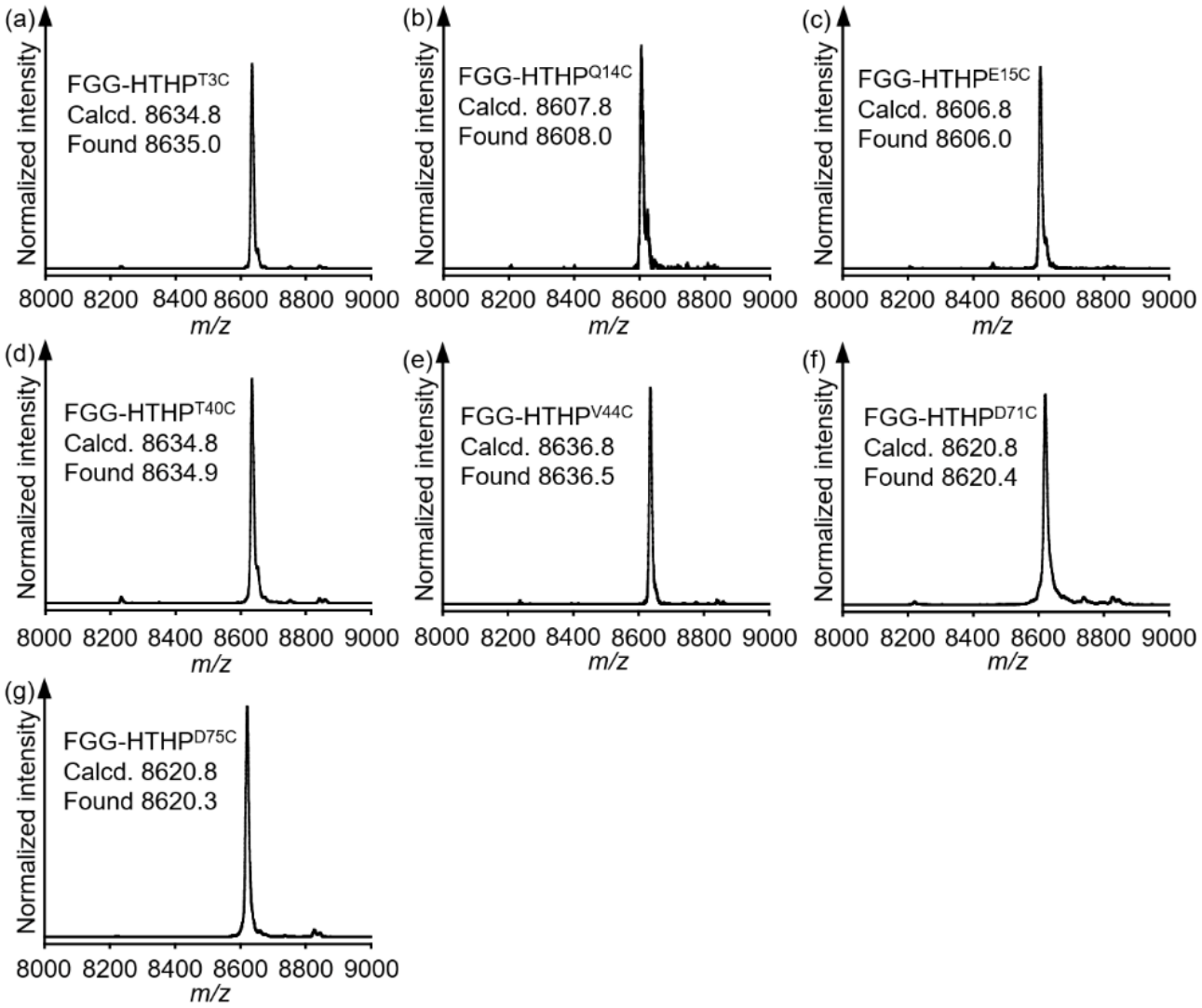

Figure 2-2. MALDI mass spectra of FGG-HTHPs. (a) FGG-HTHP^{T3C}, (b) FGG-HTHP^{Q14C}, (c) FGG-HTHP^{E15C}, (c) FGG-HTHP^{E15C}, (d) FGG-HTHP^{T40C}, (e) FGG-HTHP^{V44C}, (f) FGG-HTHP^{D71C} (g) FGG-HTHP^{D75C}

Screening of mutants for the construction of protein assembly

First, the author visually screened the FGG-HTHPs for assembly behavior upon addition of a stoichiometric amount of CB8: FGG-HTHPs (50 μM as a monomer) were mixed with a stoichiometric amount of CB8 (25 μM) in 50 mM potassium phosphate buffer, pH 7.0. As a result, only FGG-HTHP^{Q14C} and FGG-HTHP^{E15C} provided precipitates after addition of CB8 and centrifugation, whereas the other five FGG-HTHP mutants did not provide precipitates (Figure 2-3a). These results indicate that the mutants forming precipitates generate a large assembly and the other five mutants either form a small assembly or fail to assemble. Additionally, the results of optical microscopic images shown in Figure 2-3b obviously distinguish between two macroscopic shapes of CB8-inducing precipitates formed by FGG-HTHP^{Q14C} and FGG-HTHP^{E15C}. Assembly of FGG-HTHP^{Q14C} in the presence of CB8 affords film with a length of a few hundred micrometers whereas FGG-HTHP^{E15C}

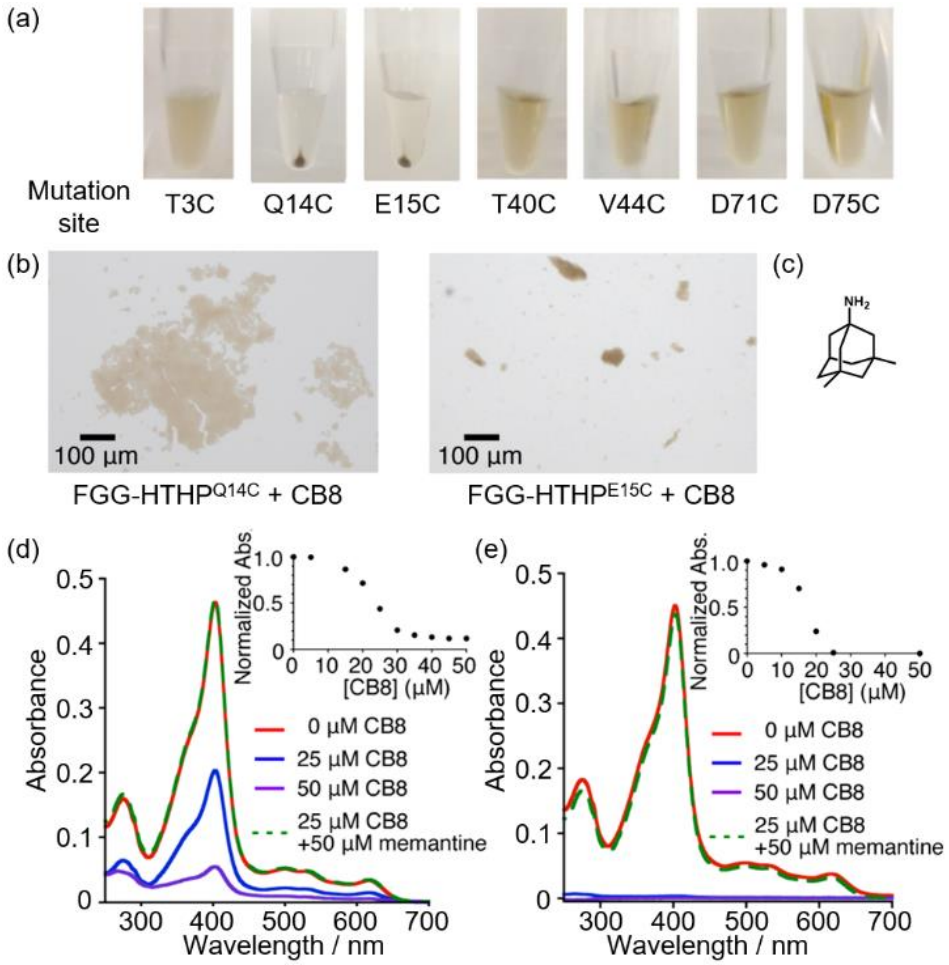

Figure 2-3. (a) Photographs of FGG-HTHP solutions (50 µM) taken after addition of CB8 (25 µM) and centrifugation. (b) Optical microscopic images of precipitates generated upon addition of CB8 (25 µM) into FGG-HTHP^{Q14C} and FGG-HTHP^{E15C} solutions (50 µM). (c) Molecular structure of memantine. (d and e) UV–vis absorption spectra of supernatants; (d) FGG-HTHP^{Q14C} and (e) FGG-HTHP^{E15C} solutions (50 µM) upon addition of various concentrations of CB8 and the following addition of 50 µM memantine. The insets of (c) and (d) show the plots of absorbance at 402 nm against the concentration of CB8. The absorbance is normalized with respect to the Soret-band of HTHP in the absence of CB8.

forms small amorphous precipitates upon addition of CB8. Thus, further observation and analysis were conducted about FGG-HTHP^{Q14C} and FGG-HTHP^{E15C}. The UV–vis spectra of supernatants after centrifugation to remove precipitates in the solutions of FGG-HTHP^{Q14C} and FGG-HTHP^{E15C} indicate that 56% and 100% of protein components are consumed in generation of precipitating assemblies upon addition of stoichiometric CB8, respectively (Figure 2-3d,e). Furthermore, both of the precipitates can be quantitatively dissolved again upon addition of memantine hydrochloride (Figure 2-3c) as a competitive guest for CB8 as shown by green broken lines in Figure 2-3d,e.[25] Thus, the precipitates are clearly provided by the ternary interaction between FGG and CB8. Although an

accurate binding constant of CB8 for FGG-tags attached to protein has not been determined,[26] a previous investigation has determined that quantitative dimerization requires over 20 μM CB8 for 20 μM of a monomeric FGG-tagged protein.[19a] In this work, the micrometer-sized precipitates, which assemble using hundreds of FGG-HTHP units, are clearly obtained with concentrations less than 50 μM FGG-HTHP and 25 μM CB8. Thus, it is evident that a cooperative interaction between FGG and CB8 occurs in the present systems using FGG-HTHP^{Q14C} and FGG-HTHP^{E15C}.

Evaluation of size and formation process of assembly in the solution

Dynamic light scattering (DLS) measurements were carried out to investigate the size and formation process in the solution. Figure 2-4 summarizes the DLS results. While the hydrodynamic diameter, D_h, of mixture of 50 μM FGG-HTHP^{Q14C} and 10 μM CB8 was determined to be ca. 9-10 nm, the sample using 15 and 20 μM CB8 afforded the hundreds nm-sized assembly in spite of stoichiometrically insufficient concentration. Stoichiometric assembly of FGG-HTHP^{Q14C} shows D_h over micrometer, which is almost out of range of DLS measurements. Next, time-dependency of D_h in the stoichiometric CB8-inducing assembly of FGG-HTHP^{Q14C} was investigated. Within 15 min after mixing the two components, hundreds nanometer-sized assembly forms and then the large assembly over micrometer of D_h is obtained 45 min later. Thus, the formation of the assembly is relatively fast against previously reported several protein sheets by covalent bond, which requires the reaction time from overnight to days.[7,9] Even under low protein concentration, assembly is obtained and its size reached to 144 nm and 43 nm D_h in 10 μM and 5 μM FGG-HTHP^{Q14C}, respectively (Figure 2-4c). In the case of FGG-HTHP^{E15C}, mostly similar assembling behavior is revealed. In the less amount of CB8 (10 μM) relative to FGG-HTHP^{Q14C}, the hundreds nanometer-sized assembly was observed and the stoichiometric assembly yields D_h over 1 μm. These results are consistent with aforementioned assembling behaviors using UV–vis spectral changes. In contrast, other FGG-attached HTHP mutants (T3C, T40C, V44C, D71C and D75C) appear to show no or inefficient cooperative interaction possibly due to the structural factors including steric hindrance and/or electrostatic repulsion resulting in dimer and small assemblies upon addition of CB8 (Figure 2-5).[24]

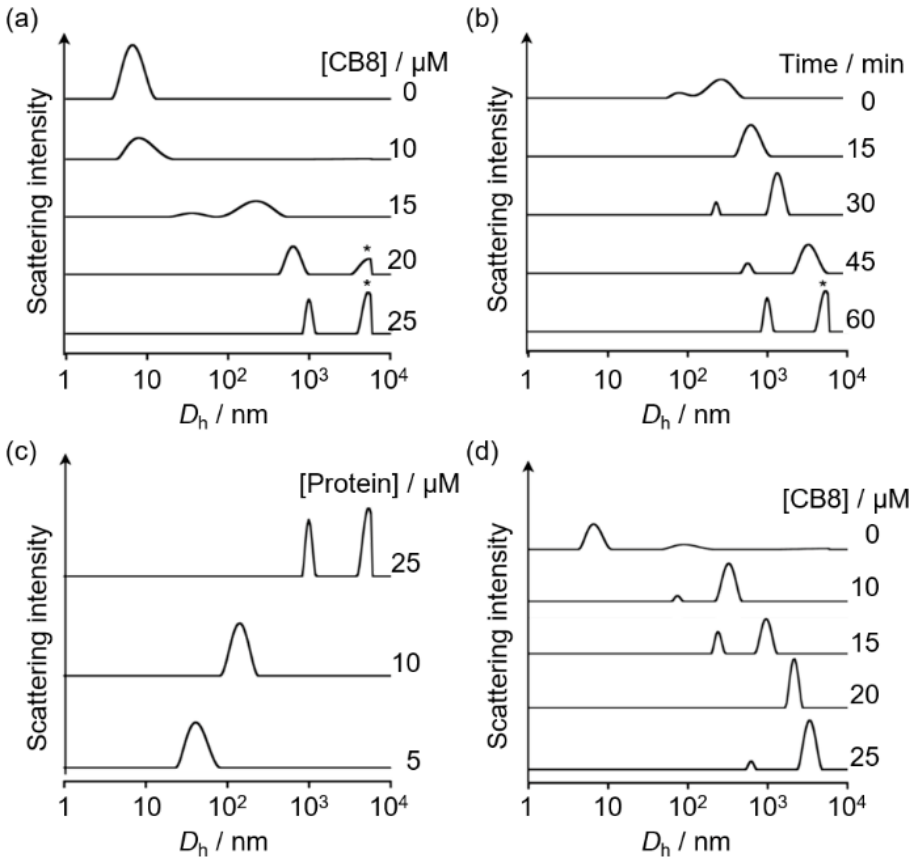

Figure 2-4. DLS results. (a) Assembly of FGG-HTHP^{Q14C} (50 μM) upon addition of various concentration of CB8. (b) Time dependent assembling behavior of FGG-HTHP^{Q14C} (50 μM) upon addition of CB8 (25 μM). (c) Assembly of various concentration of FGG-HTHP^{Q14C} upon addition of stoichiometric CB8. (d) Assembly of FGG-HTHP^{E15C} (50 μM) upon addition of various concentration of CB8. Asterisks indicate not reliable peaks due to too large D_h in the DLS measurements.

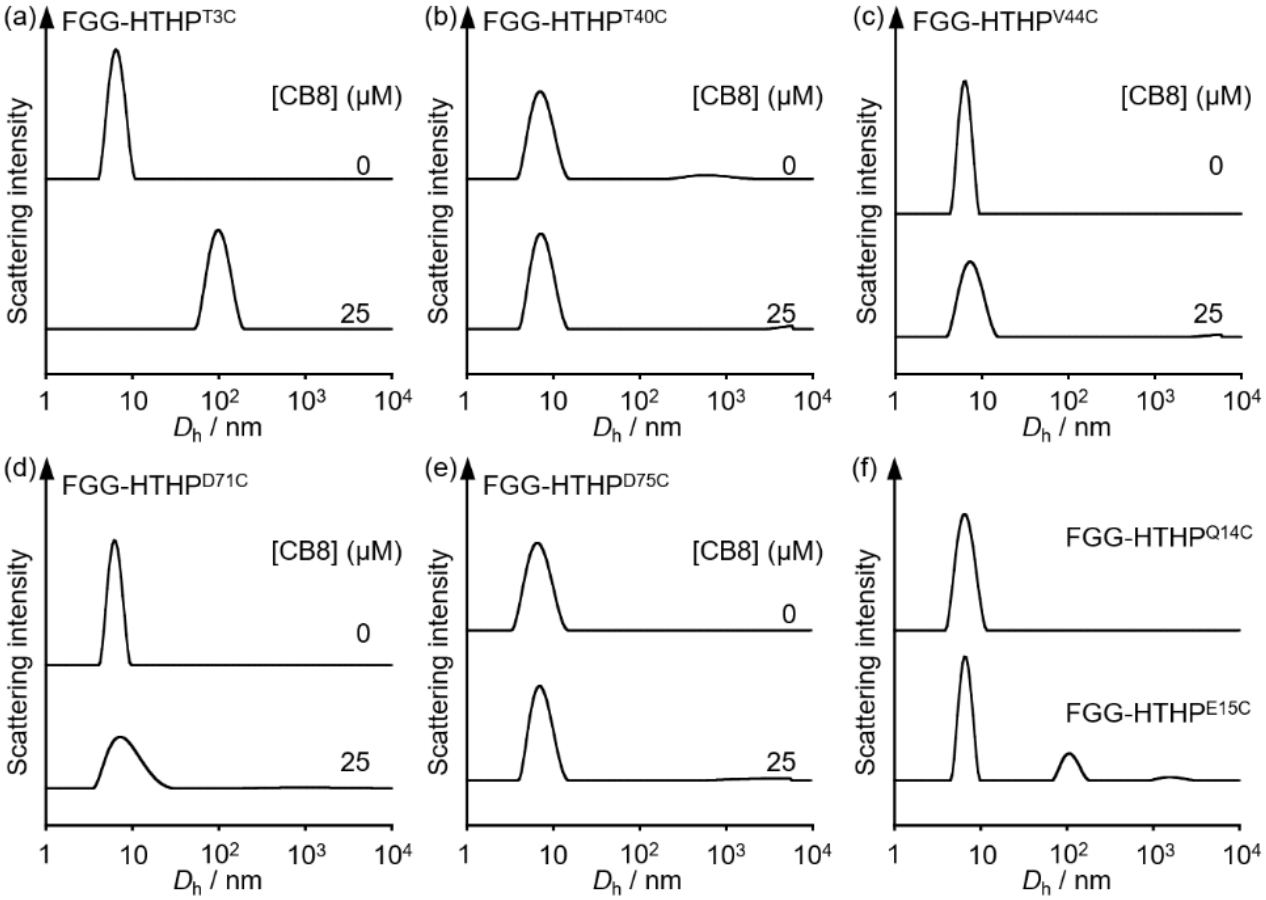

Figure 2-5. Hydrodynamic diameter distributions resulted by DLS measurements. (a) FGG-HTHP^{T3C}, (b) FGG-HTHP^{T40C}, (c) FGG-HTHP^{V44C}, (d) FGG-HTHP^{D71C}, (e) FGG-HTHP^{D75C} with CB8 (0 or 25 μM). (f) FGG-HTHP^{Q14C} or FGG-HTHP^{E15C} with CB8 (25 μM) and memantine hydrochloride (50 μM). The protein concentration is 50 μM in all measurements.

Atomic force microscopic measurements of the sheet-type two-dimensional assembly

Detailed structures were studied by high-speed atomic force microscopy (HS-AFM). The assembly prepared by mixing FGG-HTHP^{Q14C} (50 μM) and a stoichiometric amount of CB8 (25 μM) in the solution state for 30 min without a solid support was casted on mica after a 30-fold dilution and the substrate was then washed to remove excess proteins before the measurement (Figure 2-6a). Surprisingly, the sheet with a uniform height between 4 nm and 6 nm covers the mica substrate. Moreover, measurement of a solution diluted 100-fold relative to the 30-fold diluted solution indicates the presence of fragments of the sheet which has a length of hundreds nanometer, as well as the characteristic center pore of the HTHP unit (Figure 2-6b). The AFM simulations were performed based on the energy-minimized model of heptamer of HTHP, in which free mFGG units are omitted. Two orientations were considered in these simulations due to the structure of HTHP. The model in Figure 2-7a is likely a more accurate representation relative to the middle model (Figure 2-7b) because the pore is clearly observed in the experimental images (Figure 2-6b). This finding suggests that most of the HTHP units are arrayed in the same orientation. The experimentally determined height of assembly is ca. 4 nm, which is consistent with the result of the simulation. In contrast, several protein structures are found to have a height of 6 nm. This difference of height is believed to occur as result of the proteins lying sideways. This behavior appears to be induced by a vertical orientation of FGG-HTHP against the sheet, which is supported by experimental observations and simulated results (Figure 2-7c). Rotation events of FGG-HTHP can be observed in the HS-AFM measurements. This behavior suggests that the protein sheet is generated via reversible and dynamic interactions. In the case of FGG-HTHP^{E15C}, the 5-min incubation after preparation of the assembly by addition of a stoichiometric amount of CB8 in the solution state without any support induces the protein sheet to cover the mica substrate (Figure 2-6c, d). However, some of relatively large clusters which have heights ranging from 10 nm to 25 nm were seen, unlike the assembly of FGG-HTHP^{Q14C}. This appears to be caused by the formation of undesirable assemblies which may have dendritic structures. The height of the sheet of FGG-HTHP^{E15C} ranges from 4 nm to 6 nm and is more dispersed than that of the FGG-HTHP^{Q14C} sheet. Although the Q14 residue is neighboring to the E15 residue, the assembly behaviors of FGG-HTHP^{Q14C} and FGG-HTHP^{E15C} are quite different. This could be due to the side chain position at Q14 being less flexible, as it is surrounded by several bulky side chains, whereas the E15 position has less steric hindrance (Figure 2-8). FGG-HTHP^{Q14C} appears to preorganize the direction of the attached FGG moieties towards the lateral side of the cylindrical structure of HTHP. Therefore, the FGG-HTHP^{Q14C} sheet could be further assembled to yield a macroscopic film without any solid support.

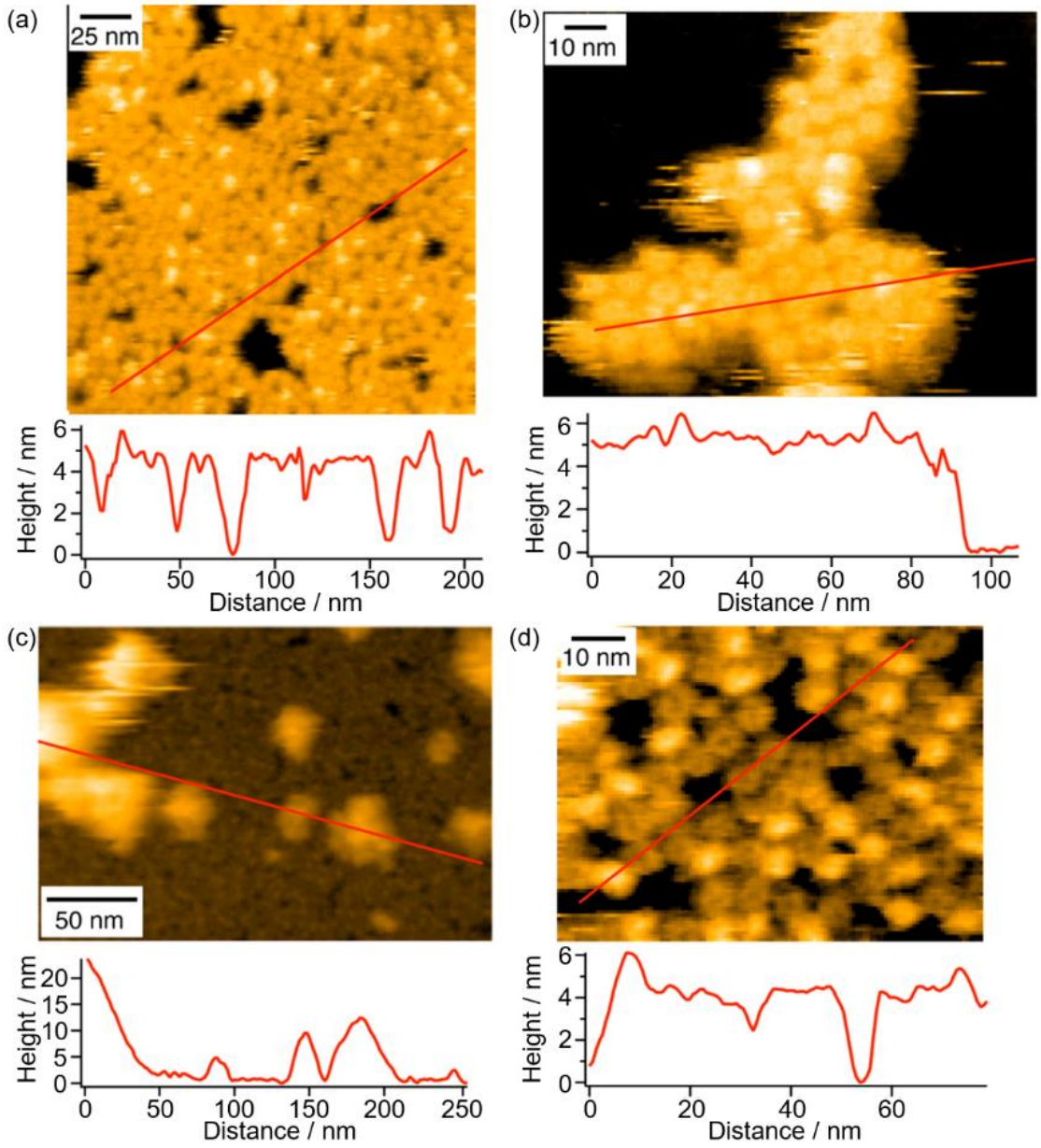

Figure 2-6. (a) Representative HS-AFM image of an assembly of FGG-HTHP^{Q14C} and CB8 on mica in a solution. The sample was prepared by mixing FGG-HTHP^{Q14C} (50 μM) and CB8 (25 μM) for 30 min in the solution with subsequent 30-fold dilution before casting on mica. (b) Representative HS-AFM image of an assembly of FGG-HTHP^{Q14C} and CB8 on mica in a solution. The sample is prepared by an additional 100-fold dilution of the 30-fold diluted solution used in (a). (c) Representative HS-AFM image of the assembly of FGG-HTHP^{E15C} and CB8 on mica in solution. The sample was prepared by mixing FGG-HTHP^{E15C} (50 μM) and CB8 (25 μM) for 5 min in the solution with subsequent 10-fold dilution before casting on mica. (d) Representative magnified HS-AFM image of (c) indicating a relatively flat segment. Each height profile is obtained along the red line in the corresponding image.

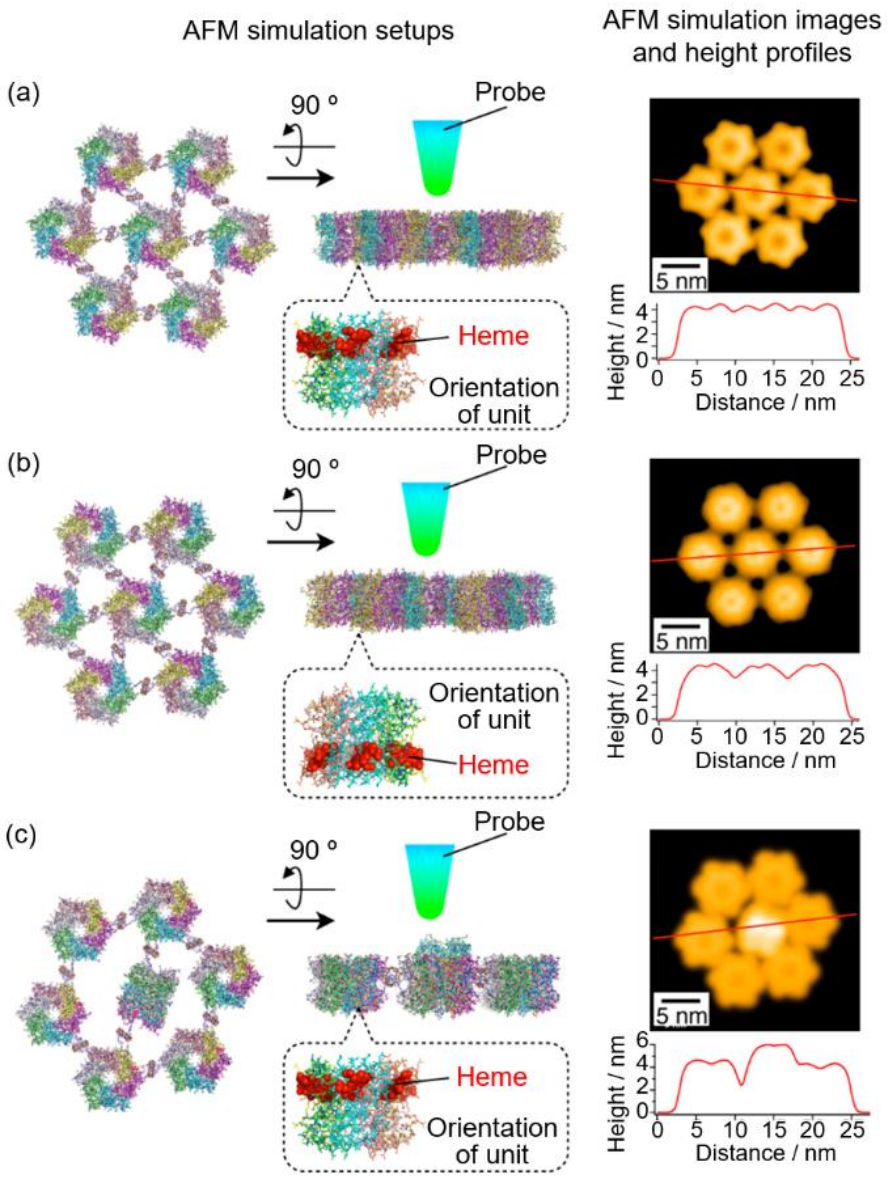

Figure 2-7. AFM simulation of assemblies of FGG-HTHP^{Q14C} and CB8, in which a heptameric model with same orientation is used. (a) The bottom of cylindrical protein structure close to the heme-binding sites is directed to probe. (b) The bottom near the heme-binding sites is directed to the substrate. (c) One HTHP unit at the center is vertically oriented.

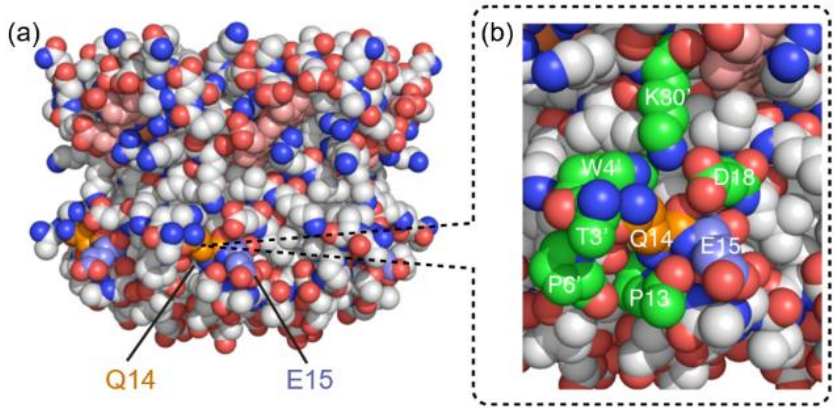

Figure 2-8. CPK-style crystal structure of HTHP (PDB ID: 2OYY). (a) Overall structure. (b) Closed up structure around Q14. Q14 and E15 residues are highlighted by orange and blue, respectively. Residues highlighted by green appears to restrict the motion of mFGG moiety and the attached C14 residue in FGG-HTHP^{Q14C}.

Dynamic formation process of the protein sheet

The process to form the FGG-HTHP^{Q14C} sheet on a mica substrate upon addition of CB8 was directly visualized by the HS-AFM (Figure 2-9). Firstly, only FGG-HTHP^{Q14C} (final concentration: 2.8 μM) was added to a solution on the mica substrate (Figure 2-9a). No clear image was seen even after 60 sec because the affinity of the protein against the mica substrate is too weak and the protein rapidly diffuses. Subsequent addition of CB8 (final concentration: 2.8 μM) at 19 sec induces the formation of small sheet-type assemblies after ca. 15 sec (Figure 2-9b). Further growth of the sheet occurs spontaneously and the FGG-HTHP^{Q14C} sheet covering the mica substrate was formed at ca.150 sec after the addition of CB8. Thus, the construction of a micrometer-sized sheet on the mica substrate is finished within several minutes even under high dilution conditions. In the case of FGG-HTHP^{E15C}, a small assembly and network-like structures are formed under similar conditions (Figure 2-9c,d). Further addition of FGG-HTHP^{E15C} causes formation of a sheet covering the mica substrate (Figure 2-9e), while several clusters which have heights of 7-8 nm are generated on the sheet due to undesirable growth in a vertical orientation on the mica substrate. Thus, HS-AFM measurements of the initial process to form the protein sheet on the mica substrate observed by indicates that the macroscopic shape of the protein assembly is derived from the nanoscale assembly behavior.

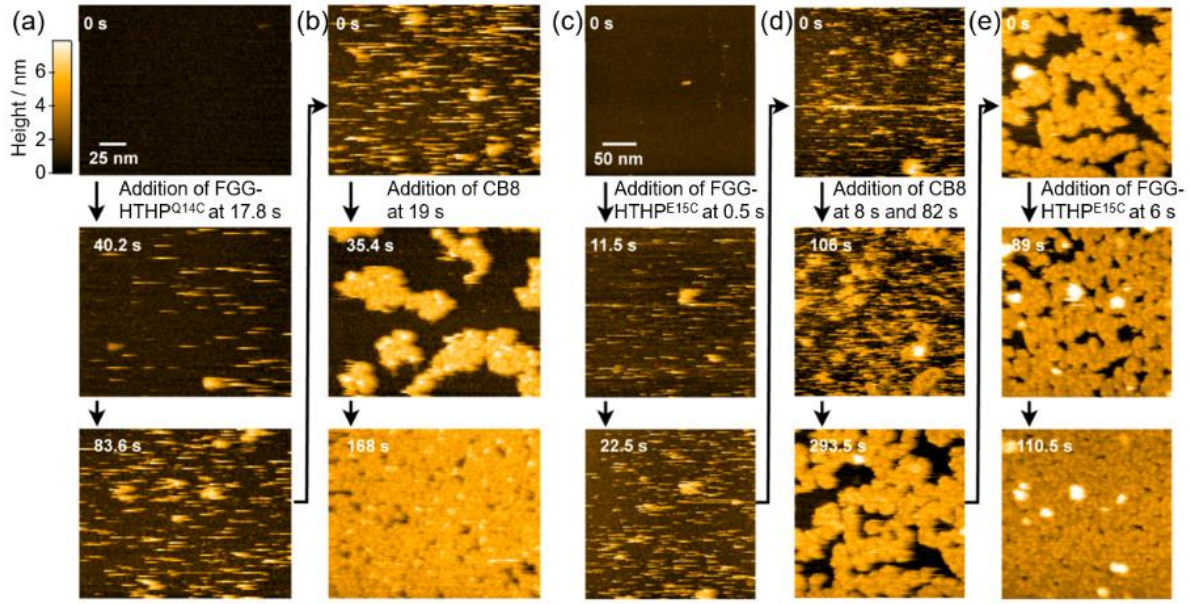

Figure 2-9. Initial process of formation of assemblies of FGG-HTHPs and CB8 on a mica substrate in a solution. (a) Snapshots from an HS-AFM movie of mica casted with only FGG-HTHP^{Q14C} (final conc.: 2.8 μM). (b) Snapshots from an HS-AFM movie of sample (a) upon addition of CB8 (final conc.: 2.8 μM). (c) Snapshots from an HS-AFM movie of mica casted with only FGG-HTHP^{E15C} (final conc.: 2.9 μM). (d) Snapshots from an HSAFM movie of sample (c) upon sequential addition of CB8 (final conc.: 2.9 μM). (e) Snapshots from an HS-AFM movie of sample (d) upon addition of FGG-HTHP^{E15C} (final conc.: 6.0 μM). Height information in all images is commonly shown by a color profile in (a).

2-3. Summary

In conclusion, the Q14C mutant of HTHP covalently modified with six FGG tripeptide tags is capable of forming a two-dimensional sheet-type assembly upon addition of CB8. The present work provides the following two significant insights with regard to protein assembling systems: (i) construction of protein sheets can be induced by a chemically-controlled host–guest interaction with moderate affinity and (ii) the dynamic formation process of formation of the protein sheet can be directly observed by HS-AFM. This HTHP sheet is expected to contribute to the development of materials with new mechanical properties and a new class of protein-based light-harvesting systems.

2-4. Experimental section

Material and methods

UV–vis spectral measurements were carried out with a UV-2700 double-beam spectrophotometer (Shimadzu), a V-670 UV–vis–NIR spectrophotometer (JASCO) or a BioSpec-nano spectrophotometer (Shimadzu). The pH values were monitored with a Horiba F-72 pH meter. MALDI-

TOF MS analysis were performed with a Bruker autoflex III mass spectrometer. Dynamic light scattering (DLS) measurements were performed using a Zetasizer μV (Malvern Instruments) with an 830 nm laser at 25 ºC. Optical microscopic images were obtained using Nikon SMZ1270i Oprtical Microscope equipped with Nikon Digital Camera DS-Fi3. Synthesis of maleimide-tethering FGG tripeptide (mFGG) was reported in the previous paper.[17] Ultrapure water (Milli-Q) was prepared using a Merck Millipore Integral 3 apparatus. Cucurbit[8]uril was purchased from Sigma-Aldrich. Other all reagents were of the highest guaranteed grade commercially available and were used as received unless otherwise indicated.

Protein Sequence of HTHP and its mutant

$HTHP^{WT}$:
SETWLPTLVTATPQEGFDLAVKLSRIAVKKTQPDAQVRDTLRAVYEKDANALIAVSAVVATHF
QTIAAANDYWKD.
$HTHP^{T3C}$:
SECWLPTLVTATPQEGFDLAVKLSRIAVKKTQPDAQVRDTLRAVYEKDANALIAVSAVVATHF
QTIAAANDYWKD.
$HTHP^{Q14C}$:
SETWLPTLVTATPCEGFDLAVKLSRIAVKKTQPDAQVRDTLRAVYEKDANALIAVSAVVATHF
QTIAAANDYWKD.
$HTHP^{E15C}$:
SETWLPTLVTATPQCGFDLAVKLSRIAVKKTQPDAQVRDTLRAVYEKDANALIAVSAVVATHF
QTIAAANDYWKD.
$HTHP^{T40C}$:
SETWLPTLVTATPQEGFDLAVKLSRIAVKKTQPDAQVRDCLRAVYEKDANALIAVSAVVATHF
QTIAAANDYWKD.
$HTHP^{V44C}$:
SETWLPTLVTATPQEGFDLAVKLSRIAVKKTQPDAQVRDTLRACYEKDANALIAVSAVVATHF
QTIAAANDYWKD.
$HTHP^{D71C}$:
SETWLPTLVTATPQEGFDLAVKLSRIAVKKTQPDAQVRDTLRAVYEKDANALIAVSAVVATHF
QTIAAANCYWKD.
$HTHP^{D75C}$:
SETWLPTLVTATPQEGFDLAVKLSRIAVKKTQPDAQVRDTLRAVYEKDANALIAVSAVVATHF
QTIAAANDYWKC.

Expression and purification of HTHP mutants

The gene expression system for wild type HTHP was reported in the previous paper.[23b] The single-point mutation was performed by the polymerase chain reaction (PCR) using the LA PCR in

vitro Mutagenesis Kit (Takara Bio Inc.) according to the protocol of the manufacture. The HTHP gene cloned into pDEST14 was used as a template to introduce each seven single-point mutation (T3C, Q14C, E15C, T40C, V44C, D71C or D75C) into the HTHP matrix. The primer sequence used to generate the mutant were:

T3C: (5'-GGAGATAGAACCATGAGCGAATGCTGGTTACCGACGTTGGTAAC-3') and the complementary primer;

Q14C: (5'-CGTTGGTAACCGCAACACCGTGCGAAGGCTTTGATCTGGCCGTG-3') and the complementary primer;

E15C: (5'-GGTAACCGCAACACCGCAGTGCGGCTTTGATCTGGCCGTGAAAC-3') and the complementary primer;

T40C: (5'-CAGATGCCCAAGTTCGCGATTGCCTCCGTGCTGTGTATGAGAAAG-3') and the complementary primer;

V44C: was (5'-GTTCGCGATACTCTCCGTGCTTGCTATGAGAAAGATGCGAATGCG-3') and the complementary primer;

D71C: (5'-GCATTTCCAGACCATCGCAGCTGCGAACTGCTACTGGAAAGAC-3') and the complementary primer;

D75C: (5'-GCTGCGAACGACTACTGGAAATGCTAATAGGACCCAGCTTTCTTG-3') and the complementary primer. After PCR, the template plasmids were digested with DpnI (Thermo Fisher Scientific). *E. Coli.* DH5α competent cells were transformed with PCR products. After the cultivation, the plasmids were purified with PureLink^{TM} Quick Plasmid Miniprep Kit (Thermo Fisher Scientific). DNA sequencing was performed to verify the correct mutation in the gene sequence. The resulting expression plasmid was used to transform *E. Coli.* BL21 (DE3). LB medium (3 L) containing ampicillin (300 mg) was inoculated with 50 mL of the culture (OD600 = 0.7) of the transformed cells. After the cells were grown aerobically with vigorous shaking at 37 ºC until OD600 reached 0.7, isopropyl-β-D-1-thiogalactopyranoside (IPTG, 1 mM as a final concentration) was added to the culture for induction of protein expression. The culture was continued overnight at 37 ºC. The cells were harvested by centrifugation at 3200 x g for 10 min. The harvested cells from 3 L of culture were re-suspended in ca. 50 mL of a 10 mM Tris-HCl buffer, pH 8.0, and lysed by freeze–thaw cycles with subsequent sonication for 30 sec x 10 times at 4 ºC. The lysate was then centrifuged and the supernatant was collected. The excess amount of hemin chloride (800 μM in 100 mM $NaOH_{aq}$) was added to the solution and stirred for 10 min at 4 ºC. The solution was incubated at 80 ºC for 10 min and the precipitate was removed by centrifugation at 8000 rpm for 10 min. The solution was loaded onto a DEAE Fast Flow (GE Healthcare) anion-exchange column pre-equilibrated with 10 mM potassium phosphate buffer at pH 6.0. The fraction of the target protein was collected by 10 mM potassium phosphate buffer at pH 6.0 containing 0.3 M NaCl. The obtained solution was concentrated using an Amicon stirred ultrafiltration cell with a 10 kDa molecular weight cut-off membrane (Millipore). The concentrated solution was passed through a Sephacryl S-200 column equilibrated with 100 mM potassium phosphate buffer at pH 7.0. The fractions with $R_z > 2.5$ (R_z is a ratio of absorbance values

at 402 nm and 280 nm) were collected and concentrated. The obtained Cys-introduced HTHP mutants were characterized by SDS-PAGE and MALDI-TOF MS, and stored at –80 ºC.

Preparation of FGG-HTHP

An aqueous solution of 1 M DTT (50 μL) was added to HTHP mutant (500 μM, 500 μL) and incubated for 1 h at 50 ºC. DTT was removed using a HiTrap Desalting column to provide a protein solution (2.0 mL). mFGG (1.3 mg, 10 eq) was dissolved in MilliQ (100 μL) and added into the protein solution and incubated at 25 ºC for 1 h. The excess mFGG was removed using a HiTrap Desalting column and FGG-HTHP (100 μM, 2.0 mL) was obtained. The modified protein was characterized by MALDI-TOF MS and UV–Vis spectrometry.

Dynamic light scattering (DLS) measurements

The assembling behavior of FGG-HTHP was observed from the DLS measurement. For DLS measurements, the used aqueous solution of FGG-HTHP (10, 20, 50 or 100 μM, dissolved in 100 mM potassium phosphate buffer at pH 7.0) was mixed with the same volume of CB_{aq} (from 0 to 50 μM) and incubated at 25 ºC for 1 h before the measurements. Prior to mixing solutions, the each solution was filtrated using a 0.22-μm filter. To analyze the protein solution, a 12 μL quartz cuvette was utilized. The cuvette was inserted into the apparatus for 2 min to obtain equilibration at the room temperature before the measurement was performed. The signals were processed in protein analysis mode. The data were obtained by the intensity-based particle size distribution mode. The DLS measurements of FGG-HTHP were conducted at 20 ºC. In these measurements. The time-dependent assembling behavior was also confirmed by DLS. The DLS measurements were repeated each 15 min after mixing. For observing the disassembly behavior only about FGG-HTHP^{Q14C} and FGG-HTHP^{E15C}, the DLS measurements were conducted after the addition of 10 mM memantine $hydrochloride_{aq}$ (final concentration is 50 μM). The sample solution was incubated at room temperature for 15 min after the addition of memantine hydrochloride and mixing by pipetting.

Modeling of the HTHP heptamer

The modeling was performed using YASARA[27] Structure Version 13.6.16 that employed force field AMBER03[28] for protein residues and GAFF[29] using AM1/BCC[30] partial charges for the mFGG moiety covalently bound to Cys14. The calculation was carried out using YASARA Structure Version 13.6.16 employing force field AMBER03. To maintain the correct coordination geometry, the distances from the metal to all four pyrrole N atoms of the porphyrin ligand were constrained to 2.0 Å. The penta-coordination by ligation with Tyr45 was represented by two force field arrows and the distances of the Fe–O dative bond was constrained to 2.6 Å, according to the crystal structure (PDB ID: 2OYY) of HTHP. The partial charge of the metal was set to +2 and the total charge of the heme was set to zero. Geometry for complex of CB8 and FGG was modeled by reported crystal structure.[21]

CB8 and mFGG molecules unused for assembly were omitted. Manually constructed heptamers were solvated in a box of TIP3P water molecules using periodic boundaries at pH 7.0 and a density of 0.997 g/mL. The minimized structures were obtained by steepest descent minimization and simulated annealing at 298 K.

HS-AFM imaging

HS-AFM imaging was carried out using a laboratory-designed HS-AFM apparatus operated in tapping mode.[31] The dimensions of the cantilever (Olympus) were 6−7 μm length, 2 μm width, and 90 nm thickness (AC7, Olympus). The nominal spring constant was ca. 0.2 N/m, the resonant frequency was 0.7−1 MHz, and the quality factor in an aqueous solution was ca. 2. For HS-AFM imaging, the free oscillation amplitude was set to 1−2 nm, and the set-point amplitude was approximately 90% of the free oscillation amplitude. An amorphous carbon tip grown by electron-beam deposition with scanning electron microscopy was used.[32] After the electron-beam deposition, the tip was sharpened by plasma etching under Ar gas (the final tip apex, d = ca. 4 nm).

For the HS-AFM imaging, mica was used as a substrate. To measure the samples in Figure 2-6, the solution of sample was deposited onto the freshly cleaved mica substrate. After the 5-min incubation, the substrate was thoroughly washed with 50 mM potassium phosphate buffer, pH 7.0, to remove excess molecules. To measure the samples in Figure 2-9, 50 mM potassium phosphate buffer, pH 7.0, (3 μL) was first casted onto the mica substrate and the stock solution of protein or CB8 was added during the imaging. The HS-AFM imaging was performed in the buffer at room temperature.

AFM simulation.

Simulation of AFM images was performed using custom software based on IgorPro 8 (Version 8.03, Wavemetrics, Lake Oswego, Ore., USA) software. The pseudo AFM image was generated using a cone-shaped AFM tip with a radius of 1 nm and half cone angle of 10°, and the energy minimized structure of the HTHP heptamer. After construction of the simulated image, the image was filtered by a low-pass filter with a cut off spatial frequency of 2 nm because the spatial resolution of the HS-AFM is generally limited to 2 nm.

References and notes

1. Ryadnov, M. G.; Woolfson, D. N.; In Nanobiotechnology II; ed. by Mirkin, C. A.; Niemeyer, C. M. Wiley-VCH, Weiheim, 2007, 24 Chap. 2, pp 17-38.
2. (a) Luo, Q.; Hou, C.; Bai, Y.; Wang, R.; Liu, J. *Chem. Rev.* **2016**, *116*, 13571-13632. (b) Oohora, K.; Hayashi, T. *Curr. Opin. Chem. Biol.* **2014**, *19*, 154-161. (c) Hirota, S. *J. Inorg. Biochem.* **2019**, *194*, 170-179. (d) Kobayashi, N.; Arai, R. *Curr. Opin. Biotech.* **2017**, *46*, 57-65. (e) Malay, A. D.; Miyazaki, N.; Biela, A.; Chakraborti, S.; Majsterkiewicz, K.; Stupka, I.; Kaplan, C. S.; Kowalczyk, A.; Piette, B. M. A. G.; Hochberg, G. K. A.; Wu, D.; Wrobel, T. P.; Fineberg, A.; Kushwah, M. S.;

Kelemen, M.; Vavpetič, P.; Pelicon, P.; Kukura, P.; Benesch, J. L. P.; Iwasaki, K.; Heddle, J. G. *Nature* **2019**, *569* 438-442. (f) Peschke, T.; Bitterwolf, P.; Gallus, S.; Hu, Y.; Oelschlaeger, C.; Willenbacher, N.; Rabe K. S.; Niemeyer, C. M. *Angew. Chem. Int. Ed.* **2018**, *57*, 17028-17032.

3. Oohora, K.; Fujimaki, N.; Kajihara, R.; Watanabe, H.; Uchihashi, T.; Hayashi, T.; *J. Am. Chem. Soc.* **2018**, *140*, 10145-10148.
4. (a) Brodin, J. D.; Smith, S. J.; Carr, J. R.; Tezcan, F. A. *J. Am. Chem. Soc.* **2015**, *137*, 10468-10471. (b) Biswas, S.; Kinbara, K.; Niwa, T.; Taguchi, H.; Ishii, N.; Watanabe, S.; Miyata, K.; Kataoka, K.; Aida, T. *Nat. Chem.* **2013**, *5*, 613-620. (c) Nguyen, T. K.; Negishi, H.; Abe, S.; Ueno, T. *Chem. Sci.* **2019**, *10*, 1046-1051. (d) Komatsu, T.; Qu, X.; Ihara, H.; Fujihara, M.; Azuma, H.; Ikeda, H. *J. Am. Chem. Soc.* **2011**, *133*, 3246-3248.
5. Oohora, K.; Kajihara, R.; Fujimaki, N.; Uchihashi, T.; Hayashi, T.; Fujimaki, N.; Uchihashi, T.; Hayashi, T. *Chem. Commun.* **2019**, *55*, 1544-1547.
6. (a) Bastings, M. M. C.; de Greef, T. F. A.; van Dongen, J. L. J.; Merkx, M.; Meijer, E. W. *Chem. Sci.* **2010**, *1*, 79-88. (b) Li, Q.; So, C. R.; Fegan, A.; Cody, V.; Sarikaya, M.; Vallera, D. A.; Wagner, C. R. *J. Am. Chem. Soc.* **2010**, *132*, 17247-17257.
7. Suzuki, Y.; Cardone, G.; Restrepo, D.; Zavattieri, P. D.; Baker, T. S.; Tezcan, F. A. *Nature* **2016**, *533*, 369-373.
8. (a) Li, X.; Qiao, S.; Zhao, L.; Liu, S.; Li, F.; Yang, F.; Luo, Q.; Hou, C.; Xu, J.; Liu, J. *ACS Nano* **2019**, *13*, 1861-1869. (b) Zhao, L.; Zou, H.; Zhang, H.; Sun, H.; Wang, T.; Pan, T.; Li, X.; Bai, Y.; Qiao, S.; Luo, Q.; Xu, J.; Hou, C.; Liu, J. *ACS Nano* **2017**, *11*, 938-945.
9. Zhao, L.; Li, Y.; Wang, T.; Qiao, S.; Li, X.; Wang, R.; Luo, Q.; Hou, C.; Xu, J.; Liu, J.; *J. Mater. Chem. B* **2018**, *6*, 75-83.
10. (a) Gonen, S.; DiMaio, F.; Gonen, T.; Baker, D. *Science* **2015**, *348*, 1365. (b) Sinclair, J. C.; Davies, K. M.; Venien-Bryan, C.; Noble, M. E. M. *Nat. Nanotechnol.* **2011**, *6*, 558-562.
11. Gao, X.; Yang, S.; Zhao, C.; Ren, Y.; Wei, D. *Angew. Chem. Int. Ed.* **2014**, *53*, 14027-10430.
12. Brodin, J. D.; Ambroggio, X. I.; Tang, C.; Parent, K. N.; Baker, T. S.; Tezcan, F. A. *Nat. Chem.* **2012**, *4*, 375-382.
13. Yang, G.; Ding, H.; Kochovski, Z.; Hu, R.; Lu, Y.; Ma, Y.; Chen, G.; Jiang, M. *Angew. Chem. Int. Ed.* **2017**, *56*, 10691-10695.
14. Ringler, P.; Schulz, G. E. *Science* **2003**, *302*, 106-109.
15. Bailey, J. B.; Zhang, L.; Chiong, J. A.; Ahn, S.; Tezcan, F. A.; *J. Am. Chem. Soc.* **2017**, *139*, 8160-8166.
16. Lai, Y. T.; Cascio, D.; Yeates, T. O. *Science* **2012**, *336*, 1129.
17. Li, X.; Bai, Y.; Huang, Z.; Si, C.; Dong, Z.; Luo, Q.; Liu, J. *Nanoscale* **2017**, *9*, 7991-7997.
18. (a) Hou, C.; Li, J.; Zhao, L.; Zhang, W.; Luo, Q.; Dong, Z.; Xu, J.; Liu, J. *Angew. Chem. Int. Ed.* **2013**, *52*, 5590-5593. (b) Wang, R.; Qiao, S.; Zhao, L.; Hou, C.; Li, X.; Liu, Y.; Luo, Q.; Xu, J.; Li, H.; Liu, J. *Chem. Commun.* **2017**, *53*, 10532-10535.
19. (a) Nguyen, H. D.; Dang, D. T.; van Dongen, J. L. J.; Brunsveld, L. *Angew. Chem. Int. Ed.* **2010**,

49, 895-898. (b) Dang, D. T.; Schill, J.; Brunsveld, L. *Chem. Sci.* **2012**, *3*, 2679-2684.

20. (a) Oohora, K.; Burazerovic, S.; Onoda, A.; Wilson, Y. M.; Ward, T. R.; Hayashi, T. *Angew. Chem. Int. Ed.* **2012**, *51*, 3818-3821. (b) Kitagishi, H.; Oohora, K.; Yamaguchi, H.; Sato, H. Matsuo, T.; Harada, A.; Hayashi, T. *J. Am. Chem. Soc.* **2007**, *129*, 10326-10327. (c) Kitagishi, H.; Kakikura, Y.; Yamaguchi, H.; Oohora, K.; Harada, A.; Hayashi, T. *Angew. Chem. Int. Ed.* **2009**, *48*, 1271-1274. (d) Oohora, K.; Onoda, A.; Kitagishi, H.; Yamaguchi, H.; Harada, A.; Hayashi, T. *Chem. Sci.* **2011**, *2*, 1033-1038. (e) Oohora, K.; Onuma, Y.; Tanaka, Y.; Onoda, A.; Hayashi, T. *Chem. Commun.* **2017**, *53*, 6879-6882.
21. Heitmann, L. M.; Taylor, A. B.; Hart, P. J.; Urbach, A. R. *J. Am. Chem. Soc.* **2006**, *128*, 12574-12581.
22. Jeoung, J.-H.; Pippig, D. A.; Martins, B. M.; Wagener, N.; Dobbek, H. *J. Mol. Biol.* **2007**, *368*, 1122-1131.
23. (a) Oohora, K.; Hirayama, S.; Mashima, T.; Hayashi, T.; *J. Porphyrins Phthalocyanines*, *in press*. (b) Oohora, K.; Mashima, T.; Ohkubo, K.; Fukuzumi, S.; Hayashi, T. *Chem. Commun.* **2015**, *51*, 11138-11140. (c) Mashima, T.; Oohora, K.; Hayashi, T. *Phys. Chem. Chem. Phys.* **2018**, *20*, 3200-3209.
24. Low ionic strength causes the nonspecific aggregation in several FGG-HTHP mutants (T3C, T40C, D71C and D75C) in the absence of CB8, whereas high ionic strength induces precipitation of CB8
25. L iu, S.; Ruspic, C.; Mukhopadhyay, P.; Chakrabarti, S.; Zavalij, P. Y.; Isaacs, L. *J. Am. Chem. Soc.* **2005**, *127*, 15959-15967.
26. The ternary affinity between two NH_2-FGG-COOH molecules and one CB8 molecule is determined to be 1.5 x 10^{11} M^{-2} according to previous results [21].
27. Krieger, E.; Darden, T.; Nabuurs, S. B.; Finkelstein, A.; Vriend, G. *Proteins* **2004**, *57*, 678-683.
28. Duan, Y.; Wu, C.; Chowdhury, S.; Lee, M. C.; Xiong, G.; Zhang, W.; Yang, R.; Cieplak, P.; Luo, R.; Lee, T.; Caldwell, J.; Wang, J.; Kollman, P. *J. Comput. Chem.* **2003**, *24*, 1999-2012.
29. Wang, J.; Wolf, R. M.; Caldwell, J. W.; Kollman, P. A.; Case, D. A. *J. Comput. Chem* **2004**, *25*, 1157-1174.
30. Jakalian, A.; Jack, D. B.; Bayly, C. I. *J. Comput. Chem.* **2002**, *23*, 1623-1641.
31. (a) Ando, T.; Kodera, N.; Takai, E.; Maruyama, D.; Saito, K.; Toda, A. *Proc. Natl Acad. Sci. USA* **2001**, *98*, 12468-12472. (b) Ando, T.; Uchihashi, T.; Fukuma, T. *Prog. Surf. Sci.* **2008**, *83*, 337-437.
32. Wendel, M.; Lorenz, H.; Kottthaus, J. P. *Appl. Phys. Lett.* **1995**, *67*, 3732-3734.

Chapter 3
Thermoresponsive Micelle Construction of HTHP Modified with Poly(*N*-isopropylacrylamide) Designing toward an Artificial Light-harvesting System

3-1. Introduction

Supramolecular assemblies of proteins in nature perform and control their functions with biochemically sophisticated structures. Over the last two decades, many researchers have focused on replicating such structures and have produced several bio-inspired artificial protein assemblies.[1-6] Four main strategies have been utilized to create artificial protein assemblies. The first strategy takes advantage of protein–protein interactions observed in natural systems. Self-assembly of computationally designed protein,[7,8] genetically fused protein,[9-11] and supercharged proteins[12,13] have often been used. The second strategy employs interactions between proteins and other molecules such as aptamers,[14] dendrimers,[15] quantum dots[16]. Moreover, the interaction of protein with small molecules such as cofactors,[17–20] inhibitors,[21] ligands[22] and uncanonical host–guest interaction[23] is often used. Introduction of a metal coordination site onto the protein surface is also utilized in this strategy, typically with an engineered interface between the protein matrices and zinc[24] or gold ion[25] to produce protein assemblies. The third strategy includes formation of covalent bonds such as an isopeptide bond,[26] or a disulfide bond.[27,28] This approach has been extended beyond the field of supramolecular chemistry. The fourth strategy employs a self-assembling molecules such as DNA,[29,30] designed peptide[31] or synthetic polymers which are introduced into a protein. For instance, the hydrophobic polystyrene[32] and its copolymer[33] can be attached onto a protein to provide hydrophobicity which induces the formation of an assembly of the modified protein.

The fourth strategy has gained significant interest in an effort to construct new protein assemblies because there are many variations of natural and synthetic polymers available to drive formation of protein assemblies with different characteristics. For example, thermoresponsive polymers may be employd as modifiers. Poly(*N*-isoporpylacrylamide) (PNIPAAm) is often used to modify the protein surface. It is a representative thermoresponsive polymer which shows lower critical solution temperature (LCST) behavior.[34] The aqueous solubility of PNIPAAm dramatically decreases at temperatures higher than LCST (ca. 32 ºC) and becomes water insoluble at higher temperatures. This LCST behavior of PNIPAAm provides a significant advantage to construct protein assemblies because the hydrophobicity of PNIPAAm attached onto a protein surface can provide a driving force to generate a protein assembly at high temperatures. Over the past decade, there have been several reports describing the introduction of thermoresponsive PNIPAAm onto protein surfaces.[35-37] However, there are few examples of specific applications of stimuli-responsive protein assemblies at the present time.

In the previous work, the author's group has prepared various hemoprotein assemblies via the

heme cofactor–heme pocket interaction utilizing the second main strategy outlined above. These efforts provided linear structures with photochemical properties within the assemblies.[38-40] In separate investigations, the author recently focused on designing a thermoresponsive hemoprotein assembly assisted by PNIPAAm which is attached onto the surface of a thermostable protein, because surface modification of a thermostable protein with a thermoresponsive polymer is expected to yield a stable artificial protein assembly formed in response to thermal stimuli. As a building block of an artificial protein assembly, hexameric tyrosine-coordinated heme protein (HTHP)[41] was selected. HTHP has a ring-shaped homohexameric structure with six annularly aligned heme molecules. One of the characteristic properties of HTHP is its thermal stability with a denaturation point, T_m, of ca. 130 ºC. This suggests that HTHP would be ideal for use as a building block for a thermoresponsive protein assembly. Therefore, the author prepared HTHP modified with PNIPAAm, which provides a block copolymer consisting of the thermostable protein and thermoresponsive polymer (Figure 3-1). This conjugate has a micellar-type spherical structure of PNIPAAm-modified HTHP (PNIPAAm-HTHP) formed via interactions among attached PNIPAAm molecules. The micellar structure of the assembly of PNIPAAm-HTHP is quite similar to a natural photosynthetic system of purple bacteria (*Rhodobacter sphaeroides*), where the complex ring-shaped light-harvesting proteins[42] enable migration of energy excited by sunlight among the photosensitizers. This finding encouraged the author to generate an artificial light-harvesting system by replacing the heme cofactor in the assembly of PNIPAAm-HTHP with zinc porphyrin to replicate the natural light-harvesting system. In this work, the author reports the preparation and evaluation of a thermoresponsive micellar-type assembly based on this hemoprotein and describe its unique photochemical properties.

3-2. Results and discussion

Modification of HTHP with maleimide-terminated PNIPAAm

For the site-selective surface modification of HTHP by PNIPAAm, the author chose the V44 residue as a reaction point, which is located at the bottom of the columnar structure and exposed on the outer surface of HTHP. Because wild-type HTHP ($HTHP^{WT}$) contains no cysteine residue, an introduced cysteine residue becomes a single reaction site in each monomer unit. The mutant $HTHP^{V44C}$ was prepared according to the previous report[43] and then treated with dithiothreitol (DTT) to cleave the disulfide bonds between the introduced Cys-residues in advance of the modification. After confirmation of the disulfide bond cleavage detected by analytical size exclusion chromatography (SEC), $HTHP^{V44C}$ was treated with maleimide-terminated PNIPAAm (PNIPAAm-MI, M_n = 5,500) and the modified protein was purified with an anion-exchange column. The modification was then identified by SDS-PAGE and analytical SEC measurements (Figure 3-2). SDS-PAGE shows

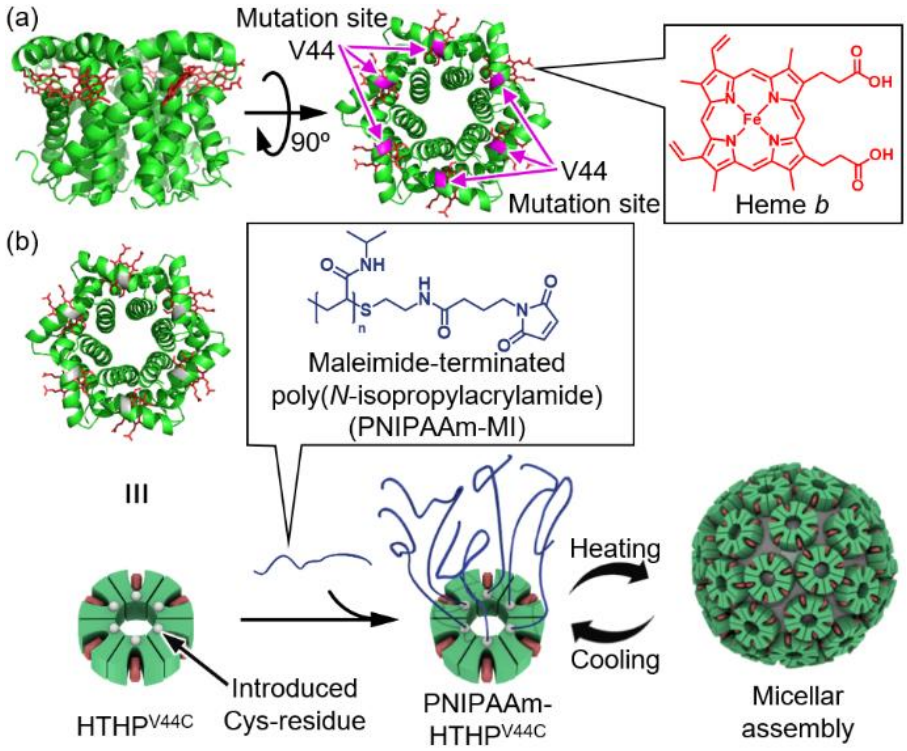

Figure 3-1. (a) Reported HTHP structure (PDB ID: 2OYY). Red molecules in the protein represent heme *b*. Pink arrows indicate the mutation site. (b) Schematic representation of attachment of the maleimide-terminated PNIPAAm molecule onto the surface modification of HTHP to construct a thermoresponsive micellar assembly of HTHP. Structure of maleimide-terminated PNIPAAm is shown in the inset.

a single band of monomeric HTHP^{V44C} before the modification reaction. After modification with PNIPAAm-MI, the major band is shifted to a larger molecular weight area with broad distribution, although a small amount of the unmodified monomer band remains. Analysis of this gel image suggests that the conversion of the modification based on the monomer is about 85% after optimization of the reaction conditions. The incomplete modification could be caused by steric hindrance between the attached PNIPAAm molecules. The profile of the analytical SEC measurement does not indicate the presence of unmodified hexamer after the reaction. The broad elution profile of the modified protein is derived from the molecular weight distribution of the modified polymer and/or the interaction between the polymer and the column resin. Thus, the author confirmed the formation of PNIPAAm-HTHP^{V44C}, which is prepared by modification of HTHP^{V44C} with PNIPAAm-MI.

Thermoresponsive assembly of PNIPAAm-HTHP^{V44C}

The thermoresponsive assembling behavior of PNIPAAm-HTHP^{V44C} was evaluated by dynamic light scattering (DLS) measurements (Table 3-1, Figure 3-3a). The protein has a small diameter of about 14 nm at 20 ºC. This diameter is greater than the diameter of HTHP^{V44C} due to the PNIPAAm molecules attached on the surface. The heating procedure leads to the formation of a

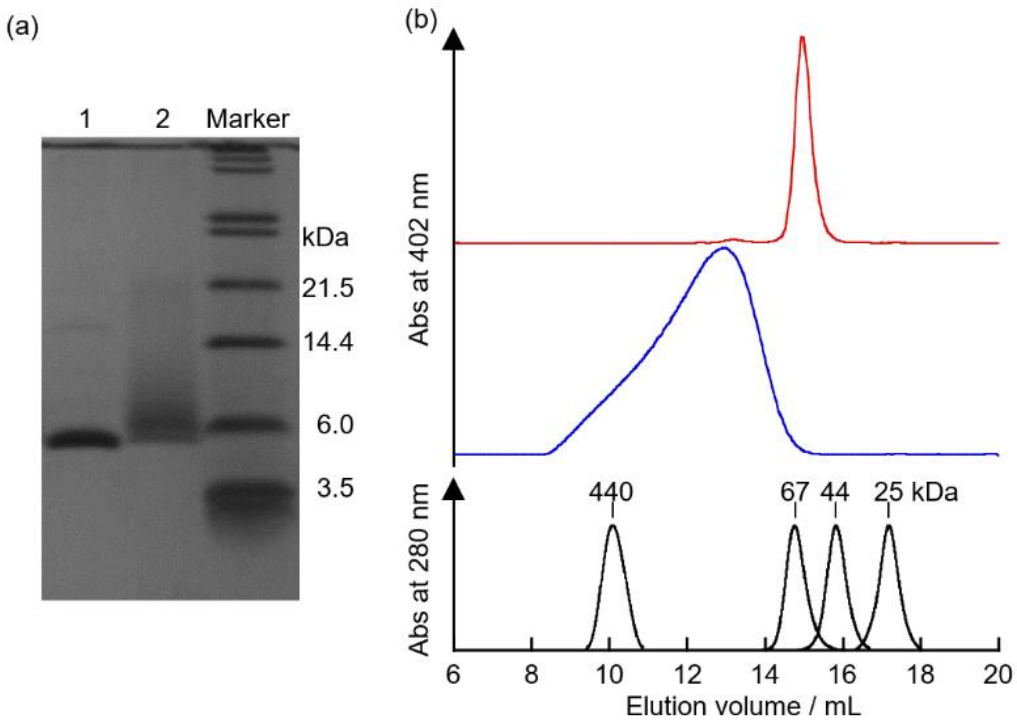

Figure 3-2. (a) SDS-PAGE of unmodified HTHP^{V44C} (lane 1) and PNIPAAm-HTHP^{V44C} (lane 2). (b) SEC traces of HTHP^{V44C} (red), PNIPAAm-HTHP^{V44C} (blue) and authentic samples (black).

micellar assembly with a larger diameter via the interaction among the attached PNIPAAm moieties. The diameter of the micellar assembly is about 55 nm at 30 ºC, and further heating at higher temperatures results in shrinkage of the assembly. These findings indicate that a slightly larger and looser micellar assembly is formed at temperatures close to the typical LCST of PNIPAAm because the interactions between individual polymer units are relatively weak. Shrinkage occurs as a result of enhancement of these interactions at temperatures higher than the LCST. Finally, the diameter of the micellar assembly was found to be 43 nm at 60 ºC. This behavior is also observed in the block copolymer of a hydrophilic polymer, poly(*N*-vinyl-2-pyrrolidone), and PNIPAAm.[44] Thus, these DLS results indicate formation of a spherical micellar assembly with a hydrophilic outer shell and a hydrophobic core formed by thermoresponsive shrinkage of the PNIPAAm molecules. The size of the constructed micellar assembly (ca. 40-nm diameter) is roughly estimated to include 100 hexamer units (6-nm diameter and 4-nm height). In addition to the assembly, the disassembly behavior was seen upon cooling. It was revealed that cooling of the assembly reduces its size by ca. 30 nm, according to DLS measurements. This result indicates recovery of the original hexameric structure of the PNIPAAm-HTHP^{V44C}. The author found that a cycle of assembly and disassembly could be repeated at least five times as shown in Figure 3-3b. Moreover, the shrinkage which occurs at temperatures higher than 30 ºC is also repetitive.

The dependence of the size of the micellar assembly on protein concentration was investigated by DLS measurements at 60 ºC (Figure 3-4). The size of the micellar assembly was found to be essentially independent of protein concentration in the range from 10 μM to 500 μM. This typical

Table 3-1. Hydrodynamic diameter of the obtained protein assembly at various temperatures[a]

Temperature / ºC	Diameter / nm[b]
20	14
30	55
40	46
50	45
60	43

[a] Conditions: [protein] = 50 μM (in terms of the monomer) in buffer, pH = 7.0. [b] The hydrodynamic diameters were determined from DLS measurements.

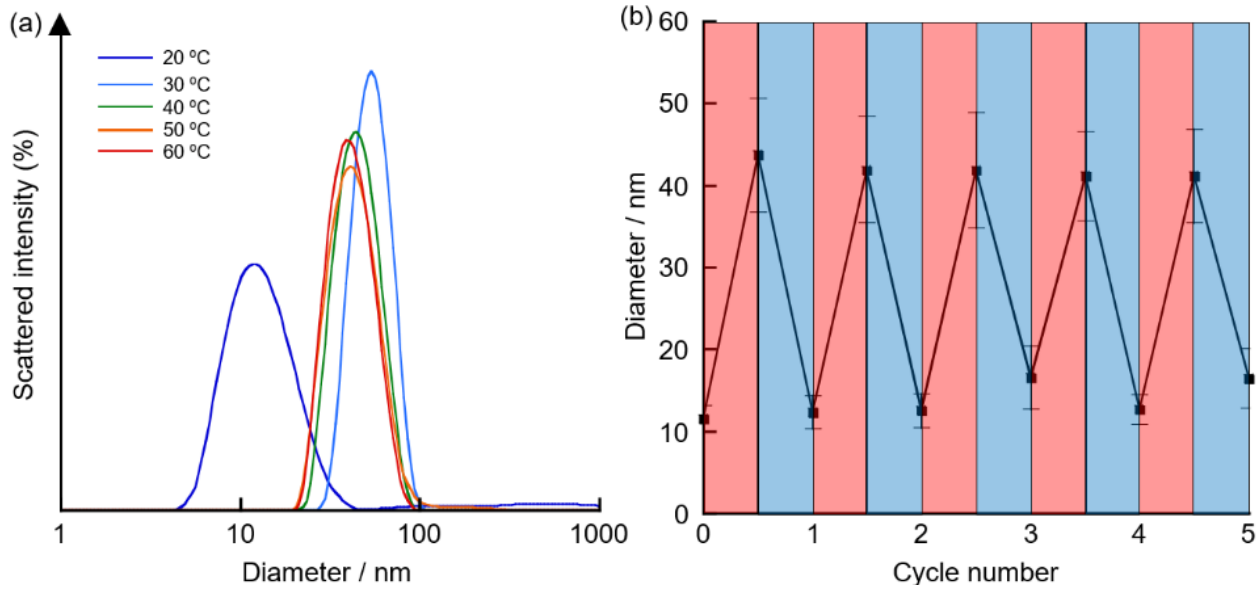

Figure 3-3. (a) Size distributions obtained from DLS analysis for a solution of 50 μM PNIPAAm-HTHP^{V44C} in buffer at various temperatures. (b) Diameter of the micellar assembly of PNIPAAm-HTHP^{V44C} determined by DLS upon cycling between heating at 60 ºC (red) and cooling at 20 ºC (blue).

concentration-independent assembly behavior is also observed in other protein assemblies with uniform structure, such as engineered spherical viral capsid proteins,[45] modified ferritin[46] and protein-based micelles.[47] As a control, an aqueous solution of PNIPAAm-MI without protein modification was evaluated, and it was found that its diameter significantly depends on its concentration, in which the size of aggregates increases as the concentration increases (Figure 3-4 inset). These results indicate that the shape of the obtained micellar assembly of PNIPAAm-HTHP^{V44C} is uniform because nonspecific aggregations are absent in the solution.

Stability of the heme and protein structures in the micellar assembly

The thermal stability of the HTHP structure in the micellar assembly was investigated (Figure 3-5). First, UV–vis spectroscopy was used because its spectral features are known to indicate the

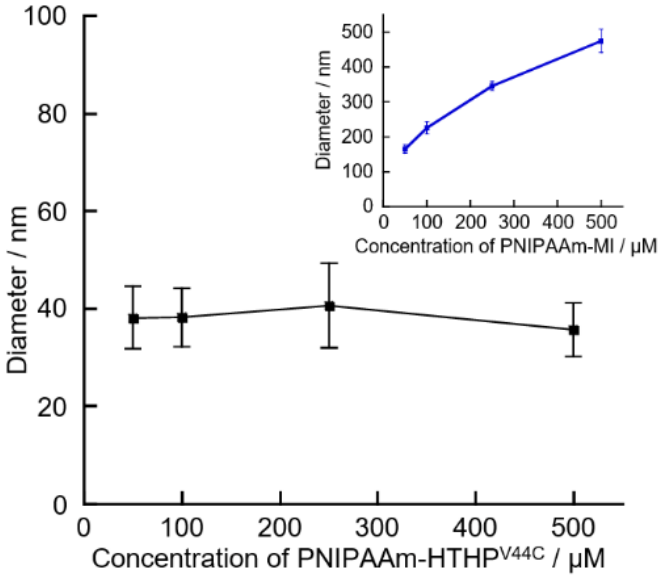

Figure 3-4. Relationship between the size of the micellar assembly and the concentration of PNIPAAm-HTHP^{V44C} or PNIPAAm-MI (inset) at 60 ºC.

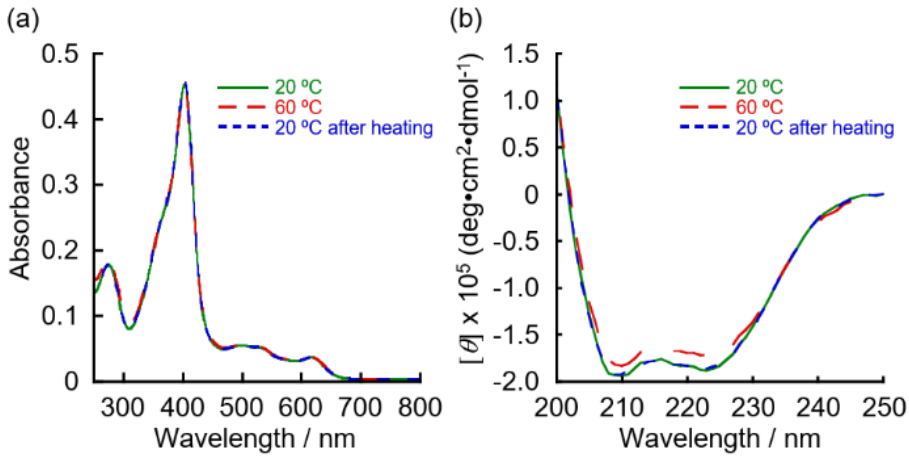

Figure 3-5. (a) UV–vis and (b) CD spectra of PNIPAAm-HTHP^{V44C} at 20 ºC, 60 ºC and 20 ºC after cooling.

coordination state of the heme molecule. The shapes and the intensities of the Soret band and Q-band derived from the heme are essentially identical at 20 ºC and 60 ºC and at 20 ºC after cooling (Figure 3-5a). This result provides evidence that the coordination structure of heme in HTHP does not change during the heating process. Furthermore, the secondary structure of the protein matrix was evaluated by CD spectroscopy. As shown in Figure 3-5b, the shape and intensity of the spectrum derived from the α-helical structure of HTHP at 60 °C is consistent with the spectrum observed at 20 °C. These results reveal that the structures of the protein units in the micellar assembly are maintained even at 60 ºC.

Atomic force microscopic measurements of the micellar assembly with cross-linked protein matrices

Direct observation of the structure was attempted by atomic force microscopy (AFM). Since AFM measurements in a solution at high temperature are technically challenging, the protein matrices in the obtained assembly of PNIPAAm-HTHP^{V44C} were cross-linked to facilitate direct observation of the micellar assembly structure (Figure 3-6). Glutaraldehyde, which is often used to cross-link protein matrices within a crystal, was employed as a cross-linker. Reaction of the PNIPAAm-HTHP^{V44C} assembly with glutaraldehyde was performed at 60 ºC to retain the protein assembly state even at

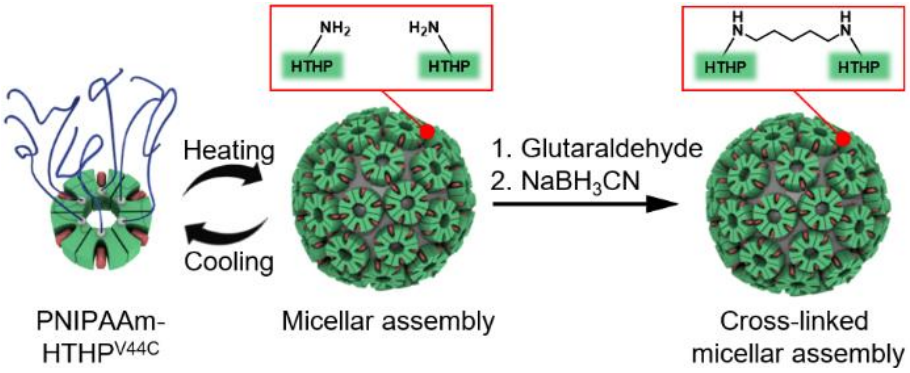

Figure 3-6. Schematic representation of the cross-linking reaction of the micellar assembly of PNIPAAm-HTHP^{V44C}.

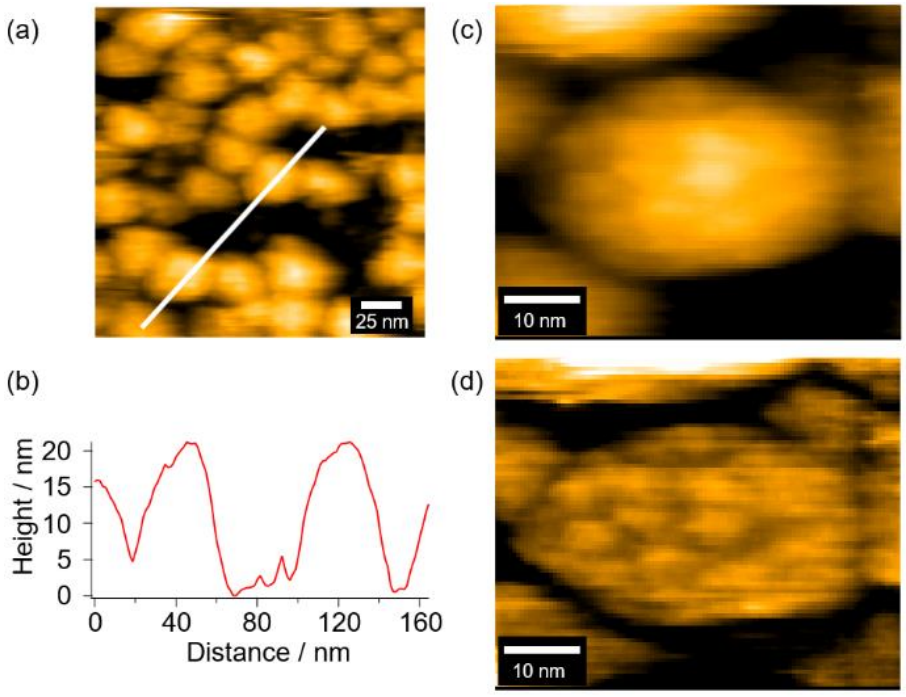

Figure 3-7. (a) Representative AFM image of the cross-linked PNIPAAm-HTP^{V44C} assembly. (b) Height profile along the white line in (a). (c) Magnified AFM image of the cross-linked PNIPAAm-HTHP^{V44C} assembly. (d) Image of (c) processed by a band-pass filter within cutoff wavelengths of 2.2 nm and 19.5 nm.

ambient temperature. After the treatment with $NaBH_3CN$ at 4 °C, the cross-linked protein assembly was purified by preparative SEC. The size of the purified assembly was evaluated by DLS. When this cross-linked protein is incubated under low-temperature conditions (at 20 ºC), the average diameter is 25 nm. The protein matrices were successfully fixed in the state to form the assembly at low temperature, although the size of the cross-linked protein assembly at ambient temperature is smaller than the size determined by DLS before cross-linking at 60 ºC.

Next, the cross-linked assembly on the mica substrate treated with glutaraldehyde and (3-aminopropyl)triethoxysilane was directly observed by high-speed AFM (HS-AFM) at room temperature to evaluate its surface structure (Figure 3-7). Spherical objects with ca. 20 nm diameter were observed in the solution (Figures 3-7a,b). This size is consistent with the diameter determined by DLS measurements. Moreover, the magnified spherical object (Figure 3-7c) was analyzed using a band-pass filter to obtain clearer images as shown in Figure 3-7d. Several nanometer-sized domains were clearly observed as spherical objects, indicating that the HTHP units are located on the surface. These HS-AFM images of the cross-linked PNIPAAm-HTHP^{V44C} assembly unambiguously indicate that PNIPAAm-HTHP^{V44C} forms the expected micellar structure at high temperature as shown in

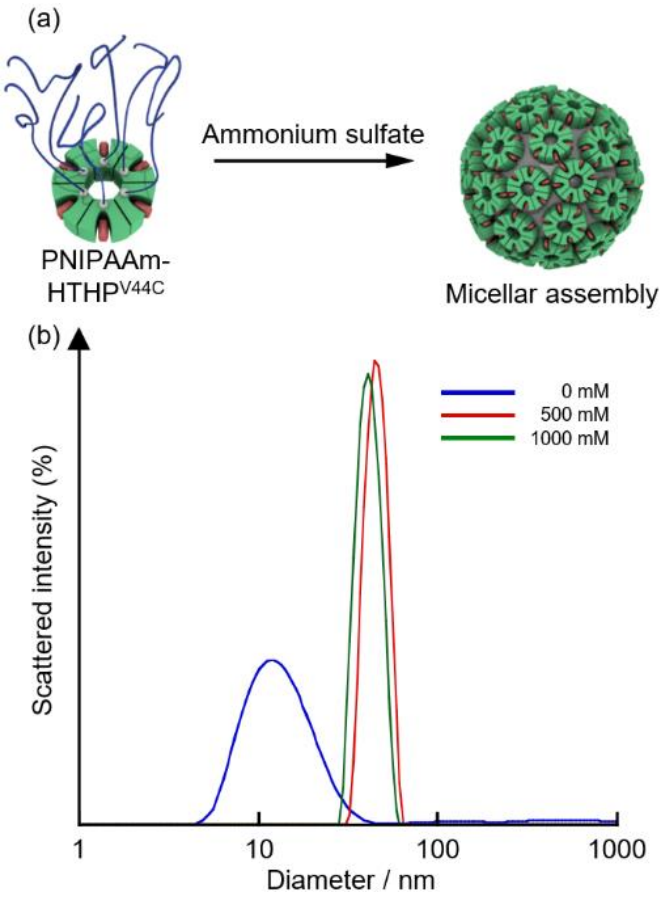

Figure 3-8. (a) Schematic representation of the preparation of PNIPAAm-HTHP^{V44C} upon addition of ammonium sulfate. (b) Size distributions obtained from DLS analysis for a solution of 50 μM PNIPAAm-HTHP^{V44C} in 100 mM potassium phosphate buffer (pH = 7.0) at various concentrations of ammonium sulfate (0, 500 or 1000 mM).

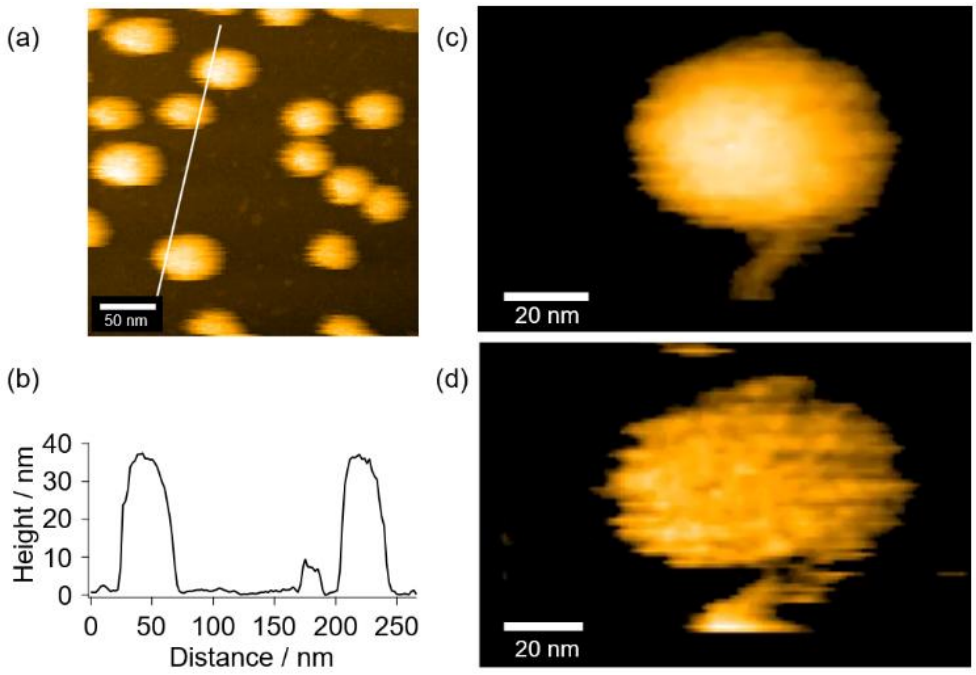

Figure 3-9. (a) Representative AFM-image of the PNIPAAm-HTP^{V44C} assembly constructed upon addition of ammonium sulfate (500 mM). (b) The height profile along the white line in (a). (c) Magnified AFM image of the cross-linked PNIPAAm-HTHP^{V44C} assembly. (d) Image of (c) processed by a band-pass filter within the cutoff wavelengths of 3.3 nm and 23.8 nm.

Figure 3-6. In contrast, PNIPAAm-HTHP^{V44C} without cross-linkages as a reference has a small annular structure at room temperature. These AFM results and the aforementioned DLS results confirm the structure of the micellar HTHP assembly with an inner PNIPAAm core.

To explore the decrease of the micelle size upon cross-linking, the micellar assembly was constructed at room temperature in the presence of salt, which is known to lower the LCST of PNIPAAm.[48] The addition of ammonium sulfate to a PNIPAAm-HTHP^{V44C} solution served to decrease the LCST below room temperature, and the micellar assembly was constructed without heating. The size of micellar assembly obtained upon addition of ammonium sulfate was evaluated by DLS measurements (Figure 3-8). In the presence of 500 mM ammonium sulfate, the size of the micellar assembly reaches 43 nm, which is consistent with the hydrodynamic diameter value of the micellar assembly constructed by heating. Further addition of ammonium sulfate at 20 ºC does not significantly change its size. Next, the micellar assembly formed in the presence of ammonium sulfate was observed by HS-AFM (Figure 3-9). Although the size of the micellar assembly is consistent with the size determined from the DLS results, the protein units at the surface of the micellar assembly move rapidly. This observation indicates that the decrease in size of the cross-linked micellar assembly occurs because of the following events: the movement of proteins provides certain interprotein spaces within the loosely packed protein units at the surface of the micellar assembly, and the cross-linking of the protein units induces tight packing of the proteins to decrease the size of the micellar assembly.

Construction of a light-harvesting model

The author evaluated the photochemical properties of the micellar assembly in the context of its potential use as a model of a light-harvesting system, because the spherical structure of the obtained micellar assembly is similar to the structures of natural light-harvesting systems.[42] Since light-harvesting systems possess an array of photosensitizers, PNIPAAm-HTHP^{V44C} containing photosensitizers was prepared as shown in Figure 3-10a. The native heme cofactor was removed from HTHP^{V44C} by conventional acid denaturation and extraction with 2-butanone.[49] Removal of heme was confirmed by UV–vis spectroscopy, indicating a lack of heme-derived absorption in the visible region. Excess Zn protoporphyrin IX, ZnPP, as a photosensitizer was added into a solution of apoHTHP^{V44C} under neutral-pH conditions, yielding the reconstituted HTHP^{V44C} (ZnPP$^{(6/6)}$HTHP^{V44C}), where 6/6 shows the complete binding of ZnPP into the six heme pockets of apoHTHP^{V44C}. The UV–vis absorption spectrum of ZnPP$^{(6/6)}$HTHP^{V44C} is similar to that of HTHP^{WT} reconstituted with ZnPP as reported previously.[50,51] As a reference sample, a protein (ZnPP$^{(1/6)}$HTHP^{V44C}) where only one heme pocket is occupied by ZnPP was prepared by mixing apoHTHP^{V44C} and ZnPP$^{(6/6)}$HTHP^{V44C} with a ratio of 5 : 1 (Figure 3-10b). These obtained proteins reconstituted with ZnPP are described as

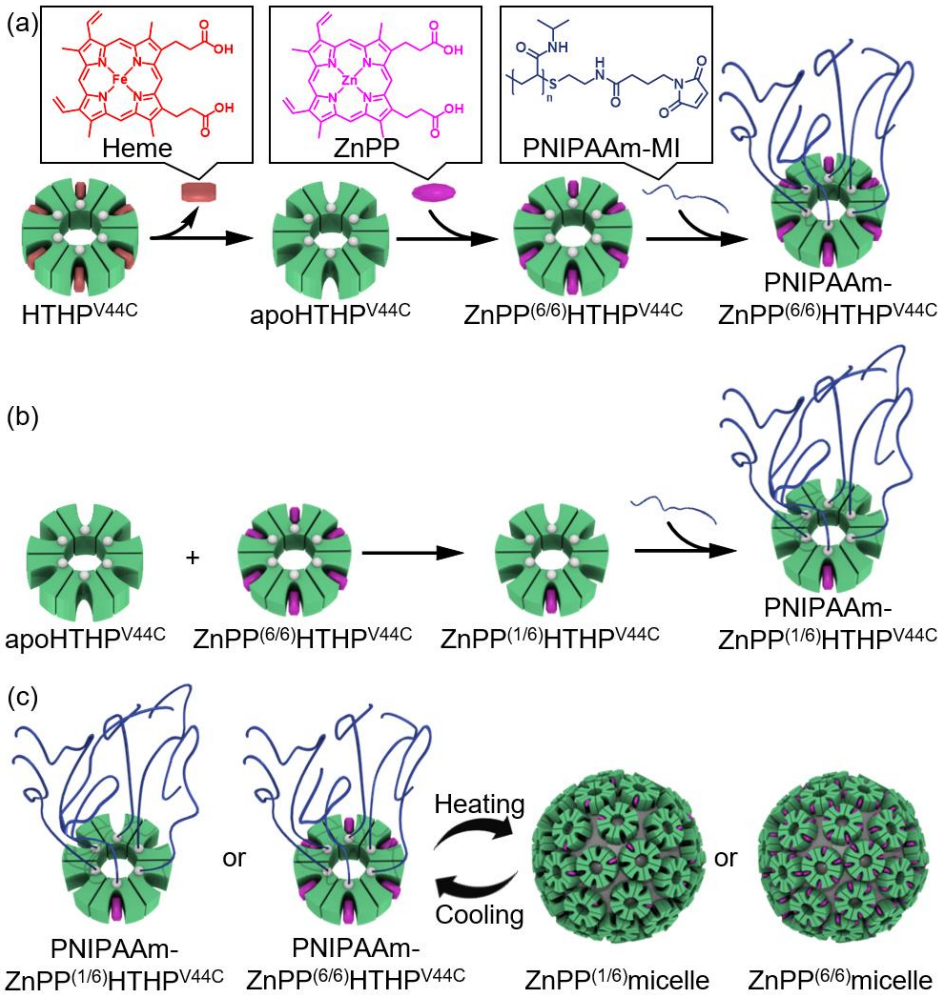

Figure 3-10. Schematic representation of the preparation of (a) PNIPAAm-ZnPP$^{(6/6)}$HTHP^{V44C}, (b) PNIPAAm-ZnPP$^{(1/6)}$HTHP^{V44C} and (c) ZnPP$^{(n/6)}$micelle.

ZnPP$^{(n/6)}$HTHP^{V44C}, where *n* represents the apparent number of ZnPP for HTHP having six heme pockets. The obtained ZnPP$^{(n/6)}$HTHP^{V44C} was reacted with PNIPAAm-MI in the same manner to prepare PNIPAAm-HTHP^{V44C}. ZnPP$^{(n/6)}$HTHP^{V44C} was confirmed by UV–vis and CD spectra and analytical SEC (Figures 3-11, 3-12 and 3-13). The absorption spectrum of PNIPAAm-ZnPP$^{(1/6)}$HTHP^{V44C} in the visible region is quite similar to that of PNIPAAm-ZnPP$^{(6/6)}$HTHP^{V44C}. CD spectra of PNIPAAm-ZnPP$^{(n/6)}$HTHP^{V44C} in the visible region are identical to spectra reported previously.[50] The CD spectrum of PNIPAAm-ZnPP$^{(1/6)}$HTHP^{V44C} only shows a positive Cotton effect due to exciton coupling between ZnPP and amino acid residues, while the CD spectrum of PNIPAAm-ZnPP$^{(6/6)}$HTHP^{V44C} is slightly more complicated. The differential CD spectrum obtained by subtraction of the CD spectrum of PNIPAAm-ZnPP$^{(1/6)}$HTHP^{V44C} from that of PNIPAAm-ZnPP$^{(6/6)}$HTHP^{V44C} affords the characteristic split-type Cotton effect derived from ZnPP–ZnPP exciton coupling. The DLS measurement indicates that PNIPAAm-ZnPP$^{(n/6)}$HTHP^{V44C} shows thermoresponsive assembling behavior (Figure 3-14) providing a micellar assembly (ZnPP$^{(n/6)}$micelle) for photochemical measurements (Figure 3-10c).

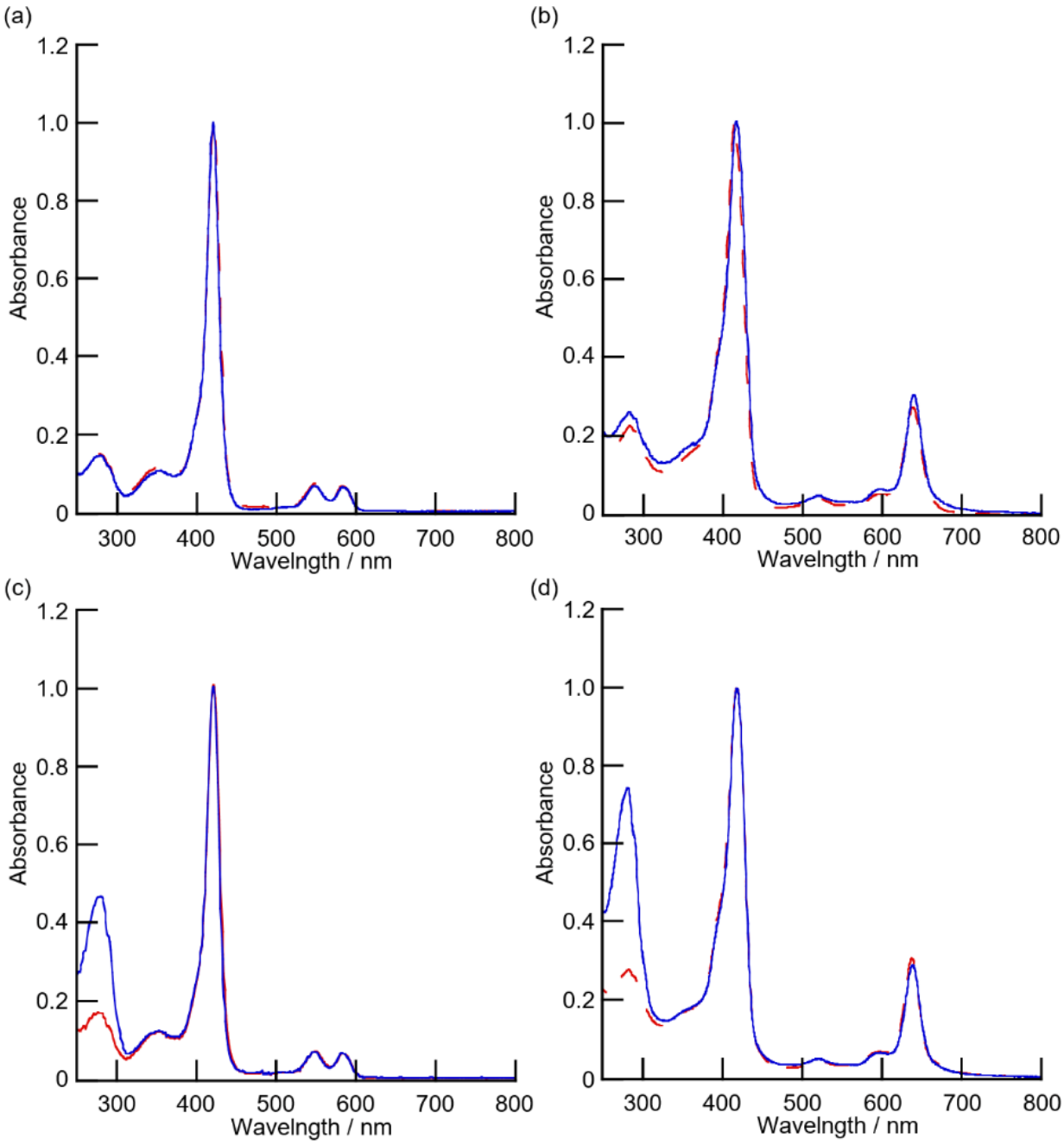

Figure 3-11. UV–vis spectra of (a) ZnPP$^{(6/6)}$HTHP^{V44C} (blue) compared to HTHP^{WT} reconstituted with ZnPP (red), (b) ZnCe$_6$$^{(6/6)}$HTHP^{V44C} (blue) compared to HTHP^{WT} reconstituted with ZnCe$_6$ (red), (c) PNIPAAm-ZnPP$^{(1/6)}$HTHP^{V44C} (blue) compared to PNIPAAm-ZnPP$^{(6/6)}$HTHP^{V44C} (red), and (d) PNIPAAm-ZnCe$_6$$^{(1/6)}$HTHP^{V44C} (blue) compared to PNIPAAm-ZnCe$_6$$^{(6/6)}$HTHP^{V44C} (red).

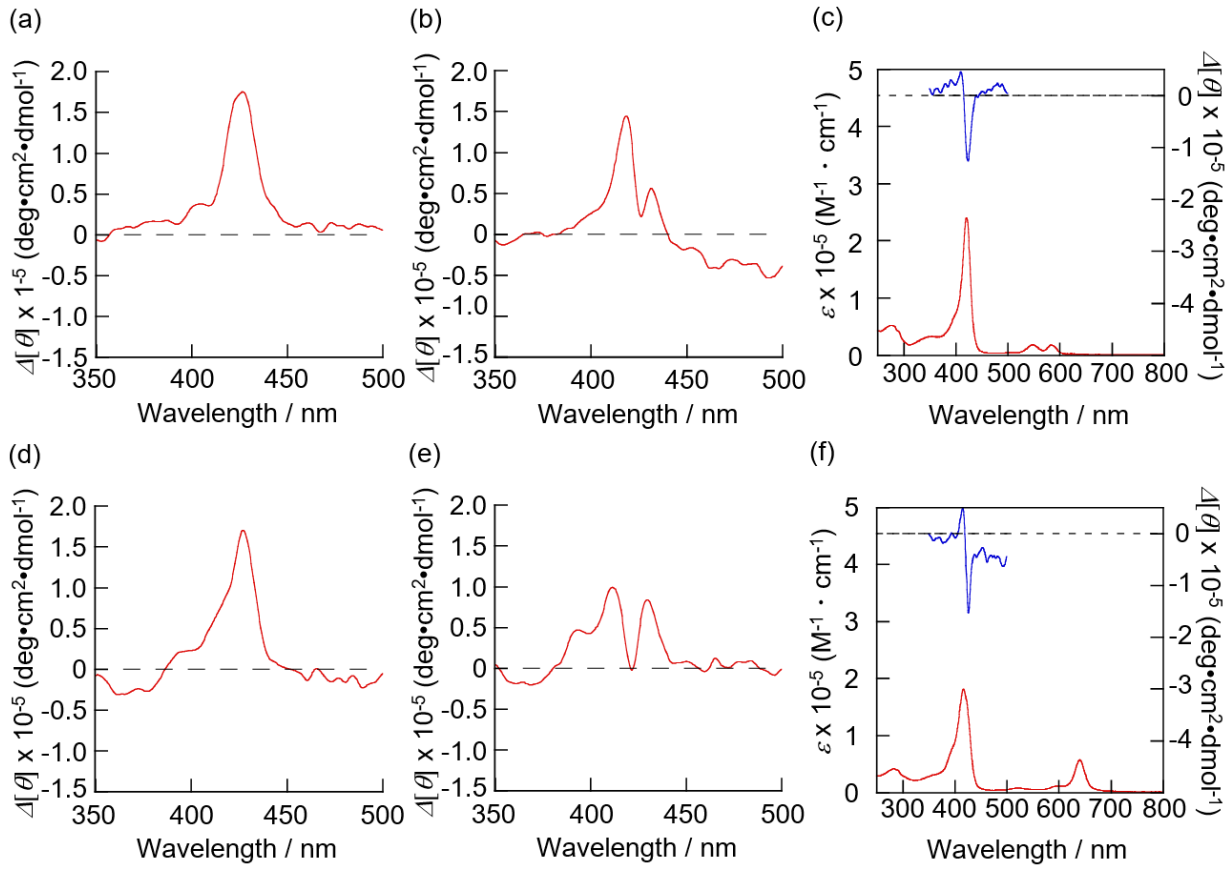

Figure 3-12. CD spectra of (a) PNIPAAm-ZnPP$^{(1/6)}$HTHP^{V44C} and (b) PNIPAAm-ZnPP$^{(6/6)}$HTHP^{V44C}. (c) UV–vis spectrum (red) of PNIPAAm-ZnPP$^{(6/6)}$HTHP^{V44C} and Differential CD spectrum (blue) generated by the subtraction of the CD spectrum of PNIPAAm-ZnPP$^{(1/6)}$HTHP^{V44C} from that of PNIPAAm-ZnPP$^{(6/6)}$HTHP^{V44C}. CD spectra of (d) PNIPAAm-ZnCe$_6^{(1/6)}$HTHP^{V44C} and (e) PNIPAAm-ZnCe$_6^{(6/6)}$HTHP^{V44C}. (f) UV–vis spectrum (red) of PNIPAAm-ZnCe$_6^{(6/6)}$HTHP^{V44C} and Differential CD spectrum (blue) generated by the subtraction of the CD spectrum of PNIPAAm-ZnCe$_6^{(1/6)}$HTHP^{V44C} from that of PNIPAAm-ZnCe$_6^{(6/6)}$HTHP^{V44C}.

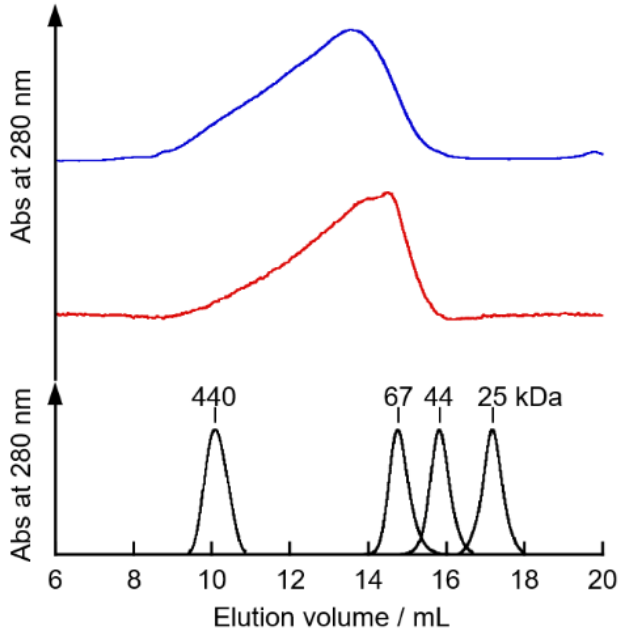

Figure 3-13. SEC traces of PNIPAAm-ZnPP$^{(1/6)}$HTHP^{V44C} (blue), PNIPAAm-ZnPP$^{(6/6)}$HTHP^{V44C} (red) and authentic samples (black)

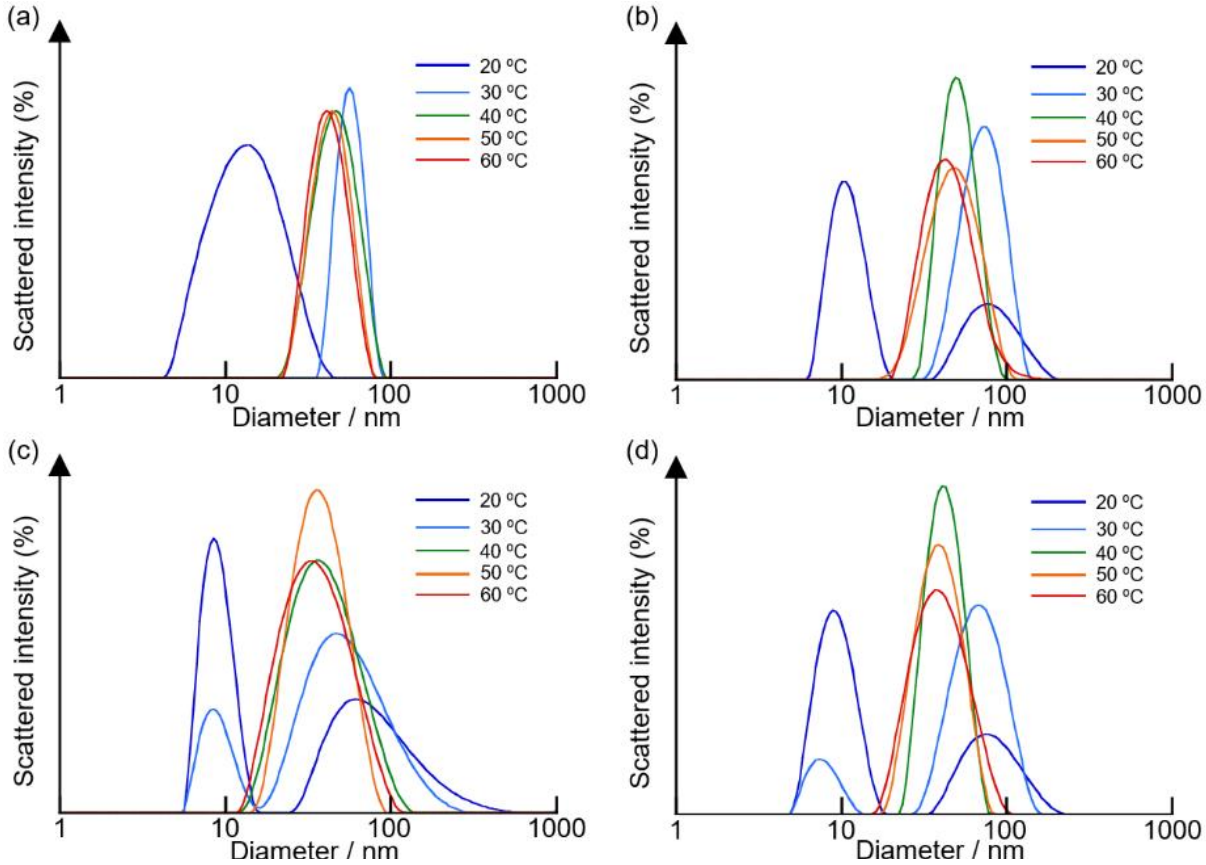

Figure 3-14. Size distributions obtained from DLS analysis for a 50 μM solution of (a) PNIPAAm-ZnPP$^{(1/6)}$HTHP^{V44C} and (b) PNIPAAm-ZnPP$^{(6/6)}$HTHP^{V44C} (c) PNIPAAm-ZnCe$_6$$^{(1/6)}$HTHP^{V44C} and (d) PNIPAAm-ZnCe$_6$$^{(6/6)}$HTHP^{V44C} in 100 mM potassium phosphate buffer (pH = 7.0) at various temperatures.

Fluorescence quenching

Energy migration among ZnPP molecules at the surface of the micellar assembly was evaluated by fluorescence quenching.[50,52] The experiment was conducted at 60 ºC, where the micellar assembly forms. The ZnPP concentration is the same for the ZnPP$^{(1/6)}$micelle and the ZnPP$^{(6/6)}$micelle. The fluorescence intensity data (Figure 3-15) were applied to the Stern-Volmer equation (1),

$$\frac{I_0}{I} = 1 + K_{SV}[Q] \quad (1)$$

where I represents the fluorescence intensity at an individual concentration of quencher, K_{SV} is the Stern–Volmer constant, and [Q] is concentration of the quencher. The Stern–Volmer plots obtained by steady-state fluorescence in the presence of the various concentrations of methyl viologen dichloride (MV^{2+}) as a fluorescence quencher are shown in Figure 3-16. The slopes of the Stern-Volmer plots, the determined K_{SV} values of ZnPP$^{(n/6)}$micelle, were 24 M^{-1} (n = 1) and 46 M^{-1} (n = 6), respectively, as apparent binding constants. The actual binding constant of MV^{2+} for ZnPP$^{(6/6)}$micelle was found to be 24 M^{-1} as determined by titrimetric experiments using UV–vis spectroscopy (Figure 3-17) to evaluate formation of the charge-transfer complex. This value is similar to that of the ZnPP$^{(1/6)}$micelle (ca. 25 M^{-1}) determined from UV–vis absorption changes (Figure 3-17). These findings indicate that the higher apparent binding constant determined for the ZnPP$^{(6/6)}$micelle is derived from efficient fluorescence quenching, which could occur as a result of the energy migration within the ZnPP array.[53] In contrast, the apparent binding constant of the ZnPP$^{(1/6)}$micelle obtained in fluorescence quenching experiments is consistent with the actual binding constant due to a lack of efficient energy migration.

One of the advantages of utilizing a hemoprotein unit is that the heme cofactor can be easily replaced with other porphyrinoid photosensitizers. To demonstrate this concept, PNIPAAm-HTHP^{V44C} reconstituted with Zn chlorine e_6 ($ZnCe_6$) (Figure 3-18) was prepared. The obtained protein, which is given the designation PNIPAAm-$ZnCe_6^{(n/6)}$HTHP^{V44C}, was also characterized by UV–vis and CD spectroscopies (Figures 3-11 and 3-12). The DLS measurements (Figure 3-14) indicate that PNIPAAm-$ZnCe_6^{(n/6)}$HTHP^{V44C} also forms a corresponding micellar assembly with ca. 43-nm diameter ($ZnCe_6^{(n/6)}$micelle). The apparent binding constants of MV^{2+} derived from the Stern–Volmer plots of $ZnCe_6^{(n/6)}$micelle were determined to be 5.1 × 10^2 M^{-1} (n = 6) and 1.7 × 10^2 M^{-1} (n = 1), respectively (Figures 3-19 and 3-20), whereas the actual binding constants of MV^{2+} for the $ZnCe_6^{(n/6)}$micelle were found to be 82 M^{-1} and 72 M^{-1}, respectively, as determined by UV–vis titrimetric spectral changes (Figure 3-21). The remarkable difference between the apparent and actual binding constant of the $ZnCe_6^{(1/6)}$micelle indicates that efficient energy migration occurs among hexamer units relative to the micellar assembly containing ZnPP. These results suggest that this protein assembly will be useful for construction of a light-harvesting antenna with various porphyrinoid photosensitizers.

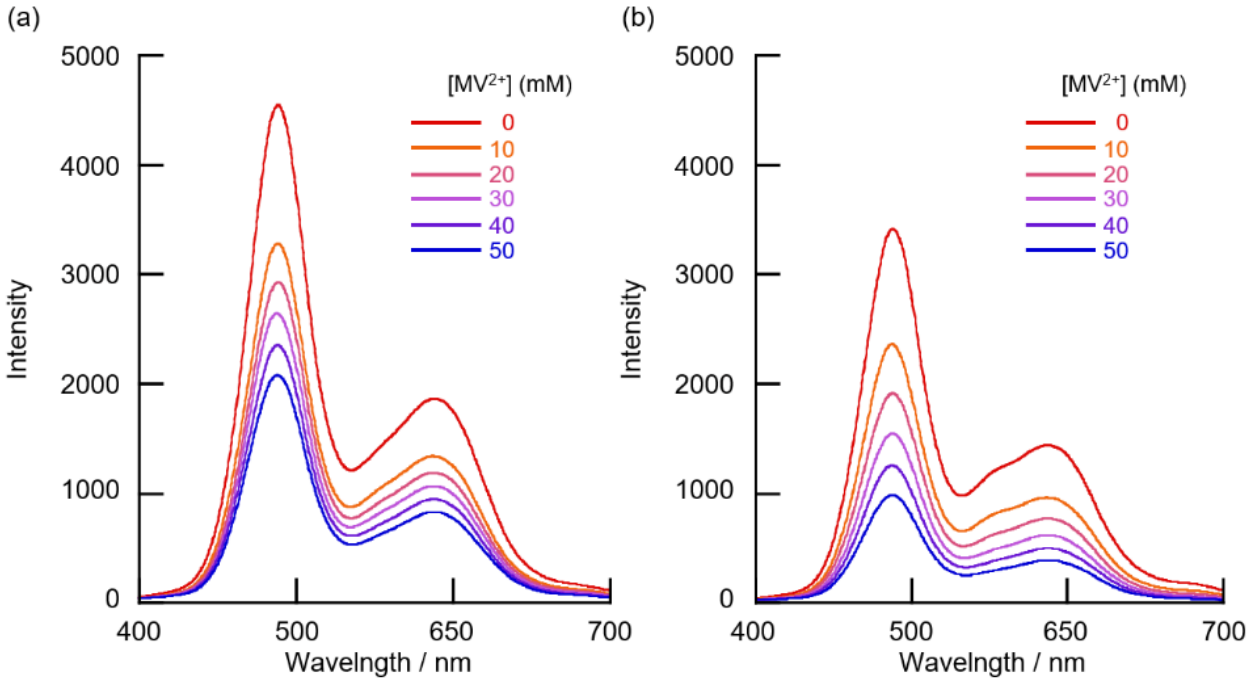

Figure 3-15. Fluorescence spectral changes of (a) ZnPP$^{(1/6)}$micelle and (b) ZnPP$^{(6/6)}$micelle upon addition of MV^{2+}. Conditions: [ZnPP] = 10 μM in 100 mM potassium phosphate buffer, pH 7.0, at 60 ºC under an N_2 atmosphere and λ_{ex} = 421 nm.

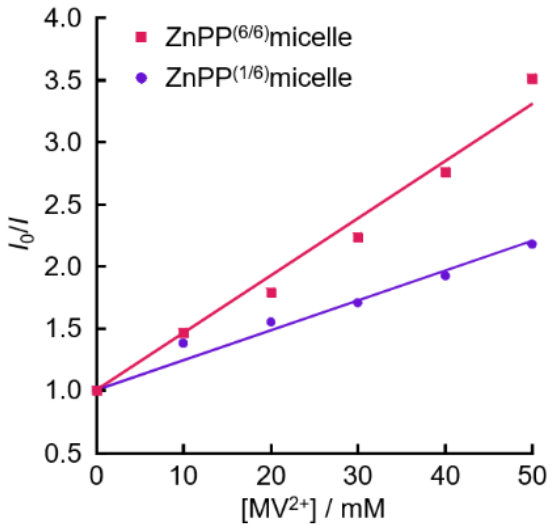

Figure 3-16. Stern–Volmer plots of steady-state fluorescence for ZnPP$^{(n/6)}$micelle in the presence of various concentrations of quencher. Methyl viologen was used as a quencher molecule. Solid lines show corresponding fitting. Conditions: [ZnPP] = 10 μM in buffer at 60 ºC under an N_2 atmosphere, λ_{ex} = 421 nm, λ_{em} = 593 nm.

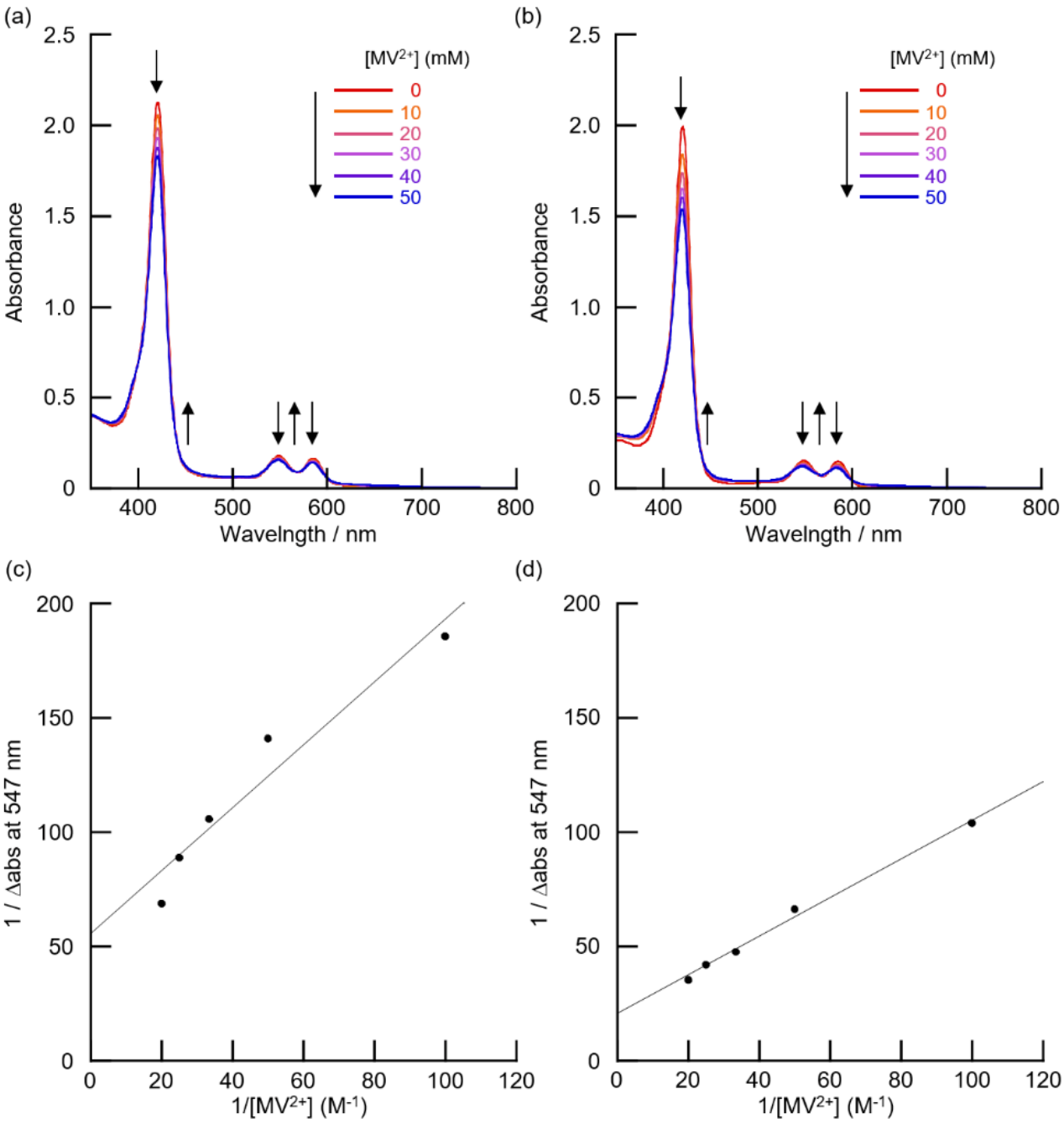

Figure 3-17. UV–vis spectral changes of (a) ZnPP$^{(1/6)}$micelle and (b) ZnPP$^{(6/6)}$micelle upon addition of MV^{2+} and the Benesi–Hildebrand plots of (c) ZnPP$^{(1/6)}$micelle and (d) ZnPP$^{(6/6)}$micelle at 547-nm absorption against various MV^{2+} concentrations. The plots were analyzed by the following equation: $(\Delta\text{Abs})^{-1} = (K_a(\Delta\varepsilon)[\text{ZnPP}]_0[MV^{2+}])^{-1} + ((\Delta\varepsilon)[\text{ZnPP}]_0)^{-1}$, where K_a and $\Delta\varepsilon$ are the binding constant and differential extinction coefficient by subtraction of that of the MV^{2+}-free photosensitizer from that of the MV^{2+}-bound photosensitizer, respectively. Conditions: $[\text{ZnPP}]_0$ = 10 μM in 100 mM potassium phosphate buffer, pH 7.0, at 60 ºC.

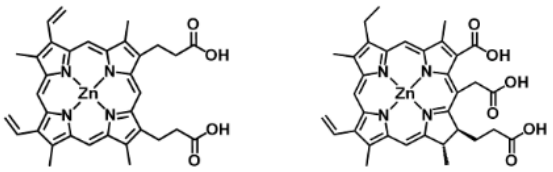

Figure 3-18. Molecular structures of Zn protoporphyrin IX (left) and Zn chlorin e_6 (right)

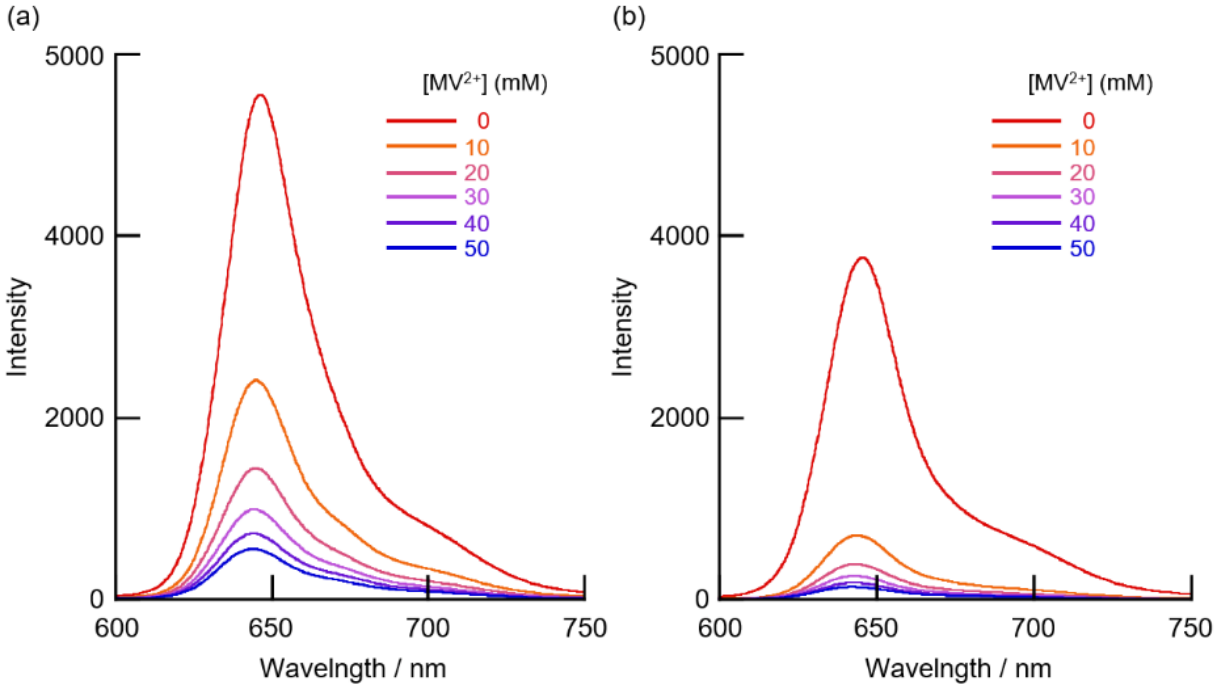

Figure 3-19. Fluorescence spectral changes of (a) $ZnCe_6^{(1/6)}$micelle and (b) $ZnCe_6^{(6/6)}$micelle upon addition of MV^{2+}. Conditions: [$ZnCe_6$] = 9 μM in 100 mM potassium phosphate buffer, pH 7.0, at 60 ºC under an N_2 atmosphere and λ_{ex} = 418 nm.

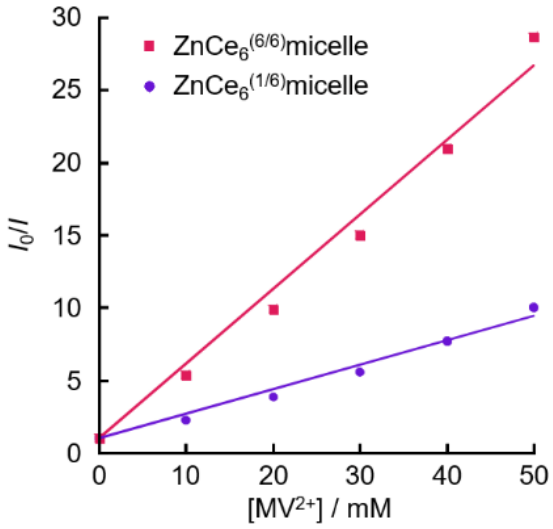

Figure 3-20. Stern–Volmer plots of steady-state fluorescence against the concentration of methyl viologen as a quencher molecule for $ZnCe_6^{(n/6)}$micelle. Solid lines show corresponding least square fitting. Conditions: [$ZnCe_6$] = 9 μM in 100 mM potassium phosphate buffer, at pH 7.0, at 60 ºC under an N_2 atmosphere, λ_{ex} = 418 nm, λ_{em} = 645 nm.

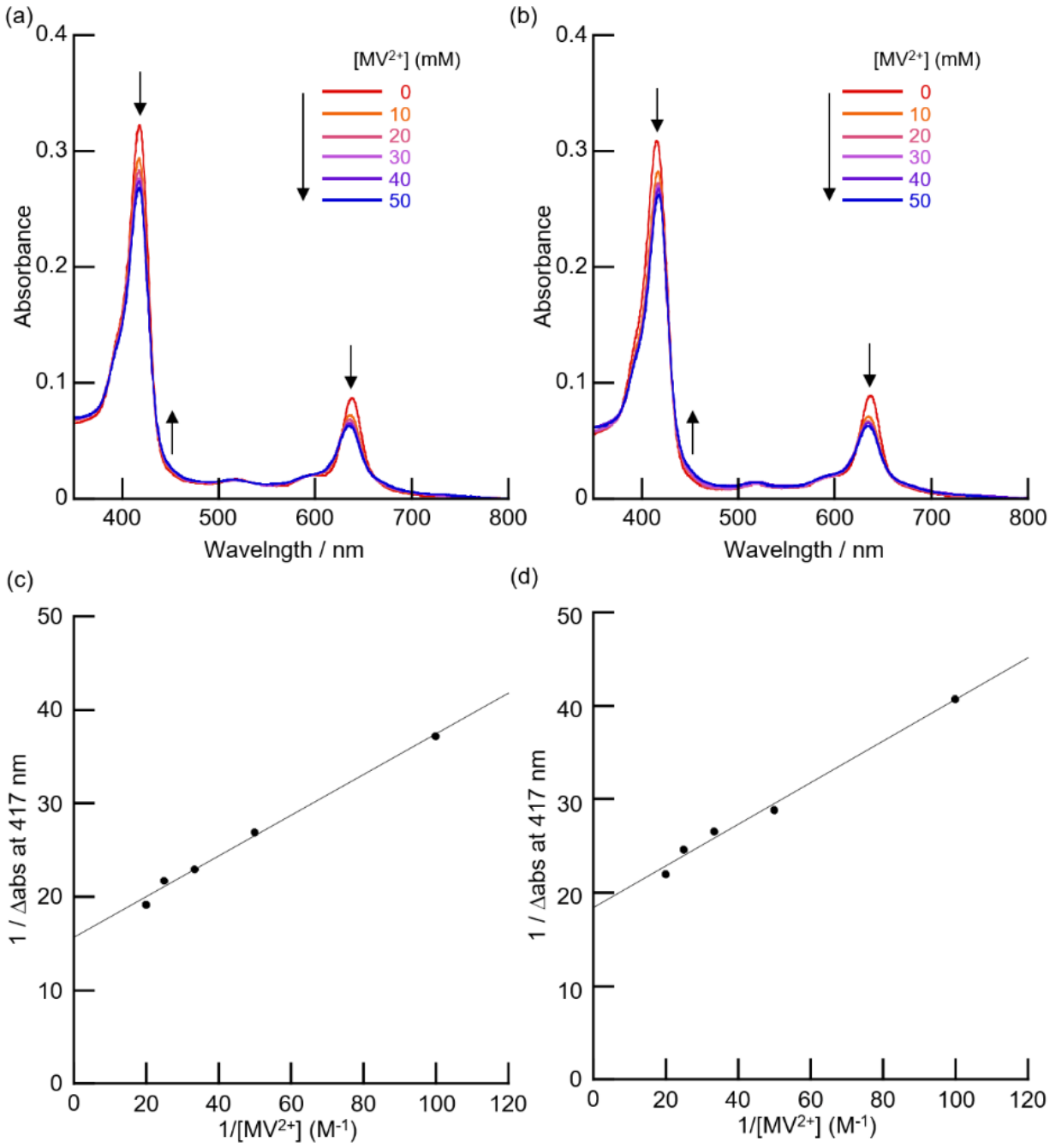

Figure 3-21. UV-vis spectral changes of (a) $ZnCe_6^{(1/6)}$micelle and (b) $ZnCe_6^{(6/6)}$micelle upon addition of MV^{2+} and the Benesi–Hildebrand plots of (c) $ZnCe_6^{(1/6)}$micelle and (d) $ZnCe_6^{(6/6)}$micelle at 417-nm absorption against various MV^{2+} concentrations. The plots were analyzed by the following equation: $(\Delta\text{Abs})^{-1} = (K_a(\Delta\varepsilon)[ZnCe_6]_0[MV^{2+}])^{-1} + ((\Delta\varepsilon)[ZnCe_6]_0)^{-1}$, where K_a and $\Delta\varepsilon$ are the binding constant and differential extinction coefficient by subtraction of that of the MV^{2+}-free photosensitizer from that of the MV^{2+}-bound photosensitizer, respectively. Conditions: $[ZnCe_6]_0$ = 9 μM in 100 mM potassium phosphate buffer, pH 7.0, at 60 ºC.

Fluorescence lifetime and fluorescence anisotropy decay

In a further investigation of the energy migration, time-dependent fluorescence measurements were conducted (Table 3-2). First, time-resolved fluorescence decays of the ZnPP$^{(n/6)}$micelle (Figure 3-22) were measured at 60 ºC. The fluorescence lifetimes (τ) are summarized in Table 3-2. The fluorescence lifetime of the ZnPP$^{(6/6)}$micelle (0.90 ns) is somewhat shorter than that of the ZnPP$^{(1/6)}$micelle (1.10 ns). The cofactor number-dependent fluorescence lifetime is also seen in the case of HTHP^{WT} reconstituted with ZnPP at room temperature[50], suggesting that the decrease of the τ value could be derived from singlet–singlet annihilation via inter- and intrahexamer energy migrations.[54] Moreover, the lifetime of ZnPP$^{(n/6)}$HTHP^{V44C} is shorter than that of the corresponding micelles. This decrease of lifetime is plausibly induced by the quenching of fluorescence by the solvent[55] because the ZnPP molecule in the hexamer is considerably more exposed to water than it is in the micellar assembly.

The time-dependent fluorescence anisotropy decays of ZnPP$^{(n/6)}$HTHP^{V44C} and the ZnPP$^{(n/6)}$micelle (Figure 3-23) were also measured at 60 ºC after changing the detecting polarization (horizontal or vertical) of the fluorescence to vertically polarized excitation light.[56] The time-dependent fluorescence anisotropy values $r(t)$ for ZnPP$^{(n/6)}$HTHP^{V44C} and the ZnPP$^{(n/6)}$micelle were fitted to a double-exponential curve (2),

$$r(t) = r_0 \{\alpha_1 \exp\left(-\frac{t}{\theta_1}\right) + \alpha_2 \exp\left(-\frac{t}{\theta_2}\right)\} \quad (2)$$

where r_0 is the initial anisotropy, α_1 and α_2 are populations of the decay, and θ_1 and θ_2 are the fluorescence anisotropy decay time constants. These θ values are interpreted to originate from the rotational motion of the photosensitizer. These parameters are summarized in Table 3-2. The rotational correlation time of a spherical object is determined by equation (3),[57]

$$\theta = \frac{\eta V}{kT} \quad (3)$$

where η represents the viscosity, V represents the volume, k represents the Boltzmann constant and T represents the absolute temperature. The expected rotational correlation time of the hexamer is about 10 ns, and that of the micellar assembly is longer than 3 μs, as estimated by equation (3). This expectation suggests that θ_2 would originate from the rotational motion of the hexameric structure of HTHP, whereas the θ_1 value does not originate from the rotation. One possible reason for this value is anisotropy decay by thermal vibration of ZnPP.[55] The heme pocket of HTHP is relatively shallow, and it is possible that ZnPP in the pocket has some mobility as a result of the high temperature. The population of the decay depends on the amount of the cofactor in the protein matrix. This difference

suggests that the thermal vibration of ZnPP in partially reconstituted HTHP occurs more easily than that of fully reconstituted HTHP.

The r_0 value is the fluorescence anisotropy in the absence of rotational motion. In the present system, this r_0 value depends on the efficiency of the energy migration within several tens of picoseconds.[58] Thus, the smaller r_0 value suggests that energy migration occurs more rapidly. The r_0 value in the fluorescence anisotropy decay of ZnPP$^{(6/6)}$HTHP^{V44C} is found to be smaller than that of ZnPP$^{(1/6)}$HTHP^{V44C} because of efficient energy migration occurring within the ZnPP array in the hexameric structure of HTHP.[51] Moreover, the ZnPP$^{(6/6)}$micelle has a remarkably small r_0 value compared to other samples. This finding indicates that rapid energy migration occurs on the surface of the ZnPP$^{(6/6)}$micelle.

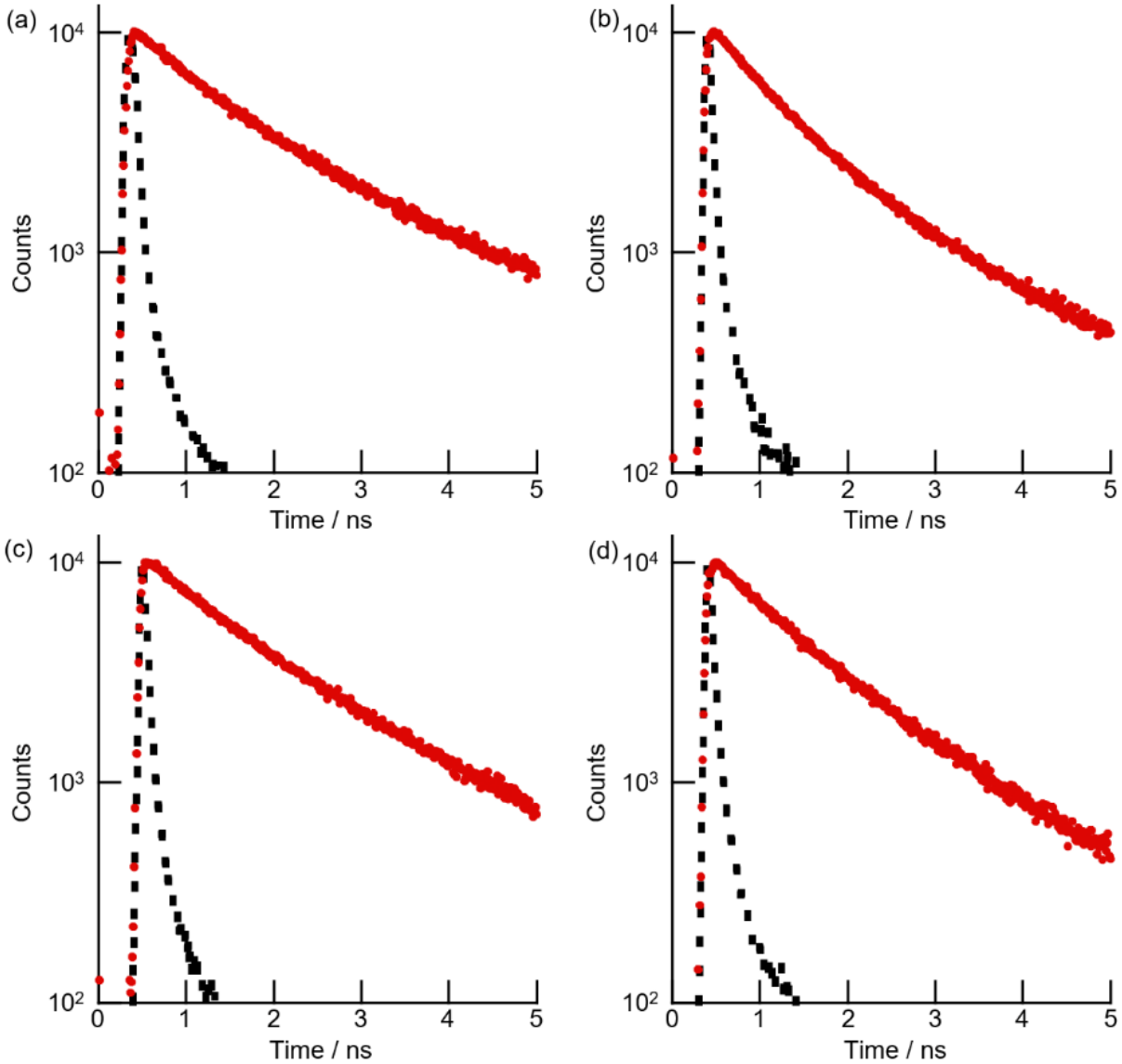

Figure 3-22. Time-resolved fluorescence decay profiles of (a) ZnPP$^{(1/6)}$HTHP^{V44C}, (b) ZnPP$^{(1/6)}$micelle, (c) ZnPP$^{(6/6)}$HTHP^{V44C} and (d) ZnPP$^{(6/6)}$micelle. The instrument response is shown by the black broken line. [ZnPP] = 10 μM in 100 mM potassium phosphate buffer, pH 7.0, at 60 ºC under an N_2 atmosphere, λ_{ex} = 404 nm and λ_{em} = 593 nm.

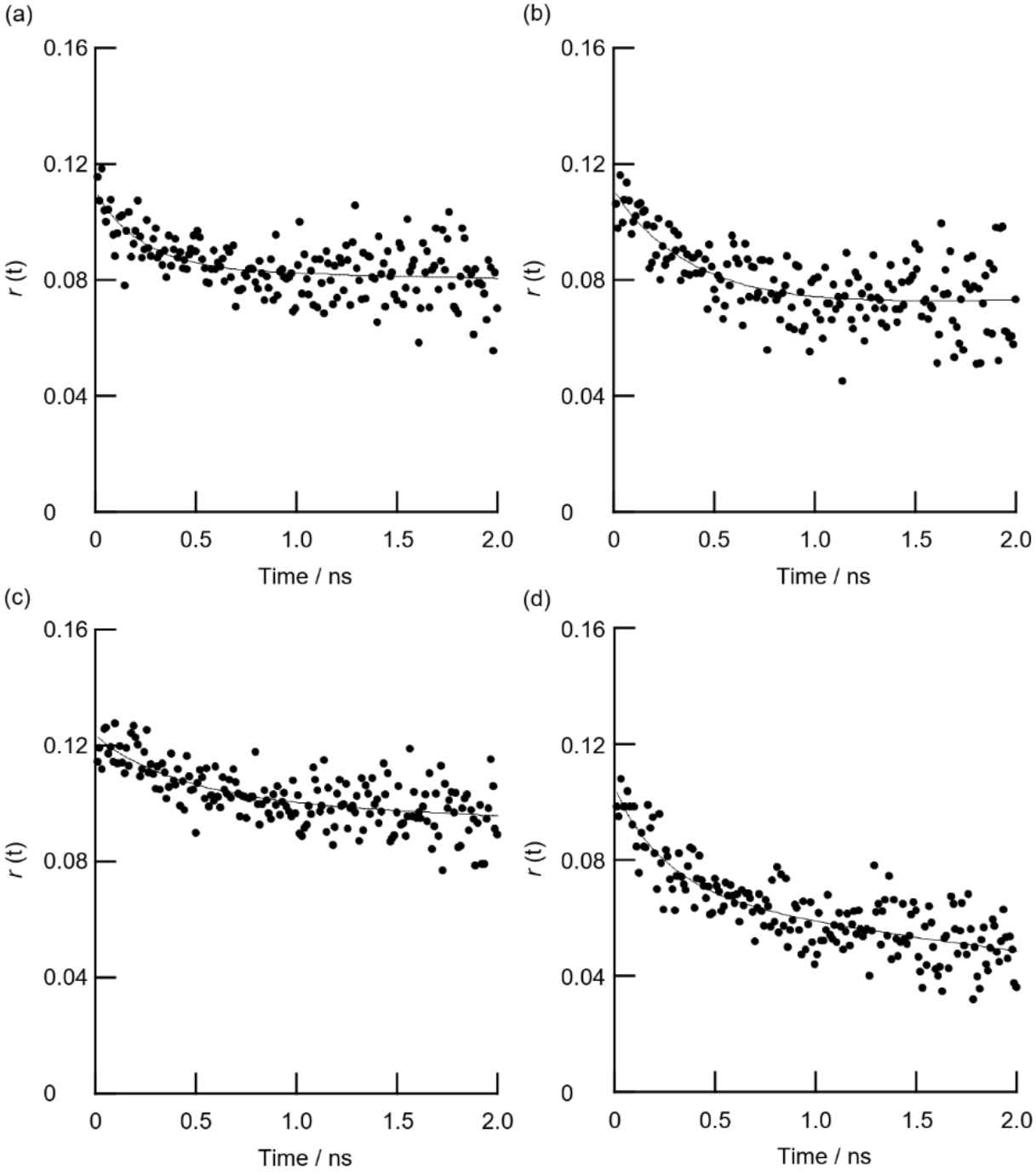

Figure 3-23. Time-resolved fluorescence anisotropy decay profiles of (a) $ZnPP^{(1/6)}HTHP^{V44C}$, (b) $ZnPP^{(1/6)}$micelle, (c) $ZnPP^{(6/6)}HTHP^{V44C}$ and (d) $ZnPP^{(6/6)}$micelle. Decay plots were analyzed by double-exponentially fitted curves (solid lines): $r(t) = r_0\{\alpha_1\exp(-t/\theta_1) + \alpha_2\exp(-t/\theta_2)\}$, where r_0 is initial anisotropy, θ_1 and θ_2 are the fluorescence anisotropy decay time constants and α_1 and α_2 are population of decays. [ZnPP] = 10 μM in 100 mM potassium phosphate buffer, pH 7.0, at 60 ºC under an N_2 atmosphere, λ_{ex} = 404 nm and λ_{em} = 593 nm.

Table 3-2. Fluorescence decay and fluorescence anisotropy decay parameters of $ZnPP^{(n/6)}HTHP^{V44C}$ and the $ZnPP^{(n/6)}$micelle[a]

Sample	τ (ns)	r_0	α_1	θ_1 (ns)	α_2	θ_2 (ns)
$ZnPP^{(1/6)}HTHP^{V44C}$	0.97 ± 0.01	0.14 ± 0.02	0.21	0.34 ± 0.11	0.79	18 ± 8.4
$ZnPP^{(1/6)}$micelle	1.10 ± 0.01	0.12 ± 0.01	0.23	0.26 ± 0.11	0.77	13 ± 2.0
$ZnPP^{(6/6)}HTHP^{V44C}$	0.70 ± 0.01	0.12 ± 0.01	0.37	0.42 ± 0.08	0.63	14 ± 3.5
$ZnPP^{(6/6)}$micelle	0.90 ± 0.01	0.10 ± 0.01	0.41	0.39 ± 0.14	0.59	8.3 ± 2.5

[a] Conditions: [ZnPP] = 10 μM in 100 mM potassium phosphate buffer, pH = 7.0 and 60 ºC under N_2 atmosphere, λ_{ex} = 404 nm.

3-3. Summary

Construction of a micellar assembly of a ring-shaped thermostable hemoprotein in combination with a thermoresponsive polymer was achieved. The structure of the protein is maintained during the heating and cooling processes, and the size of the micellar assembly is essentially monodispersed. HS-AFM measurements of the cross-linked assembly reveal that the obtained protein assembly has a micellar structure consisting of a polymer core and a protein shell, which has similarities with the spherical chromatophore from *Rhodobacter sphaeroides*.[42] The obtained micellar assembly was investigated as a model of light-harvesting system after substitution of heme with ZnPP as a photosensitizer. Energy migration within the ZnPP-substituted micelle occurs among the photosensitizers located at the surface of the micellar assembly within several tens of picoseconds. This protein assembly represents a functional model of a light-harvesting system and will be applied to an artificial photosynthesis reaction in the future.

3-4. Experimental section

Material and methods

A Shimadzu BioSpec-nano spectrophotometer, a Shimadzu UV-2550 or UV-3150 double-beam spectrophotometer, or a V-670 UV–vis–NIR spectrophotometer (JASCO) was used to record UV–vis absorption spectra. The pH values were monitored with a Horiba F-52 pH meter or F-72 pH meter. A Bruker autoflex III mass spectrometer was used for MALDI-TOF MS analysis. Circular dichroism (CD) spectra were recorded with a JASCO J-820S spectrometer. An ÄKTApurifier system (GE Healthcare) was utilized for size exclusion chromatographic (SEC) analyses. A Zetasizer μV (Malvern Instruments) was used for dynamic light scattering (DLS) experiments, where the laser wavelength was 830 nm. A Hamamatsu Photonics picosecond fluorescence lifetime measurement system C11200 was utilized for time-resolved fluorescence anisotropy decay experiments. As the excitation light source, a Hamamatsu Photonics picosecond light pulser PLP-10 was employed. $HTHP^{V44C}$ was prepared according to the reported procedures.[43] The apo form of $HTHP^{V44C}$ was obtained using modified Teale's method.[49,50] Synthesis of Zn protoporphyrin IX (ZnPP) was reported

in the previous paper.[59] A Merck Millipore Integral 3 apparatus provided ultrapure water (Milli-Q). PNIPAAm-maleimide was obtained from Sigma-Aldrich and purified by a HiTrap Desalting column (GE Healthcare) just before use. Other all reagents were commercially available and used as received. As a buffer solution, 100 mM potassium phosphate buffer, pH 7.0, was used.

Protein sequences

$HTHP^{WT}$:

SETWLPTLVTATPQEGFDLAVKLSRIAVKKTQPDAQVRDTLRAVYEKDANALIAVSAVVATHF QTIAAANDYWKD.

$HTHP^{V44C}$:

SETWLPTLVTATPQEGFDLAVKLSRIAVKKTQPDAQVRDTLRACYEKDANALIAVSAVVATHF QTIAAANDYWKD.

Analytical SEC measurements and preparative SEC purification

Buffer was employed as an SEC eluent. Both the analysis and purification were carried out at 4 ºC, and the flow rate and detection wavelength for absorbance were 0.5 mL min^{-1} and 280, 402 or 421 nm. Analytical SEC was performed with a Superdex 200 increase 10/300 GL (GE Healthcare) column calibrated by the following protein standards: ferritin (440 kDa), albumin (67 kDa), ovalubumin (44 kDa) and chymotripsinogen (25 kDa). Preparative SEC was performed by a Superose 6 column (GE Healthcare).

Preparation of PNIPAAm-$HTHP^{V44C}$

Into an $HTHP^{V44C}$ solution (500 μM, 900 μL), a 1 M DTT aqueous solution (100 μL) was added, and the solution stood at 50 ºC for 1 h. The protein was purified by a HiTrap Desalting column to provide a protein solution (2.0 mL). Maleimide-terminated PNIPAAm (PNIPAAm-MI, M_n = 5,500) (24.7 mg, 10 eq) was dissolved in buffer (500 μL) and purified using a HiTrap Desalting column. Into the protein solution, the purified PNIPAAm-MI solution (1.0 mL) was added and incubated at 4 ºC for 2 h. The solution was loaded onto a DEAE Fast Flow anion-exchange column which was pre-equilibrated in buffer. The target protein fraction was collected in buffer containing 0.5 M NaCl, pH 7.0. This fraction was dialyzed in buffer and PNIPAAm-HTHP (300 μM, 3.0 mL) was obtained. The modified protein was characterized by SDS-PAGE and analytical SEC measurements. The modification rate was determined from the result of SDS-PAGE analyzed by ImageJ software.

Thermoresponsive size evaluation of PNIPAAm-$HTHP^{V44C}$

The thermoresponsive assembling behavior was observed from the DLS measurement (from 20 ºC to 60 ºC). For DLS measurements, an aqueous solution of PNIPAAm-$HTHP^{V44C}$ (50 μM) dissolved in buffer was used. The detailed setup is used exactly as described in the previous paper.[43] The data were obtained by the intensity-based particle size distribution mode. The DLS measurements

of PNIPAAm-HTHP^{V44C} were conducted every 10 ºC from 20 to 60 ºC. In these measurements, the samples were incubated at the target temperature for 5 min in order to wait for completion of the thermoresponsive behavior. The repetitive assembling behavior was also confirmed by DLS. The DLS measurements were repeated with an iterative heating and cooling cycle more than 5 times.

Cross-linking reaction of PNIPAAm-HTHP^{V44C}

Prior to initiating the cross-linking reaction, a solution of PNIPAAm-HTHP^{V44C} (50 μM as a monomer, 1.2 mL) in buffer was heated at 60 ºC. An aqueous solution of 1 % (w/v) glutaraldehyde (60 μL) heated at 60 ºC was added to the heated solution of PNIPAAm-HTHP^{V44C}. After incubation at 60 ºC for 1 h, glutaraldehyde was removed by dialysis with buffer (2 times) at 4 ºC. Then $NaBH_3CN$ (5.3 mg, 84 μmol) was added to the protein solution and the reaction mixture was incubated at room temperature for 1 h. $NaBH_3CN$ was removed by dialysis with buffer (2 times) at 4 ºC to obtain the cross-linked PNIPAAm-HTHP^{V44C}. The obtained product was purified by preparative SEC.

HS-AFM experiments

HS-AFM experiments were performed by a laboratory-designed HS-AFM apparatus operated in tapping mode,[60,61] and an amorphous carbon tip grown by electron-beam deposition with scanning electron microscopy.[62] The detailed setup is used exactly as described in the previous paper.[18]

For the HS-AFM imaging, the mica surface was treated with glutaraldehyde and (3-aminopropyl)triethoxysilane (APTES). First, a 3 μL droplet of 0.1% APTES diluted with pure water was placed on freshly cleaved mica. After 3-min. incubation, the substrate was washed with pure water with a volume of 70 μL. Then a 3 μL droplet of 0.25% glutaraldehyde diluted with pure water was placed on the APTES-mica. The substrate was washed with pure water of 70 μL after the 3-min incubation. Then the solution (3 μL) of cross-linked PNIPAAm-HTHP^{V44C} assembly (50 μM as a monomer) was deposited onto the glutaraldehyde/APTES-mica substrate for 3 min. The substrate was thoroughly washed with buffer to remove excess molecules. The HS-AFM experiments were carried out in buffer at room temperature.

Preparation of ZnPP$^{(6/6)}$HTHP^{V44C}

A solution of ZnPP in DMSO (1.5 mM, 405 μL) was added to a solution of apoHTHP^{V44C} (8 μM, 50 mL) in buffer. After mildly mixing at 4 ºC for 1 hour, the target protein was purified by the same method as PNIPAAm-HTHP^{V44C}. An aqueous solution of ZnPP$^{(6/6)}$HTHP^{V44C} (50 μM, 3.5 mL, 50 %) was obtained.

Preparation of ZnPP$^{(1/6)}$HTHP^{V44C}

A solution of ZnPP$^{(6/6)}$HTHP^{V44C} (50 μM, 2 mL) in buffer was added to a solution of apoHTHP^{V44C} (10 μM, 50 mL) in the same buffer and incubated at 4 ºC for 1 day to obtain ZnPP$^{(1/6)}$HTHP^{V44C}.

Preparation of PNIPAAm-ZnPP$^{(n/6)}$HTHP^{V44C}

The aqueous solution of 1 M DTT (50 μL) was added to ZnPP$^{(n/6)}$HTHP^{V44C} (1.2 mM, 500 μL) and incubated at room temperature for 1 h. DTT was removed by a HiTrap Desalting column to yield the protein solution (1 mL). PNIPAAm-MI (34 mg, 10 eq) was dissolved in buffer (0.5 mL) and purified by a HiTrap Desalting column. The purified PNIPAAm-MI solution (1.0 mL) was added into the protein solution and incubated at 4 ºC for 2 h. The target protein was purified by the same method as PNIPAAm-HTHP^{V44C}. PNIPAAm-ZnPP$^{(n/6)}$HTHP^{V44C} (50 μM, 3.0 mL) was obtained.

Preparation of PNIPAAm-apoHTHP^{V44C}

A 1 M DTT aqueous solution (50 μL) was added to apoHTHP^{V44C} (0.55 mM, 500 μL), and the solution stood at room temperature for 1 h. DTT was removed by a HiTrap Desalting column to yield the protein solution (1 mL). PNIPAAm-MI (15 mg, 10 eq) was dissolved in buffer at pH 7.0 (0.5 mL) and purified using a HiTrap Desalting column. Into the protein solution, the purified PNIPAAm-MI solution (1.0 mL) was added and the solution stood at 4 ºC for 2 h. The target protein was purified by the same method as PNIPAAm-HTHP^{V44C}. PNIPAAm-apoHTHP^{V44C} (20 μM, 6.0 mL) was obtained.

Preparation of PNIPAAm-ZnCe$_6^{(6/6)}$HTHP^{V44C}

A solution of ZnCe$_6$ in glycine–NaOH buffer at pH 10 (170 μM, 300 μL) was added to a solution of PNIPAAm-apoHTHP^{V44C} (20 μM, 1.7 mL) in buffer. After mildly mixing at 4 ºC for 10 h, the solution was dialyzed with buffer (3 times) at 4 ºC to obtain an aqueous solution of PNIPAAm-ZnCe$_6^{(6/6)}$HTHP^{V44C} (10 μM, 2.1 mL, 62 %).

Preparation of PNIPAAm-ZnCe$_6^{(1/6)}$HTHP^{V44C}

A solution of PNIPAAm-ZnCe$_6^{(6/6)}$HTHP^{V44C} (10 μM, 1.1 mL) in buffer was added to a solution of PNIPAAm-apoHTHP^{V44C} (5.5 μM, 10 mL) in the same buffer and incubated at 4 ºC for 1 day to obtain PNIPAAm-ZnCe$_6^{(1/6)}$HTHP^{V44C}.

Fluorescence quenching

The fluorescence quenching measurements of the micellar assembly of PNIPAAm-ZnPP$^{(n/6)}$HTHP^{V44C} were carried out with MV^{2+} as a fluorescence quencher at 60 ºC under an N_2 atmosphere. ZnPP in the protein assembly was excited at λ_{ex} = 421 nm. Stern–Volmer plots were obtained by steady-state fluorescence emission intensities in the presence of various concentrations of MV^{2+} made by use of the ratio about fluorescence intensity at λ_{ex} = 593 nm. The actual binding constants of MV^{2+} for PNIPAAm-ZnPP$^{(n/6)}$HTHP^{V44C} were determined with UV–vis absorption changes by the titration of MV^{2+} to form the charge-transfer complex.

Fluorescence lifetime and fluorescence anisotropy decay

The time-resolved fluorescence decays of $ZnPP^{(n/6)}HTHP^{V44C}$ and the $ZnPP^{(n/6)}$micelle were measured using a time-correlated single-photon counting system. During the fluorescence lifetime and the fluorescence anisotropy decay measurements, the number of detected fluorescence photons per unit time was retained at or below 2%. To determine the excitation of ZnPP in the micellar assembly, the Soret band (λ_{ex} = 404 nm) was employed. All of the measurements were conducted at 60 ºC under an N_2 atmosphere.

References and notes

(1) Fegan, A.; White, B.; Carlson, J. C. T.; Wagner, C. R. *Chem. Rev.* **2010**, *110*, 3315-3336.

(2) Bai, Y.; Luo, Q.; Liu, J. *Chem. Soc. Rev.* **2016**, *45*, 2756-2767.

(3) Sun, H.; Luo, Q.; Hou, C.; Liu, J. *Nano Today*, **2017**, *14*, 16-41.

(4) van Dun, S. Ottmann, C.; Milroy, L.-G.; Brunsveld, L. *J. Am. Chem. Soc.* **2017**, *139*, 13960-13968.

(5) Oohora, K.; Hayashi, T. *Curr. Opin. Chem. Biol.* **2014**, *19*, 154-161.

(6) Hirota, S. *J. Inorg. Biochem.* **2019**, *194*, 170-179.

(7) Hsia, Y.; Bale, J. B.; Gonen, S.; Shi, D.; Sheffler, W.; Fong, K. K.; Nattermann, U.; Xu, C.; Huang, P.-S.; Ravichandran, R.; Yi, S.; Davis, T. N.; Gonen, T.; King, N. P.; Baker, D. *Nature* **2016**, *535*, 136-139.

(8) Bale, J. B.; Gonen, S.; Liu, Y.; Sheffler, W.; Ellis, D.; Thomas, C.; Cascio, D.; Yeates, T. O.; Gonen, T.; King, N. P.; Baker, D. *Science* **2016**, *353*, 389-394.

(9) Lai, Y.-T.; Cascio, D.; Yeates, T. O. *Scienece* **2012**, *336*, 1129.

(10) Kobayashi, N.; Yanase, K.; Sato, T.; Unzai, S.; Hecht, M. H.; Arai, R. *J. Am. Chem. Soc.* **2015**, *137*, 11285-11293.

(11) Kawakami, N.; Kondo, H.; Matsuzawa, Y.; Hayasaka, K.; Nasu, E.; Sasahara, K.; Arai, R.; Miyamoto, K. *Angew. Chem. Int. Ed.* **2018**, *57*, 12400-12404.

(12) Simon, A. J.; Zhou, Y.; Ramasubramani, V.; Glaser, J.; Pothukuchy, A.; Gollihar, J.; Gerberich, J. C.; Leggere, J. C.; Morrow, B. R.; Jung, C.; Glotzer, S. C.; Taylor, D. W.; Ellington, A. D. *Nat. Chem*. **2019**, *11*, 204-212.

(13) Frey, R.; Mantri, S.; Rocca, M.; Hilvert, D. *J. Am. Chem. Soc.* **2016**, *138*, 10072-10075.

(14) Weizmann, Y.; Braunschweig, A. B.; Wilner, O. I.; Cheglakov, Z.; Willner, I. *Chem. Commun.* **2008**, *40*, 4888-4890.

(15) Sun, H.; Miao, L.; Li, J.; Fu, S.; An, G.; Si, C.; Dong, Z.; Luo, Q.; Yu, S.; Xu, J.; Liu, J. *ACS Nano*, **2015**, *9*, 5461-5469.

(16) Miao, L.; Han, J.; Zhang, H.; Zhao, L.; Si, C.; Zhang, X.; Hou, C.; Luo, Q.; Xu, J.; Liu, J. *ACS Nano*, **2014**, *8*, 3743-3751.

(17) Kitagishi, H.; Oohora, K.; Yamaguchi, H.; Sato, H.; Matsuo, T.; Harada, A.; Hayashi, T. *J. Am. Chem. Soc.* **2007**, *129*, 10326-10327.

(18) Oohora, K.; Kajihara, R.; Fujimaki, N.; Uchihashi, T.; Hayashi, T. *Chem. Commun.* **55**, 2019, 1544-1547.
(19) Oohora, K.; Burazerovic, S.; Onoda, A.; Wilson, Y. M.; Ward, T. R.; Hayashi, T. *Angew. Chem. Int. Ed.* **2012**, *51*, 3818-3821.
(20) Kitagishi, H.; Kakikura, Y.; Yamaguchi, H.; Oohora, K.; Harada, A.; Hayashi, T. *Angew. Chem. Int. Ed.* **2009**, *48*, 1271-1274.
(21) Carlson, J. C. T.; Jena, S. S.; Flenniken, M.; Chou, T.-F.; Siegel, R. A.; Wagner, C. R. *J. Am. Chem. Soc.* **2006**, *128*, 7630-7638.
(22) Ringler, P.; Schultz, G. E. *Science*, **2003**, *302*, 106-109.
(23) Dang, D. T.; Bosmans, R. P. G.; Moitzi, C.; Voets, I. K.; Brunsveld, L. *Org. Biomol. Chem.* **2014**, *12*, 9341-9344.
(24) Churchfield, L. A.; Tezcan, F. A. *Acc. Chem. Res.* **2019**, *52*, 345-355.
(25) Malay, A. D.; Miyazaki, N.; Biela, A.; Chakraborti, S.; Majsterkiewicz, K.; Stupka, I.; Kaplan, C. S.; Kowalczyk, A.; Piette, B. M. A. G.; Hochberg, G. K. A.; Wu, D.; Wrobel, T. P.; Fineberg, A.; Kushwah, M. S.; Kelemen, M.; Vavpetič, P.; Pelicon, P.; Kukura, P.; Benesch, J. L. P.; Iwasaki, K.; Heddle, J. G. *Nature*, **2019**, *569* 438-442.
(26) Fierer, J. O.; Veggiani, G.; Howarth, M. *Proc. Natl. Acad. Sci. U. S. A.* **2014**, *111*, E1176-E1181.
(27) Suzuki, Y.; Cardone, G.; Restrepo, D.; Zavattieri, P. D.; Baker, T. S.; Tezcan, F. A. *Nature*, **2016**, *533*, 369-373.
(28) Ballister, E. R.; Lai, A. H.; Zuckermann, R. N.; Cheng, Y.; Mougous, J. D. *Proc. Natl. Acad. Sci. U. S. A.* **2008**, *105*, 3733-3738.
(29) Kashiwagi, D.; Sim, S.; Niwa, T.; Taguchi, H.; Aida, T. *J. Am. Chem. Soc.* **2018**, *140*, 26-29.
(30) Subramanian, R. H.; Smith, S. J.; Alberstein, R. G.; Bailey, J. B.; Zhang, L.; Cardone, G.; Suominen, L.; Chami, M.; Stahlberg, H.; Baker, T. S.; Tezcan, F. A. *ACS Cent. Sci.* **2018**, *4*, 1578-1586.
(31) Matsuura, K.; Honjo, T. *Bioconjugate Chem.* **2019**, *30*, 1636-1641.
(32) Velonia, K.; Rowan, A. E.; Nolte, R. J. M. *J. Am. Chem. Soc.* **2002**, *124*, 4224-4225.
(33) Reynhout, I. C.; Cornelissen, J. J. L. M.; Nolte, R. J. M. *J. Am. Chem. Soc.* **2007**, *129*, 2327-2332.
(34) Fujishige, S.; Kubota, K.; Ando, I. *J. Phys. Chem.* **1989**, *93*, 3311-3313.
(35) Lam, C. N.; Kim, M.; Thomas, C. S.; Chang, D.; Sanoja, G. E.; Okwara, C. U.; Olsen, B. D. *Biomacromolecules*, **2014**, *15*, 1248-1258.
(36) Wan, X.; Liu, S. *Macromol. Rapid Commun*. **2010**, *31*, 2070-2076.
(37) Li, M.; De, P.; Li, H.; Sumerlin, B. S. *Polym. Chem*. **2010**, *1*, 854-859.
(38) Onoda, A.; Kakikura, Y.; Uematsu, T.; Kuwabata, S.; Hayashi, T. *Angew. Chem., Int. Ed.* **2012** *51*, 2628-2631.
(39) Oohora, K.; Fujimaki, N.; Kajihara, R.; Watanabe, H.; Uchihashi, T.; Hayashi, T. *J. Am. Chem. Soc.* **2018**, *140*, 10145-10148.
(40) Kajihara, R.; Oohora, K.; Hayashi, T. *J. Inorg. Biochem.* **2019**, *193*, 42-51.

(41) Jeoung, J.-H.; Pippig, D. A.; Martins, B. M.; Wagener, N.; Dobbek, H. *J. Mol. Biol.* **2007**, *368*, 1122-1131.

(42) Strümpfer, J.; Şener, M.; Schulten, K. *J. Phys. Chem. Lett.* **2012**, *3*, 536-542.

(43) Oohora, K.; Hirayama, S.; Mashima, T.; Hayashi, T. *J. Porphyrins Phthalocyanines, in press*.

(44) Sato, T.; Tanaka, K.; Toyokura, A.; Mori, R.; Takahashi, R.; Terao, K.; Yusa, S. *Macromolecules,* **2013**, *46*, 226-235.

(45) van Eldijk, M. B.; Wang, J. C.-Y.; Minten, I. J.; Li, C.; Zlotnick, A.; Nolte, R. J. M.; Cornelissen, J. J. L. M.; van Hest, J. C. M. *J. Am. Chem. Soc.* **2012**, *134*, 18506-18509.

(46) Huard, D. J. E.; Kane, K. M.; Tezcan, F. A. *Nat. Chem. Biol.* **2013**, *9*, 169-176.

(47) Brault, P.-A.; Kariapper, M. S. T.; Pham, C. V.; Flowers, R. A.; Gunning, W. T.; Shah, P.; Funk, M. O. *Biomacromolecules*, **2002**, *3*, 649-654.

(48) Zhang, Y.; Furyk, S.; Bergbreiter, D. E.; Cremer, P. S. *J. Am. Chem. Soc.* **2005**, *127*, 14505-14510.

(49) Teale, F. W. J. *Biochim. Biophys. Acta*, **1959**, *35*, 543.

(50) Oohora, K.; Mashima, T.; Ohkubo, K.; Fukuzumi, S.; Hayashi, T. *Chem. Commun*. **2015**, *51*, 11138-11140.

(51) Mashima, T.; Oohora, K.; Hayashi, T. *Phys. Chem. Chem. Phys*. **2018**, *20*, 3200-3209.

(52) Son, H.-J.; Jin, S.; Patwardhan, S.; Wezenberg, S. J.; Jeong, N. C.; So, M.; Wilmer, C. E.; Sarjeant, A. A.; Schatz, G. C.; Snurr, R. Q.; Farha, O. K.; Wiederrecht, G. P.; Hupp, J. T. *J. Am. Chem. Soc.* **2013**, *135*, 862-869.

(53) Another possible mechanism which could rationalize the results of Stern-Volmer plots for the $ZnPP^{(6/6)}$micelle and the $ZnPP^{(1/6)}$micelle could arise from changes of the structure of the reconstituted protein and/or fluorescence properties of photosensitizers in relation to the different numbers of photosensitizer molecules bound to the hexamer. However, this contribution is most likely negligible because UV–vis and fluorescence spectra of PNIPAAm-$ZnPP^{(6/6)}HTHP^{V44C}$ in the absence of MV^{2+} are consistent with those of PNIPAAm-$ZnPP^{(1/6)}HTHP^{V44C}$.

(54) Yang, J.; Yoon, M.-C.; Yoo, H.; Kim, P.; Kim, D. *Chem. Soc. Rev.* **2012**, *41*, 4808-4826.

(55) Luo, L.; Chang, C.-H.; Chen, Y.-C.; Wu, T.-K.; Diau, E. W.-G. *J. Phys. Chem. B* **2007**, *111*, 7656-7664.

(56) The time-dependent fluorescence anisotropy was determined from the equation $r(t)= (I_{VV}(t) - GI_{VH}(t))/(I_{VV} + 2GI_{VH}(t))$, where $r(t)$ is the time-dependent fluorescence anisotropy, $I(t)$ is the time-dependent fluorescence intensity, the first and second subscripts of I values indicate the polarization direction of excitation and emission light, respectively: vertical (V) or horizontal (H). The G factor is the ratio of the sensitivities of the detection system against polarized light, defined as I_{HV}/I_{HH}.

(57) Deprez, E.; Tauc, P.; Leh, H.; Mouscadet, J.-F.; Auclair, C.; Brochon, J.-C. *Biochemistry,* **2000**, *39*, 9275-9284.

(58) Hwang, I.-W.; Kamada, T.; Ahn, T. K.; Ko, D. M.; Nakamura, T.; Tsuda, A.; Osuka, A.; Kim, D. *J. Am. Chem. Soc*. **2004**, *126*, 16187-16198.

(59) Hayashi, T.; Ando, T.; Matsuda, T.; Yonemura, H.; Yamada, S.; Hisaeda, Y. *J. Inorg. Biochem.* **2000**, *82*, 133-139.
(60) Ando, T.; Kodera, N.; Takai, E.; Maruyama, D.; Saito, K.; Toda, A. *Proc. Natl Acad. Sci. U. S. A.* **2001**, *98*, 12468-12472.
(61) Ando, T.; Uchihashi, T.; Fukuma, T. *Prog. Surf. Sci.* **2008**, *83*, 337-437.
(62) Wendel, M.; Lorenz, H.; Kotthaus, J. P. *Appl. Phys. Lett*. **1995**, *67*, 3732-3734.

Conclusions

The author focused on C_6-symmetric hemoprotein, HTHP as a building block in order to construct artificial protein assemblies, whereas previous reports of artificial hemoprotein assemblies have employed monomeric hemoproteins such as myoglobin and cytochrome b_{562}. The utilization of the highly symmetric structure of HTHP and chemical modification at the protein surface with various molecules achieved the formation of novel protein assemblies and application.

In chapter 1, the author has constructed the supramolecular dimer of hexameric hemoprotein HTHP via the multiple interactions between pyrene derivatives modified onto the protein surface. The genetic mutation introduced six cysteine residues as site-specific modification points with the maleimide tethered pyrene to obtain cysteine-introduced HTHP mutant ($HTHP^{V44C}$) and the following Michael reaction resulted in the pyrene-attached $HTHP^{V44C}$ (pyr-$HTHP^{V44C}$) and the supramolecular dimer of pyr-$HTHP^{V44C}$, (pyr-$HTHP^{V44C}$)$_2$, spontaneously forms via the multiple pyrene–pyrene interactions. Additionally, it was revealed that (pyr-$HTHP^{V44C}$)$_2$ dissociates into the original hexameric structure by the extraction of the heme molecule. This dissociation appears to occur because of the incorporation of each attached pyrene into the adjacent heme pocket.

In chapter 2, the author has demonstrated that the formation of two-dimensional protein assembly is triggered by the combination of C_6-symmetric protein and C_2-symmetric supramolecular complex. The surface modification of Q14C mutant of HTHP ($HTHP^{Q14C}$) with FGG tripeptide (FGG-tag) and the addition of the cucurbit[8]uril, a host molecule selectively binding two FGG-tags, provides the two-dimensional protein assembly of HTHP. The formation process and detailed structure of two-dimensional assembly was directly observed by high-speed atomic force microscopy (HS-AFM)

In chapter 3, the author has demonstrated the formation of thermoresponsive micellar assembly of HTHP and its application for an artificial light-harvesting system. The surface modification of V44C mutant HTHP ($HTHP^{V44C}$) with thermoresponsive poly(*N*-isopropylacrylamide), PNIPAAm, to obtain the PNIPAAm-attached $HTHP^{V44C}$ (PNIPAAm-$HTHP^{V44C}$) to construct the protein assembly upon heating. The formation of this micellar assembly is repetitive and the protein maintains the folding structure in this procedure. HS-AFM measurements of the micellar assembly cross-linked by glutaraldehyde proved that HTHP units are covering the inner core of a PNIPAAm cluster. Moreover, the exchange of heme of HTHP with a photosensitizer, Zn protoporphyrin IX (ZnPP), in micellar assembly resulted in the construction of a ZnPP array as an artificial light-harvesting system. The fluorescence quenching measurements and fluorescence anisotropy decay indicate that the energy migration among ZnPP molecules occurs on the surface of micellar assembly.

In conclusion, this study has proved that the surface modification of proteins with various molecules can afford to construct the artificial protein assemblies with different morphologies depending on the structure and characteristics of attached molecules. The author suggests that the chemical modification of symmetric protein can work as the effective method to construct protein assemblies. Additionally, it was proved that the constructed high-ordered protein assembly can be

applied to artificial light-harvesting system. These findings displayed in this thesis will bestow the deep insights into the construction of artificial protein assemblies with high-ordered structure and unique functions toward novel and functional bionanomaterials near future.

List of Publications for this thesis

1. Supramolecular dimerization of a hexameric hemoprotein via multiple pyrene–pyrene interactions
   Koji Oohora, Shota Hirayama, Tsuyoshi Mashima and Takashi Hayashi
   J. Porphyrins Phthalocyanines, in press.
2. Construction of a Hexameric Hemoprotein Sheet and Direct Observation of Dynamic Process of Its Formation
   Koji Oohora, Shota Hirayama, Takayuki Uchihashi, Takashi Hayashi
   Chem. Lett. **2020**, *49*, 186–190.
3. Thermoresponsive Micellar Assembly Constructed from a Hexameric Hemoprotein Modified with Poly(*N*-isopropylacrylamide) toward an Artificial Light-harvesting System
   Shota Hirayama, Koji Oohora, Takayuki Uchihashi, Takashi Hayashi
   J. Am. Chem. Soc. **2020**, *142*, 1822–1831.

Acknowledgement

The study presented in this thesis has been carried out at Department of Applied Chemistry, Graduate School of Engineering, Osaka University from April 2014 to March 2020. The author would like to express his best gratitude to Professor Takashi Hayashi for his continuous guidance, insightful suggestion, constant discussions and warm encouragement throughout this research. The author would like to deeply thank Dr. Koji Oohora for his kind and continuous guidance, valuable suggestions, and helpful discussions. The author also acknowledges Professors Hidehiro Sakurai and Masaya Nogi for reviewing this thesis and their valuable suggestions.

Acknowledgements are also made to Professor Takayuki Uchihashi at Department of Physics and Structural Biology Research Center, Graduate School of Science, Nagoya University for his assistance on AFM simulations in Chapter 2 and high-speed AFM measurements in Chapter 2 and 3.

The author would like to express his gratitude to Dr. Akira Onoda for his helpful suggestion and insightful discussion. Acknowledgement is also made to Ms. Kiyomi Lee for her kind help in laboratory life, and all members at Professor Takashi Hayashi's group and Professor Luc Brunsveld's group for their discussions, encouragements and friendship.

The author is grateful for financial support by the program of leading graduate schools at Osaka University; Interdisciplinary Program for Biomedical Sciences (5 years).

Finally, the author expresses his great gratitude to his family, Shinya, Hiroko, Suzuka, Mifuyu for their heartfelt assistance and encouragements.

Shota Hirayama
January 2020